Broad-spectrum immune suppression encoded in self-amplifying RNA enables non-cytotoxic, non-immunostimulatory, reversible transgene expression

Tony K.Y Lim,[1,*] Anne Ritoux,[1] Luke W. Paine,[1] Larissa Ferguson,[2] Tawab Abdul,[1] and Ewan St. John Smith[1,**]
[1]Department of Pharmacology, University of Cambridge, Cambridge, UK
[2]MRC Laboratory of Molecular Biology, Cambridge, UK
*Correspondence: tony.ky.lim@gmail.com
**Correspondence: es336@cam.ac.uk

ABSTRACT

Self-amplifying RNA (saRNA) has the potential to provide durable, non-integrative transgene expression for transient gene therapy. However, its auto-replicative nature mimics viral infection, triggering innate immune responses that shutdown cap-dependent translation, degrade cellular mRNA, induce cell death, and release cytokines. In non-immunotherapy applications, this immune activation is undesirable as it limits transgene expression, depletes transfected cells, and damages surrounding tissues, undermining therapeutic outcomes. Moreover, the use of exogenous immune suppressants to mitigate these effects often increases treatment complexity and the risk of unintended systemic side effects. To address these challenges, we developed a strategy to encode broad-spectrum innate immune suppression directly within saRNA. This approach leverages cap-independent translation to bypass saRNA-triggered translation shutdown, enabling the expression of multiple inhibitors targeting diverse double-stranded RNA-sensing and inflammatory signaling pathways. In mouse primary fibroblast-like synoviocytes—a model relevant to inflammatory joint diseases—this strategy eliminates the need for external immune inhibitors, reduces cytotoxicity and antiviral cytokine secretion, and enables sustained transgene expression that is reversible with a small-molecule antiviral. These findings support the development of saRNA therapeutics that offer durable, non-integrative, controllable transgene expression without persistent immune activation or reliance on exogenous immune suppressants.

GRAPHICAL ABSTRACT

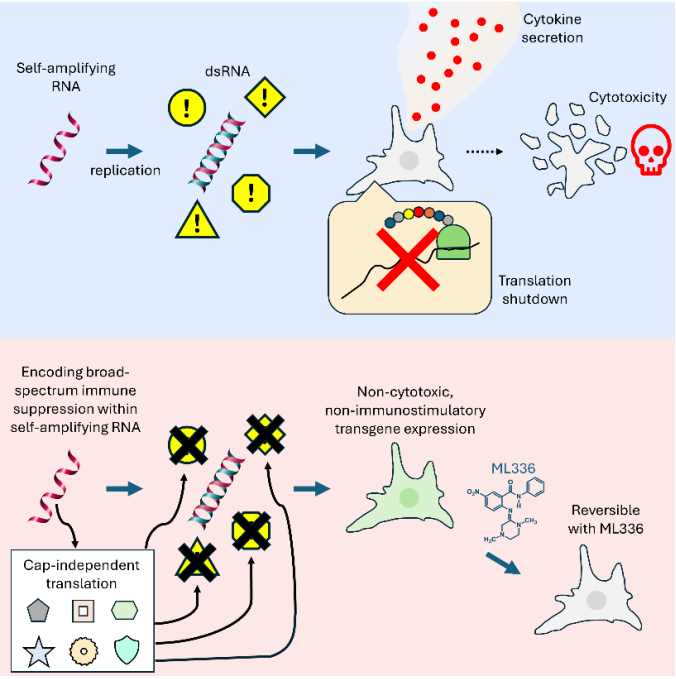

ETOC SYNOPSIS

Targeting diverse double-stranded RNA sensing and inflammatory pathways with cap-independently expressed proteins cis-encoded within self-amplifying RNA enables non-cytotoxic, non-immunostimulatory, and reversible transgene expression in mouse primary fibroblast-like synoviocytes.

INTRODUCTION

Self-amplifying RNA (saRNA) is a promising platform for transient gene therapy due to its ability to encode large therapeutic payloads and achieve sustained, non-integrative protein expression.[1] Upon cellular internalization, saRNA utilizes host machinery to synthesize an RNA-dependent RNA polymerase (RdRp), which drives replication of the saRNA genome.[2] This process involves the production of a negative-strand RNA intermediate that serves as a template for both genomic and subgenomic RNA synthesis.[3] Subgenomic RNA, encoding the gene of interest, is transcribed in excess of the genomic RNA, leading to robust and sustained protein expression.[4]

However, the self-replication of saRNA also generates double-stranded RNA (dsRNA) intermediates, formed both during the synthesis of negative-strand RNA and during the transcription of positive-strand RNA from the negative-strand template.[3] These dsRNA intermediates are potent activators of cytosolic pattern recognition receptors, triggering innate immune responses.[5,6] This recognition results in suppression of cap-dependent translation,[7–10] degradation of cellular mRNA,[6,11] induction of programmed cell death,[6,10,12–16] and release of cytokines and chemokines characteristic of viral infection[9,17,18]. While this innate immune stimulation can enhance the efficacy of immunotherapy applications such as vaccines and cancer therapy,[19] excessive stimulation can undermine potency by reducing antigen expression,[17] necessitating strategies to reduce the immunostimulatory effects of saRNA.[20] In non-immunotherapy applications, sustained activation of innate immune pathways is particularly problematic, as it limits transgene expression, depletes transfected cells, and induces inflammation. While exogenous immunosuppressants can mitigate these effects and restore transgene expression,[9,21–23] they add complexity to treatment regimens and increase the risk of unintended side effects.

Strategies to mitigate saRNA-mediated innate immune responses have included the incorporation of modified nucleotides[24], removal of dsRNA contaminants,[9,25] and co-delivery of non-replicating mRNA encoding viral innate immune inhibiting proteins.[22,26,27] While these approaches can reduce initial innate immune responses to saRNA transfection, they fall short in addressing the continuous immune activation triggered by dsRNA intermediates that arise during saRNA replication.[2] Sequence evolution of the RdRp replicon shows some promise in reducing these responses, but even engineered replicons still induce significant innate immune activation.[6,28] Another strategy involves encoding a viral immune inhibitor within the saRNA construct using a 2A self-cleaving peptide, which improves protein expression in vitro but does not significantly reduce cytokine responses, despite reductions in NF-κB and IRF3 activation.[19]

Building on these insights, we developed a fully saRNA-based approach to mitigate ongoing saRNA-induced innate immune responses. Our strategy incorporates several key innovations. First, innate immune inhibitory proteins are expressed via cap-independent translation, bypassing the cap-dependent translation shutdown commonly triggered by saRNA. Cap-dependent translation requires the presence of a 5′ cap structure on mRNA, which recruits translation initiation factors and ribosomes.[29] By contrast, cap-independent translation uses alternative mechanisms—such as internal ribosome entry sites (IRES)—to recruit ribosomes directly to the mRNA, enabling translation even when cap-dependent pathways are inhibited.[30] Second, by simultaneously targeting multiple dsRNA-sensing and inflammatory signaling pathways, our method provides a more comprehensive suppression of innate immune responses than single target approaches. Third, encoding innate immune inhibitors directly within the saRNA ensures continuous protection against persistent innate immune activation caused by dsRNA intermediates during saRNA replication, eliminating the need for exogenous immunosuppressants.

We evaluated this approach in mouse primary fibroblast-like synoviocytes (FLS), a key cell type in the pathology of inflammatory joint diseases.[31,32] To facilitate this evaluation, we developed a novel microplate assay for straightforward, longitudinal monitoring of saRNA translation control and cytotoxicity in live cells. Our results demonstrate that this strategy effectively reduces saRNA-induced cytotoxicity and cytokine production while enabling sustained cap-dependent transgene expression, which can be

reversed with a small-molecule antiviral. These results pave the way for saRNA-based therapies that offer durable, controllable transgene expression with minimal innate immune activation, achieving this without reliance on exogenous immunosuppressants.

RESULTS

Development of a microplate assay for longitudinal monitoring of translational control and cell number

Since saRNA can induce cap-dependent translation shutdown and cell death, we developed a microplate assay to simultaneously monitor cap-independent translation, cap-dependent translation, and cell number over time. In this assay, primary mouse FLS (Fig. S1) were plated in 6-well plates and transfected with saRNA constructs that used the Venezuelan equine encephalitis virus (VEEV) RdRp to self-replicate. These constructs featured a dual-fluorescence design, with EGFP expressed through encephalomyocarditis virus (EMCV) IRES-mediated, cap-independent translation, and mScarlet3 expressed through subgenomic cap-dependent translation. This dual-reporter system enabled assessment of the effects of saRNA on translational control (Fig. 1a). Spectral overlap between EGFP and mScarlet3 was corrected using linear unmixing (Figs. S2a-c).

To monitor cell number, FLS were stained with BioTracker NIR680, a lipophilic carbocyanine membrane dye that enables long-term fluorescent labeling of cells.[33] Carbocyanine dyes like BioTracker are weakly fluorescent in aqueous solution but exhibit high fluorescence when integrated into lipid bilayers. Consequently, mock transfection with Lipofectamine MessengerMAX—a lipid transfection agent—enhanced BioTracker fluorescence compared to non-transfected cells, likely due to an interaction with the lipid components of Lipofectamine (Figs. S3a, S3b). Despite this interaction, BioTracker remains effective for indicating cell number, as treatment of mock transfected cells with the apoptosis inducer staurosporine[34] reduced BioTracker fluorescence (Figs. S3a, S3b). The BioTracker results were consistent with those obtained using the viability dye calcein AM (Figs. S3c, S3d), with the added advantages of eliminating the need for additional staining and wash steps and avoiding spectral overlap with red and green fluorescent proteins. This assay allows for seamless longitudinal monitoring of cap-independent translation, cap-dependent translation, and cell number using microplate readers or imagers.

Design of saRNA constructs for inhibiting multiple dsRNA sensing pathways

Cells detect cytosolic dsRNA through several sensing pathways, including RIG-I,[35] melanoma differentiation-associated protein 5 (MDA-5),[36] protein kinase R (PKR),[37] and the oligoadenylate synthase (OAS)/RNase L pathway.[38] To broadly inhibit these pathways, we designed an saRNA construct, referred to as ‘E3’, that utilizes EMCV IRES cap-independent translation to express the vaccinia virus E3 protein (Fig. 1a). E3 protein is a pleiotropic inhibitor that binds and sequesters dsRNA, effectively blocking multiple dsRNA sensing pathways.[39]

Given the key roles of PKR in cap-dependent translation shutdown and OAS/RNase L in cellular mRNA degradation in response to dsRNA, we sought to further inhibit these pathways in a second construct. This construct includes Toscana virus NSs, a ubiquitin ligase that promotes PKR degradation,[40] and Theiler’s virus L*, which inhibits RNase L.[41] To enable co-expression of these three proteins—E3, NSs, and L*—we incorporated 2A “self-cleaving” peptide sequences between the proteins, allowing the polyprotein to be cleaved into separate proteins during translation. As prior experiments showed that using multiple identical 2A peptides can reduce protein expression,[42] we selected non-identical 2A peptides for this construct. This construct, named ‘E3-NSs-L*’, is expected to provide a more comprehensive inhibition of dsRNA-sensing pathways than the E3 construct.

Finally, as a control, we designed a ‘native saRNA’ construct that expresses a blue fluorescent protein (moxBFP) as a visual marker of IRES functionality in place of inhibitors of dsRNA-sensing pathways. Importantly, moxBFP expression did not overlap spectrally with the EGFP or mScarlet3 channels (Figs. S2a-c).

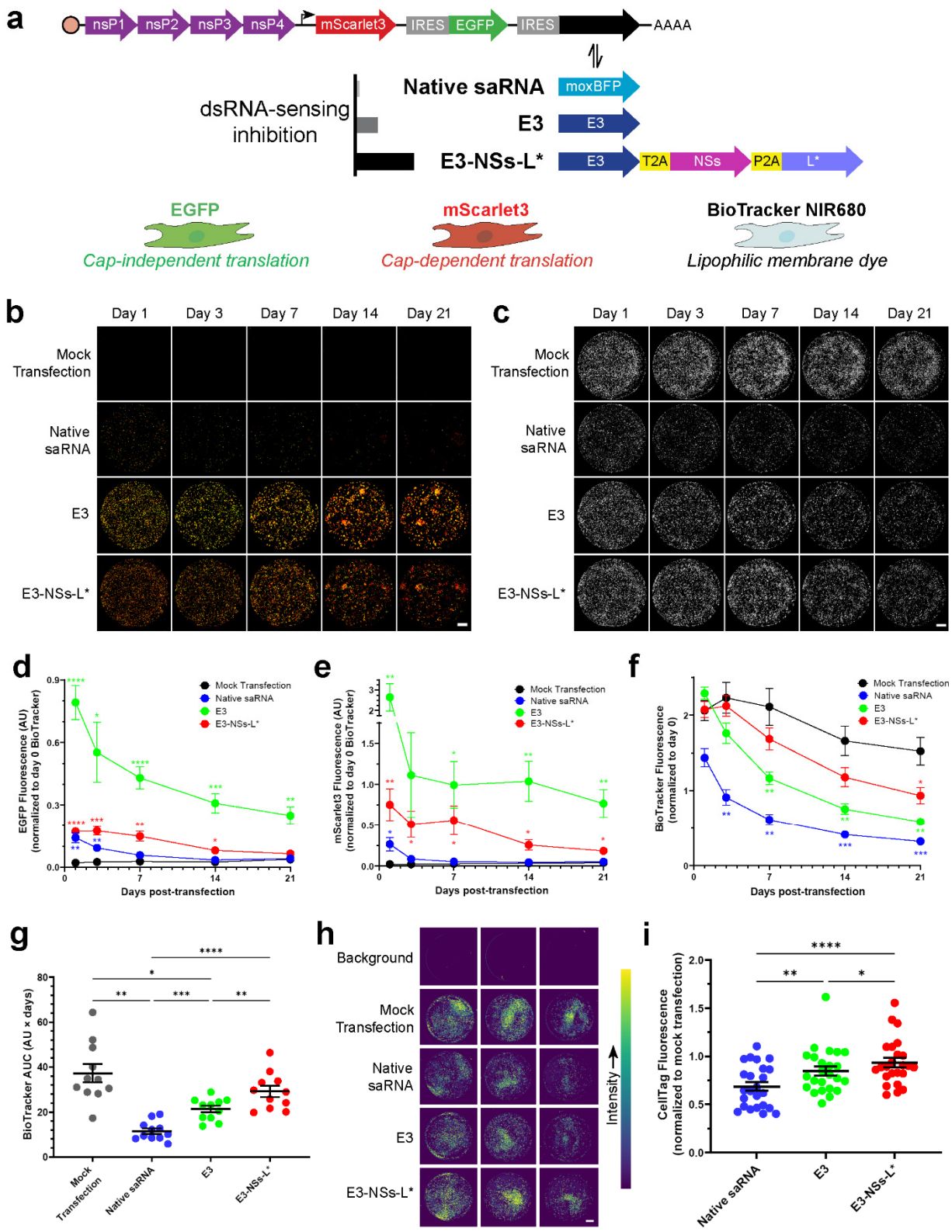

Fig. 1. Differential effects of moderate and strong dsRNA-sensing pathway inhibition on saRNA transgene expression and cell loss

a, Schematic of the native saRNA, E3, and E3-NSs-L* constructs designed to inhibit dsRNA-sensing pathways and report saRNA transgene expression. The native saRNA construct lacks dsRNA-sensing inhibitors. The E3 construct expresses vaccinia virus E3, a pleiotropic inhibitor of dsRNA sensing, expected to provide moderate inhibition. The E3-NSs-L* construct expresses vaccinia virus E3, and additionally includes Toscana virus NSs and Theiler's virus L*, which target the PKR and OAS/RNase L pathways, expected to provide strong inhibition. EGFP is expressed via an IRES to report cap-independent translation, while a subgenomic promoter (depicted with an angled arrow) enables transcription of an RNA transcript that expresses mScarlet3 via cap-dependent translation. saRNA constructs were transfected into primary mouse FLS, which were labeled with BioTracker to monitor cell number.
b, Representative images of EGFP (green) and mScarlet3 (red) expression in FLS transfected with native saRNA, E3, or E3-NSs-L* over 3 weeks. Scale bar = 5 mm.
c, Representative images of FLS transfected with the same constructs, showing BioTracker intensity over time. Scale bar = 5 mm.
d, Quantification of EGFP fluorescence over time (n = 11). The E3 construct provided the greatest EGFP expression, while the E3-NSs-L* construct showed intermediate levels. Statistical significance of treatment effects at each time point compared to mock transfection was determined by two-way RM ANOVA with Greenhouse–Geisser correction and Dunnett's multiple comparisons test.
e, Quantification of mScarlet3 fluorescence over time (n = 11). The E3 construct provided the greatest mScarlet3 expression, while the E3-NSs-L* showed intermediate levels. Statistical significance of treatment effects at each time point compared to mock transfection was determined by two-way RM ANOVA with Greenhouse–Geisser correction and Dunnett's multiple comparisons test.
f, Quantification of BioTracker fluorescence over time (n = 11). The native saRNA and E3 constructs reduced BioTracker fluorescence, indicating cell loss. Statistical significance of treatment effects at each time point compared to mock transfection was determined by two-way RM ANOVA with Greenhouse–Geisser correction and Dunnett's multiple comparisons test.
g, AUC analysis of BioTracker fluorescence data shown in (f), summarizing cumulative effects over the time course (n = 11). Increasing dsRNA-sensing pathway inhibition prevents saRNA-induced reductions in integrated BioTracker signal. Statistical analysis was performed using one-way RM ANOVA with Greenhouse–Geisser correction and Tukey's multiple comparisons test to compare all groups. Mock transfection data is also presented in Fig. S5a.
h, Representative images of FLS stained with the cell number normalization dye, CellTag 700. Columns represent cells plated from the same biological replicate, while rows show different treatments. Scale bar = 2.5 mm.
i, Quantification of mock transfection normalized CellTag signal (n = 24). Increasing dsRNA-sensing pathway inhibition mitigates saRNA-induced reductions in CellTag signal. Statistical analysis was performed using one-way RM ANOVA with Greenhouse–Geisser correction and Holm-Šídák's multiple comparisons test to compare all groups. Assays were performed 2 days post-transfection. Data in this panel were pooled from in-cell western assays, incorporating data presented in Figs. 3 and 6 as well as additional data not shown elsewhere.
For all statistical reporting, *P < 0.05, **P < 0.01, ***P < 0.001 and ****P < 0.0001. Data are presented as mean ± SEM.
For panels (d-f): Data were normalized to starting cell number, indicated by BioTracker intensity on day 0, prior to transfection. The mock transfection control data is also presented in Figs. 5c-e.

Acronyms: saRNA, self-amplifying RNA; dsRNA, double-stranded RNA; nsP, Venezuelan equine encephalitis virus non-structural protein; IRES, encephalomyocarditis virus internal ribosome entry site; moxBFP, monomeric oxidizing environment-optimized blue fluorescent protein; E3, Vaccinia virus E3 protein; NSs, Toscana virus non-structural NSs protein; L*, Theiler's murine encephalomyelitis virus L* protein; T2A, Thosea asigna virus 2A peptide; P2A, porcine teschovirus-1 2A peptide; PKR, protein kinase R; OAS, oligoadenylate synthase; AUC, area under the curve.

Moderate dsRNA-sensing pathway inhibition enables high transgene expression at the cost of cell loss, while strong inhibition preserves cell number at lower expression levels

Following transfection of saRNA constructs, we monitored BioTracker, EGFP, and mScarlet3 fluorescence over 3 weeks (Figs. 1b, 1c). Inhibiting dsRNA-sensing pathways with viral proteins

185 significantly enhanced saRNA transgene expression (Figs. 1d, 1e). Interestingly, the E3 construct
186 produced the highest levels of EGFP and mScarlet3 expression, surpassing both native saRNA and the
187 E3-NSs-L* construct. Native saRNA yielded low levels of transgene expression, while E3-NSs-L* showed
188 intermediate expression.

189 Achieving durable transgene expression depends equally on preserving cell viability and maximizing
190 transgene expression, as constructs that induce cell death undermine the goal of sustained transgene
191 expression. Transfection of FLS with native saRNA caused both immediate and long-term reductions in
192 cell number, as indicated by BioTracker intensity (Fig. 1f). While the E3 construct initially maintained cell
193 number, BioTracker signals gradually diminished over time. In contrast, the E3-NSs-L* construct provided
194 sustained protection against the decline in cell number. To quantify the cumulative effects of different
195 saRNA constructs on cell number over the experimental time course, we performed area under the curve
196 (AUC) analysis, demonstrating that E3-NSs-L* significantly protected against a decline in cell number
197 compared to the E3 construct (Fig. 1g). These findings were further supported by experiments using
198 CellTag, a cell number normalization stain (Fig. 1h), which revealed that increasing dsRNA-sensing
199 pathway inhibition protects against cell loss (Fig. 1i). Together, these results suggest that while the E3
200 construct effectively enhances saRNA transgene expression, it is associated with greater cell loss,
201 underscoring the advantage of the E3-NSs-L* construct for applications requiring sustained, non-cytotoxic
202 gene expression.

203 *Inhibiting dsRNA sensing pathways reduces saRNA-induced cytotoxicity and improves cell*
204 *viability*

205 saRNA is known to induce programmed cell death,[6,10,12–16] which often leads to cell detachment.[43] Thus
206 reductions in BioTracker signal following saRNA treatment are likely indicative of this process. However,
207 since BioTracker is a lipophilic membrane dye, the reduction in signal may not necessarily correlate with
208 cell viability or cytotoxicity. In addition to long-term cell tracking, lipophilic membrane dyes like BioTracker
209 are often used to stain extracellular vesicles, which bud off from the plasma membrane.[44] During cellular
210 stress, increased production of extracellular vesicles[45] could deplete the membrane-associated
211 BioTracker dye from cells, resulting in a lower detectable signal. Therefore, the observed reduction in
212 BioTracker signal could reflect enhanced extracellular vesicle production rather than cell death.

213 To provide more definitive evidence that inhibiting dsRNA-sensing pathways protects against saRNA-
214 induced cytotoxicity, we conducted a longitudinal assay with annexin V staining over 6 days (Fig. 2a),
215 followed by calcein AM staining on day 7 (Fig. 2b). Annexin V, a membrane-impermeable protein, binds
216 to phosphatidylserine, which translocates to the extracellular side of the cell membrane during early
217 apoptosis, enabling the detection of apoptotic cells with intact membranes.[46] If the membrane is
218 compromised, annexin V can enter cells and stain intracellular phosphatidylserine, indicating late
219 apoptosis or necrosis.[47] Calcein AM, a viability dye, accumulates in metabolically active cells with intact
220 membranes, serving both as a marker of live cell number and an indicator of membrane integrity.[48]

221 The apoptosis inducing agent staurosporine caused a transient increase in annexin V staining that
222 decreased after the first day (Fig. 2c), along with a marked reduction in calcein AM fluorescence
223 compared to mock transfection (Fig. 2d), observations that are consistent with extracellular
224 phosphatidylserine translocation and/or increased membrane permeability. Similarly, native saRNA
225 induced a temporary increase in annexin V staining during the first two days post-transfection (Fig. 2c)
226 accompanied by reduced calcein AM staining (Fig. 2d). Co-expression of E3 prevented the initial increase
227 in annexin V staining, but elevated it from day 2 onward, and also resulted in significantly reduced calcein
228 AM intensity (Figs. 2c, 2d). In contrast, E3-NSs-L* had no significant effect on annexin V or calcein AM
229 staining compared to mock transfection, supporting the idea that broader inhibition of dsRNA-sensing
230 pathways, achieved by combining E3, NSs and L*, is more effective than E3 alone in preventing saRNA-
231 induced cell death and preserving cell viability.

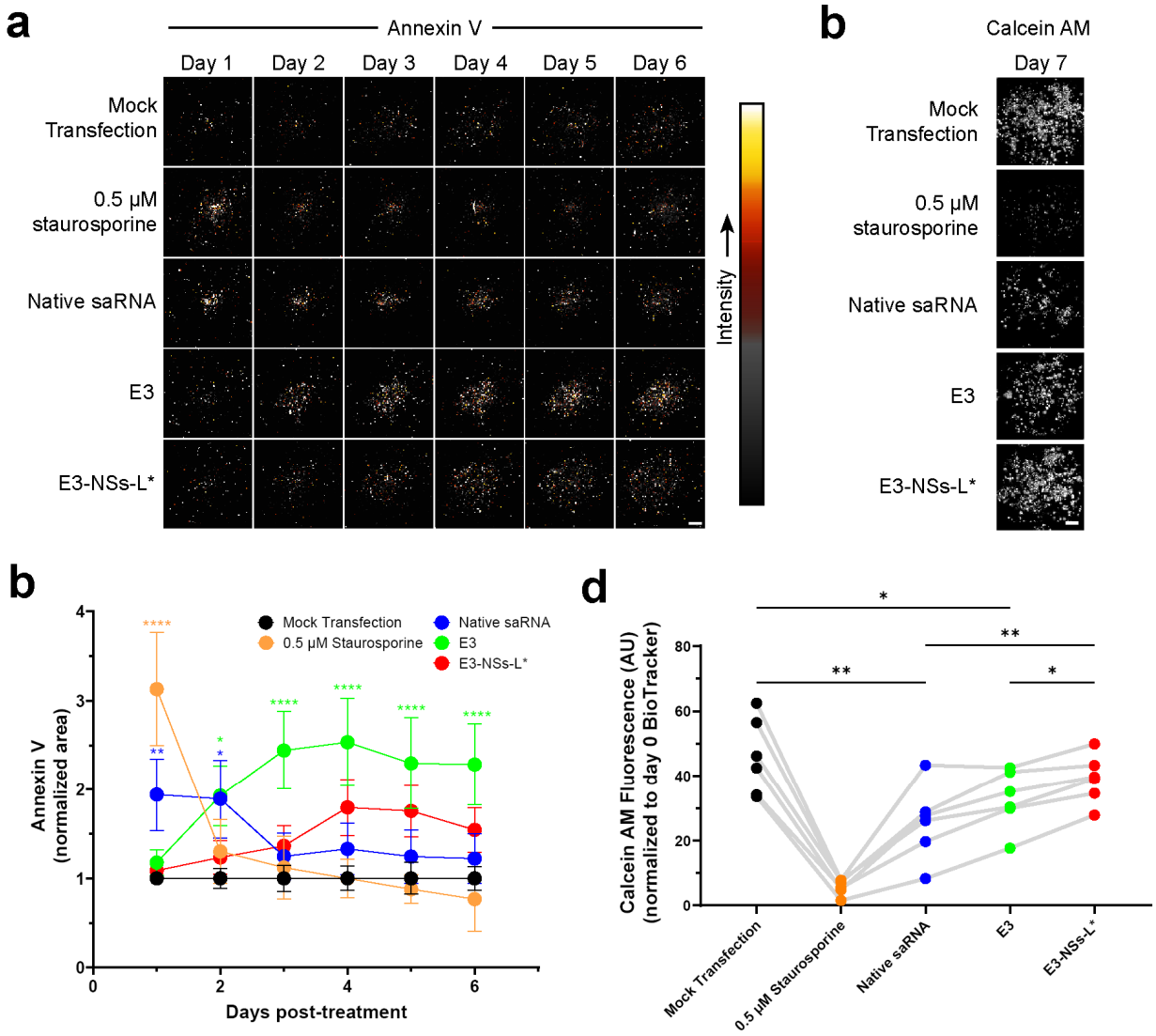

Fig. 2. saRNA induces increased phosphatidylserine staining and reduced viability, which is prevented by E3-NSs-L*

a, Representative cropped images of Annexin V-CF800 staining, indicating phosphatidylserine exposure or loss of membrane integrity, performed daily over 6 days using a microplate imager. Scale bar = 1.5 mm.
b, Representative cropped images of calcein AM staining, indicating viability, on day 7 post-treatment. Scale bar = 1.5 mm.
c, Annexin V staining, quantified as the area of positive pixels determined using Li thresholding (n = 6). Staurosporine, native saRNA, and the E3 construct significantly increased annexin V staining, while E3-NSs-L* did not. Data are normalized to the average of the mock transfection group. Statistical significance of treatment effects at each time point compared to mock transfection was determined using two-way RM ANOVA with Bonferroni's multiple comparisons test. Data are presented as mean ± SEM.
d, Calcein AM intensity measured on day 7 post-treatment (n = 6). Native saRNA, and E3 significantly reduced cell viability compared to mock transfection, while E3-NSs-L* did not. Cell viability in the E3-NSs-L* group was significantly higher than the E3 group. All groups differed significantly from staurosporine; these comparisons are omitted from the figure for clarity due to the large number of statistical comparisons. Data are normalized to cell number on day 0 as determined by BioTracker staining before transfection. Statistical significance was determined by one-way RM ANOVA with Greenhouse–Geisser

correction and Tukey's multiple comparisons test comparing all groups.
saRNA constructs used are shown in Fig. 1a. For all statistical reporting, *P < 0.05, **P < 0.01, ***P < 0.001 and ****P < 0.0001.

E3 and E3-NSs-L prevent saRNA-induced eIF2α phosphorylation and differentially regulate eIF2α levels*

We next explored how the E3 and E3-NSs-L* constructs influence translational control mechanisms during saRNA transfection. Eukaryotic initiation factor 2 alpha (eIF2α) is a central regulator of translation initiation; its phosphorylation serves as a cellular stress response to limit cellular cap-dependent protein synthesis, freeing ribosomes for cap-independent translation initiation instead.[49] Using in-cell western assays, we found that native saRNA transfection increased eIF2α phosphorylation, but both E3 and E3-NSs-L* effectively blocked this phosphorylation (Fig. 3a), consistent with previous reports of E3's inhibitory effect on eIF2α phosphorylation.[26] Interestingly, E3-NSs-L* also increased total eIF2α levels, an effect not observed with the E3 construct (Fig. 3b).

E3-NSs-L counteracts saRNA-induced PKR upregulation*

Given that PKR phosphorylates eIF2α upon activation by dsRNA,[7] we next assessed its levels following saRNA transfection. Consistent with previous reports,[6] native saRNA transfection increased PKR levels (Fig. 3c). The E3 construct similarly increased PKR levels; however, co-expression of E3-NSs-L* mitigated this increase, suggesting that E3-NSs-L* effectively counteracts saRNA-induced PKR upregulation. This is in line with the known role of the Toscana virus NSs protein as a ubiquitin ligase that targets PKR for degradation.[40]

saRNA reduces eIF4E phosphorylation without altering total eIF4E levels

We next examined the impact of saRNA transfection on eIF4E, a key regulator of translation initiation.[50] All constructs reduced eIF4E phosphorylation levels (Fig 3d), while total eIF4E levels remained unchanged (Fig. 3e).

E3-NSs-L preserves RNA integrity compared to E3*

Both the E3 and E3-NSs-L* constructs inhibited saRNA-induced eIF2α phosphorylation (Fig. 3a) and reduced eIF4E phosphorylation (Fig. 3d). However, E3-NSs-L* also reduced PKR levels (Fig. 3c) and increased total eIF2α availability for cap-dependent translation (Fig. 3b). Despite these advantages, the E3-NSs-L* construct unexpectedly produced lower levels of cap-dependent and cap-independent transgene expression compared to the E3 construct, suggesting that mechanisms beyond eIF2α and eIF4E-mediated translational control may contribute to the heightened transgene expression observed with the E3 construct.

When OAS binds dsRNA, it synthesizes 2′-5′-oligoadenylate, which activates RNase L to cleave single-stranded RNA, leading to cellular mRNA degradation[51] and inhibition of mRNA nuclear export,[52] thereby massively reducing host protein synthesis.[53] Many RNA viruses, including dengue and Zika, evade RNase L by localizing their transcripts within viral replication organelles, protecting them from degradation while allowing continued protein production.[52,54] Similarly, the VEEV-derived saRNA used in this study replicates within these organelles,[55] likely protecting its transcripts from RNase L activity. Consequently, RNase L activation by the E3 construct may selectively deplete cytoplasmic host mRNA while sparing saRNA. This depletion reduces competition for ribosomes, thereby enhancing the translation of saRNA transcripts. In contrast, the E3-NSs-L* construct encodes Theiler's virus L*, an RNase L inhibitor,[41] thereby preventing host mRNA degradation and forcing saRNA transcripts to compete directly with cellular mRNA for ribosomal access.

To test the hypothesis that RNase L activation by the E3 construct cleaves cellular mRNA, capillary gel electrophoresis was performed on RNA extracted from FLS transfected with the E3 and E3-NSs-L* constructs. RNA electropherograms were analyzed using the RNA integrity number (RIN) algorithm, an automated Bayesian learning method for measuring RNA integrity.[56] Cells transfected with E3-NSs-L* exhibited higher RIN than cells transfected with E3 (Fig. 3f), supporting the idea that RNase L-mediated reductions in cellular mRNA occur with the E3 construct but not with the E3-NSs-L* construct.

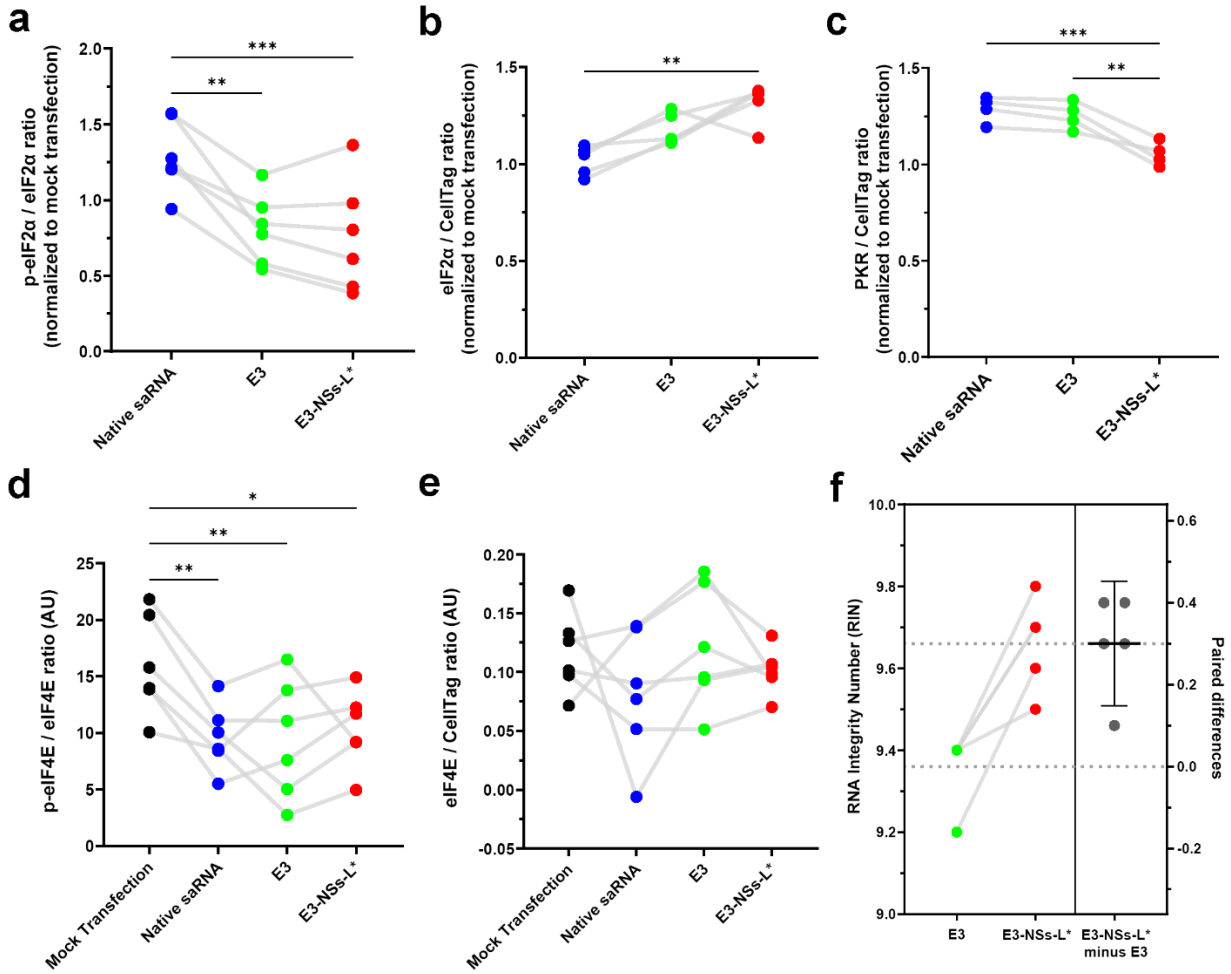

Fig. 3. Translational control alterations induced by saRNA are modulated by dsRNA-sensing pathway inhibitors with differing effects on RNA integrity

a, Phosphorylated eIF2α levels examined day 2 post-transfection by in-cell western assay (n = 6). Both E3 and E3-NSs-L* constructs significantly reduced eIF2α phosphorylation. Data are presented as fold-change relative to mock transfected cells. Statistical significance was determined by one-way RM ANOVA with Tukey's multiple comparisons test.
b, eIF2α levels examined day 2 post-transfection by in-cell western assay (n = 5). E3-NSs-L* significantly increased total eIF2α levels compared to native saRNA transfection. Data are presented as fold-change relative to mock transfected cells. Statistical significance was determined by one-way RM ANOVA with Tukey's multiple comparisons test.
c, PKR levels examined day 2 post-transfection by in-cell western assay (n = 4). E3-NSs-L* significantly reduced PKR levels compared to both native saRNA and E3 transfection. Data are presented as fold-change relative to mock transfected cells. Statistical significance was determined by one-way RM ANOVA with Tukey's multiple comparisons test.
d, Phosphorylated eIF4E levels examined day 2 post-transfection by in-cell western assay (n = 6). All saRNA constructs tested significantly reduced eIF4E phosphorylation levels compared to mock transfection. Statistical significance was determined by one-way RM ANOVA with Dunnett's multiple comparisons test comparing treatments to mock transfection.
e, eIF4E levels examined day 2 post-transfection by in-cell western assay (n = 6). One-way RM ANOVA revealed no significant differences between groups ($F(3,15) = 1.207$, $P = 0.3410$).
f, RNA integrity of FLS transfected with E3-NSs-L* is significantly higher than that of E3-transfected FLS (n = 5). RNA integrity was assessed using the RNA Integrity Number (RIN) algorithm, which ranges from

1 to 10, with 10 indicating fully intact RNA. RNA was extracted from FLS 1 day post-transfection. Data are shown as a Gardner-Altman comparison plot, with the right panel illustrating the mean effect size ± 95% CI. Statistical significance was assessed using a paired t-test (P = 0.0054).
saRNA constructs used are shown in Fig. 1a. Statistical significance is indicated as follows: *P < 0.05, **P < 0.01, ***P < 0.001. The mock transfection control data presented in panels (a), (b), (d) and (f) are also used in Fig. 6.

Design of saRNA constructs for inhibiting multiple inflammatory signaling pathways

Having addressed key saRNA-induced toxicities—including cell death, translation shutdown, and mRNA degradation—with the E3-NSs-L* construct, we next sought to design new saRNA constructs aimed at mitigating cytokine production. In these new constructs, E3-NSs-L*-EGFP was expressed via a single IRES using non-identical 2A peptides (Fig. 4a). On a second IRES, varying amounts of cellular inhibitors of inflammatory signaling were expressed. The control construct, called 'moxBFP', lacks cellular inhibitors of inflammatory signaling and instead expresses a blue fluorescent protein.

Given that activation of nuclear factor-κB (NF-κB) is a hallmark of viral infection and a master regulator of cytokine and chemokine induction,[57,58] we prioritized its inhibition using super repressor inhibitor of κBα (srIκBα). This dominant active form of IκBα cannot be phosphorylated and thus resists ubiquitination and degradation, forming a stable cytoplasmic pool of IκBα that prevents NF-κB nuclear translocation and downstream signaling.[59,60] We generated one construct expressing srIκBα alone (named 'srIκBα') and another expressing srIκBα in combination with Smad7 and suppressor of cytokine signaling 1 (SOCS1) using non-identical 2A peptides (named 'srIκBα-Smad7-SOCS1'). Smad7 negatively regulates both transforming growth factor-β (TGF-β) and NF-κB signaling pathways,[61] while SOCS1 inhibits type I, II, and III interferon (IFN) pathways as well as NF-κB signaling.[62–64]

Inhibiting dsRNA-sensing pathways and inflammatory signaling suppresses saRNA-induced cytokine secretion

Using a bead-based immunoassay on FLS culture supernatants, we observed that native saRNA transfection induced cytokine responses associated with viral infection (Figs. 4b, S4a-m). Cytokine secretion was still apparent when dsRNA-sensing pathways were inhibited, although a reduction in tumor necrosis factor (TNF)-α, IFN-α, and IFN-β levels were observed with E3 expression. Similarly, C-X-C motif chemokine ligand 10 (CXCL10) levels were reduced with E3-NSs-L* expression. On the other hand, srIκBα co-expression broadly suppressed cytokine secretion, reducing all measured cytokines to levels comparable to mock-transfected FLS. The srIκBα-Smad7-SOCS1 construct did not further reduce cytokine levels beyond the suppression achieved by srIκBα alone.

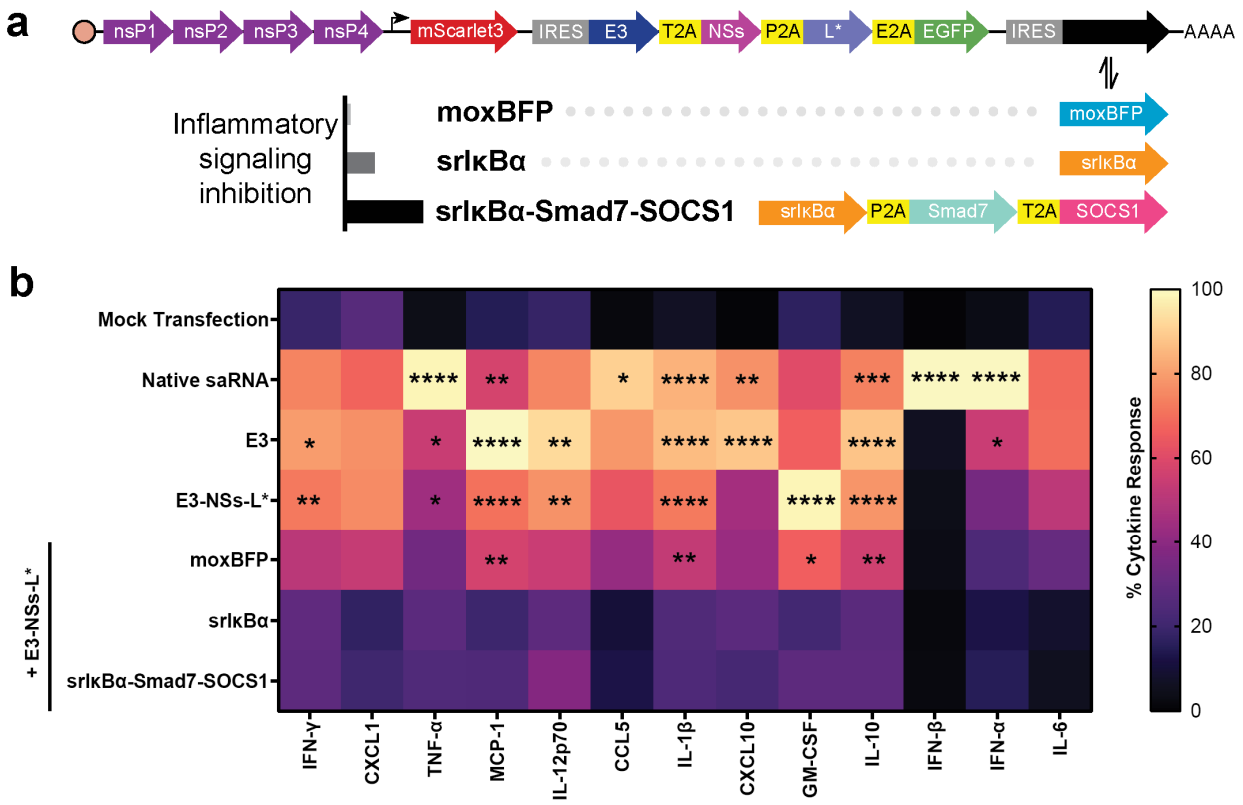

Fig. 4. Inhibiting inflammatory signaling reduces saRNA-induced anti-viral cytokine secretion

a, Schematic of the moxBFP, srIκBα, and srIκBα-Smad7-SOCS1 saRNA constructs designed for inhibition of inflammatory signaling. These constructs include dsRNA-sensing pathway inhibitors (vaccinia virus E3, Toscana virus NSs, and Theiler's virus L*). The moxBFP construct, serving as a control, lacks inflammatory signaling inhibitors. The srIκBα construct co-expresses srIκBα, which blocks the NF-κB inflammatory signaling pathway and represents moderate inflammatory signaling inhibition. The srIκBα-Smad7-SOCS1 construct co-expresses srIκBα, Smad7 and SOCS1 to additionally inhibit TGF-β and IFN pathways, representing strong inflammatory signaling inhibition. The angled arrow denotes the subgenomic promotor.
b, FLS were transfected with saRNA constructs, and anti-viral cytokines were quantified by bead-based immunoassay on day 2 post-transfection (n = 6). dsRNA-sensing pathway inhibition and inflammatory signaling inhibition significantly reduced cytokine secretion induced by saRNA. Cytokine levels were scaled within each biological replicate, with the highest value set to 100%, and the mean value displayed in the heatmap. Detailed graphs of individual cytokines are shown in Supplementary Fig. S4. For statistical analysis, cytokine levels were normalized to pre-transfection cell number (measured using BioTracker). Statistical significance for each cytokine was assessed using one-way RM ANOVA followed by Bonferroni's multiple comparisons test against the mock transfection control. A Bonferroni correction was applied to P values to account for multiple independent hypothesis testing. *$P < 0.05$, **$P < 0.01$, ***$P < 0.001$ and ****$P < 0.0001$.

Acronyms: nsP, Venezuelan equine encephalitis virus non-structural protein; IRES, encephalomyocarditis virus internal ribosome entry site; moxBFP, monomeric oxidizing environment-optimized blue fluorescent protein; E3, Vaccinia virus E3 protein; NSs, Toscana virus non-structural NSs protein; L*, Theiler's murine encephalomyelitis virus L* protein; T2A, Thosea asigna virus 2A peptide; P2A, porcine teschovirus-1 2A peptide, E2A, equine rhinitis A virus 2A peptide, srIκBα, super-repressor inhibitor of κBα; smad7, mothers against decapentaplegic homolog 7; SOCS1, suppressor of cytokine signaling 1; IFN-γ, interferon-γ; CXCL1, C-X-C motif chemokine ligand 1; TNF-α, tumor necrosis factor-α; MCP-1, monocyte chemoattractant protein-1; IL-12p70, interleukin-12; CCL5, chemokine ligand 5; IL-1β, interleukin-1β;

383 CXCL10, C-X-C motif chemokine ligand 10; GM-CSF, granulocyte-macrophage colony-stimulating factor;
384 IL-10, interleukin-10; IFN-β, interferon-β; IFN-α, interferon-α; IL-6, interleukin-6.

385 ***srIκBα* reduces cell number, whereas *srIκBα-Smad7-SOCS1* preserves cell number and enhances**
386 ***transgene expression***

387 We then examined the impact of inhibiting inflammatory signaling on cell number and transgene
388 expression (Figs. 5a, 5b). Interestingly, the srIκBα construct caused both immediate and sustained
389 reductions in cell number, as quantified by BioTracker signal, whereas the srIκBα-Smad7-SOCS1
390 construct maintained cell number comparable to mock transfection throughout the experiment (Fig. 5c).
391 AUC analysis of the BioTracker data confirmed that srIκBα-Smad7-SOCS1 significantly mitigated the
392 srIκBα-induced reduction in integrated BioTracker signal (Fig. S5a). Additional experiments using CellTag
393 and calcein AM staining corroborated these findings, showing that srIκBα negatively impacted both cell
394 number (Fig. S5b) and viability (Fig. S5c), effects that were prevented by co-expression of Smad7 and
395 SOCS1.

396 All three constructs produced low levels of EGFP expression (Fig. 5d), which was expected given EGFP's
397 position as the fourth protein in a quad-cistronic 2A element (Fig. 4a). Previous studies have
398 demonstrated that protein expression decreases significantly for downstream genes in such
399 configurations.[42] Notably, while the moxBFP and srIκBα constructs generated intermediate mScarlet3
400 levels, the srIκBα-Smad7-SOCS1 construct produced 2- to 5-fold higher mScarlet3 fluorescence
401 compared to the others (Fig. 5e).

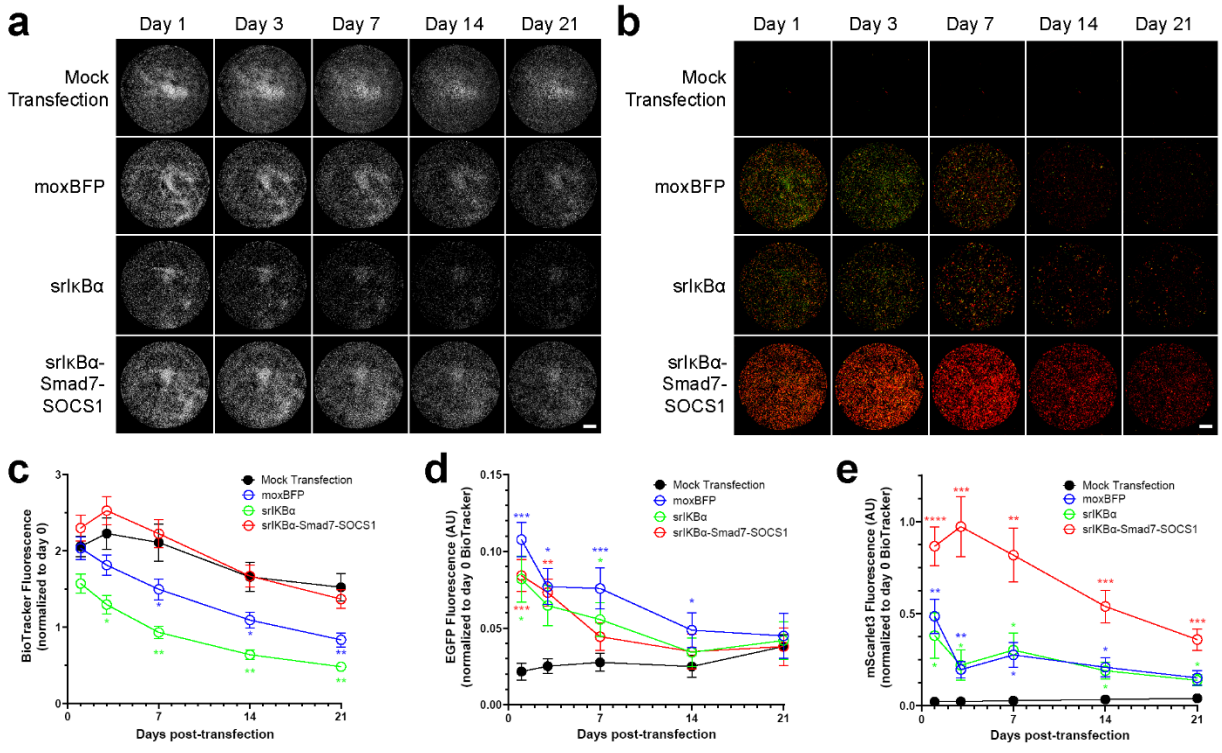

402

403 **Fig. 5. Differential effects of srIκBα and srIκBα-Smad7-SOCS1 on cell number and transgene**
404 **expression.**

405 **a**, Representative images of BioTracker staining over 3 weeks in FLS transfected with different saRNA
406 constructs. Scale bar = 5 mm.
407 **b**, Representative images of EGFP (green) and mScarlet3 (red) expression over 3 weeks in FLS
408 transfected with different saRNA constructs. Scale bar = 5 mm.
409 **c**, Quantification of BioTracker fluorescence intensity over time (n = 11). srIκBα induces reduction in cell
410 number, which is prevented by srIκBα-Smad7-SOCS1. Statistical significance of treatment effects at each

time point compared to mock transfection was determined by two-way RM ANOVA with Greenhouse–Geisser correction and Dunnett's multiple comparisons test.
d, Quantification of EGFP fluorescence intensity over time (n = 11). All constructs showed low levels of EGFP expression. Statistical significance of treatment effects at each time point compared to mock transfection was determined by two-way RM ANOVA with Greenhouse–Geisser correction and Dunnett's multiple comparisons test.
e, Quantification of mScarlet3 fluorescence intensity over time (n = 11). The srIκBα-Smad7-SOCS1 produced 2-5 times more mScarlet3 fluorescence than either moxBFP or srIκBα constructs. Statistical significance of treatment effects at each time point compared to mock transfection was determined by two-way RM ANOVA with Greenhouse–Geisser correction and Dunnett's multiple comparisons test.
saRNA constructs used are shown in Fig. 4a. For all statistical reporting, *P < 0.05, **P < 0.01, ***P < 0.001 and ****P < 0.0001. Data were normalized to cell number (BioTracker intensity) on day 0, prior to transfection. The mock transfection control data used in this figure is also presented in Fig. 1. Data are presented as mean ± SEM.

Smad7 and SOCS1 co-expression prevents srIκBα-induced alterations in translational control

We next explored how srIκBα and srIκBα-Smad7-SOCS1 modulate translational regulation. Interestingly, srIκBα expression led to reductions in eIF2α phosphorylation, a change that was prevented by co-expression of Smad7 and SOCS1 (Fig. 6a). While neither construct affected total eIF2α levels or eIF4E phosphorylation compared to the moxBFP construct (Figs. 6b, 6c), srIκBα caused a significant reduction in total eIF4E levels (Fig. 6d). Given the critical role of eIF4E in cap-dependent translation, its depletion likely contributes to the poor transgene expression observed with srIκBα (Fig. 5e). These effects, combined with srIκBα-induced declines in cell number and viability (Figs. 5c, S5a-c), highlight the dual impact of srIκBα on translational machinery and cellular health. Importantly, Smad7 and SOCS1 co-expression preserved eIF4E levels, counteracting the disruption of cap-dependent translation caused by srIκBα.

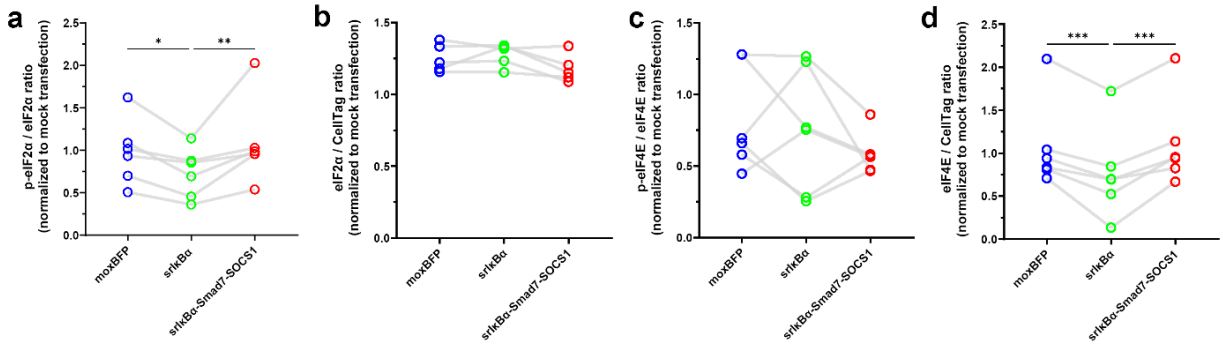

Fig. 6. *srIκBα reduces eIF2α phosphorylation and total eIF4E levels, effects reversed by co-expression of Smad7 and SOCS1*

In-cell western assays were performed 2 days post-transfection. Data are presented as fold change relative to mock-transfected cells.
a, Phosphorylation of eIF2α is significantly reduced by srIκBα, and this reduction is reversed by co-expression of Smad7 and SOCS1 (n = 6). Statistical significance was determined by one-way RM ANOVA and Holm-Šídák's multiple comparisons test to compare all groups.
b, Total eIF2α levels are not significantly affected by srIκBα or srIκBα-Smad7-SOCS1 (n = 6). One-way RM ANOVA revealed no significant differences among groups. $F(2,8)=3.683$, $P=0.0735$.
c, Phosphorylation of eIF4E is not significantly affected by srIκBα or srIκBα-Smad7-SOCS1 (n = 6). One way RM ANOVA revealed no significant difference among groups. $F(2,10)=1.336$, $P=0.3059$.
d, Total eIF4E levels are significantly reduced by srIκBα, an effect reversed by co-expression of Smad7 and SOCS1 (n = 6). Statistical significance was determined by one-way RM ANOVA and Holm-Šídák's multiple comparisons test to compare all groups.
saRNA constructs are described in Fig. 4a. For all statistical reporting, *P < 0.05, **P < 0.01 and ***P < 0.001. Mock transfection data used for normalization are the same as in Fig. 3.

453 ***Prolonged moxBFP transfection does not activate FLS, while srIκBα reduces basal activation***

454 Fibroblast activation protein-α (FAP-α) is a serine protease expressed on the surface of FLS that
455 contributes to extracellular matrix degradation and tissue remodeling.[65,66] Its expression is minimal in
456 normal adult FLS but increases significantly following inflammatory activation, such as in rheumatoid and
457 osteoarthritis.[67,68] Since viral infections can induce fibroblast activation,[69,70] we hypothesized that
458 prolonged saRNA transfection might similarly trigger FLS activation. To test this, we measured FAP-α
459 levels using an in-cell western assay after 11 days of transfection. FLS transfected with moxBFP showed
460 FAP-α levels comparable to those of mock-transfected cells, whereas srIκBα and srIκBα-Smad7-SOCS1
461 constructs resulted in significantly lower FAP-α levels compared to mock transfection (Figs. 7a, 7b).
462 These findings indicate that long-term saRNA transfection does not induce FLS activation, as measured
463 by FAP-α levels, potentially alleviating concerns that saRNA might drive pathological fibroblast
464 responses.

465

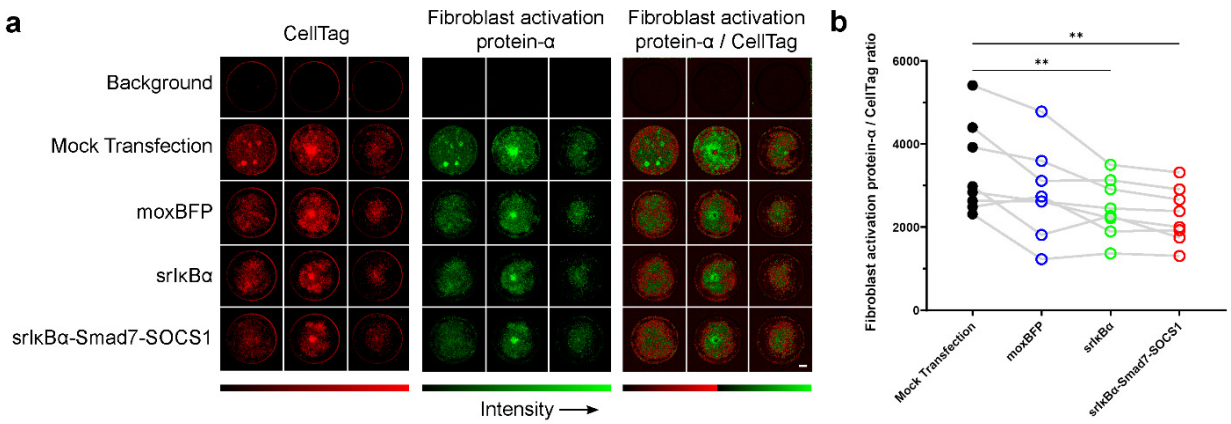

466

467 **Fig. 7. Prolonged transfection with *srIκBα or srIκBα-Smad7-SOCS1 significantly reduces basal***
468 ***fibroblast activation factor-α (FAP-α) levels***

469 **a,** Representative in-cell western images showing FAP-α expression. Columns show different biological
470 replicates, and rows show different treatments. The montage on the right shows FAP-α signal normalized
471 to CellTag signal (FAP-α/CellTag).
472 **b,** In-cell western assay of FAP-α expression (n = 8). Both srIκBα and srIκBα-Smad7-SOCS1 significantly
473 reduce FAP-α levels compared to mock transfection, while moxBFP does not differ significantly from
474 mock. Statistical significance was determined by one-way RM ANOVA with Greenhouse–Geisser
475 correction and Dunnett's multiple comparisons test to compare groups to mock transfection. **P<0.01.

476 ***Reversibility of srIκBα-Smad7-SOCS1 transfection using a small-molecule antiviral***

477 The srIκBα-Smad7-SOCS1 construct, which includes E3-NSs-L*, provides broad suppression of dsRNA
478 sensing and inflammatory signaling pathways. This construct mitigates saRNA-induced cytokine release
479 (Figs. 4b, S4a-m) and counters saRNA- and srIκBα-induced reductions in cell viability (Figs. 5c, S5a–c),
480 enabling sustained cap-dependent transgene expression (Fig. 5e) without inducing fibroblast activation
481 (Fig. 7b) or causing srIκBα-associated reductions in eIF4E levels (Fig. 6d). Together, these attributes
482 position the srIκBα-Smad7-SOCS1 construct as a promising candidate for transient gene therapy
483 applications.
484 To further enhance the therapeutic potential of this construct, we investigated whether its transfection
485 could be reversed. Achieving temporal control of transgene expression would enhance safety and
486 flexibility in therapeutic contexts. The saRNA constructs in this study rely on the VEEV RdRp for self-
487 amplification. VEEV is a mosquito-borne alphavirus capable of causing flu-like illness in humans, with the
488 potential to progress to fatal encephalitis.[71] Due to its pathogenicity, significant efforts have focused on
489 developing small-molecule inhibitors of VEEV. One such compound is ML336, a potent inhibitor of the
490 VEEV RdRp.[72]

To test whether ML336 could reverse srIκBα-Smad7-SOCS1 transfection, ML336 or vehicle was added to the culture medium one day post-transfection. EGFP and mScarlet3 fluorescence were monitored over 13 days (Fig. 8a), followed by calcein AM staining to assess cell viability (Fig. 8b). ML336 treatment significantly reduced EGFP and mScarlet3 expression over time (Figs. 8c, 8d), demonstrating its efficacy in reversing saRNA transfection. While vehicle-treated cultures exhibited lower viability compared to mock-transfected cells—possibly due to reduced proliferation over the experiment's duration—prolonged ML336 treatment did not reduce viability relative to mock-transfected controls (Fig. 8e).

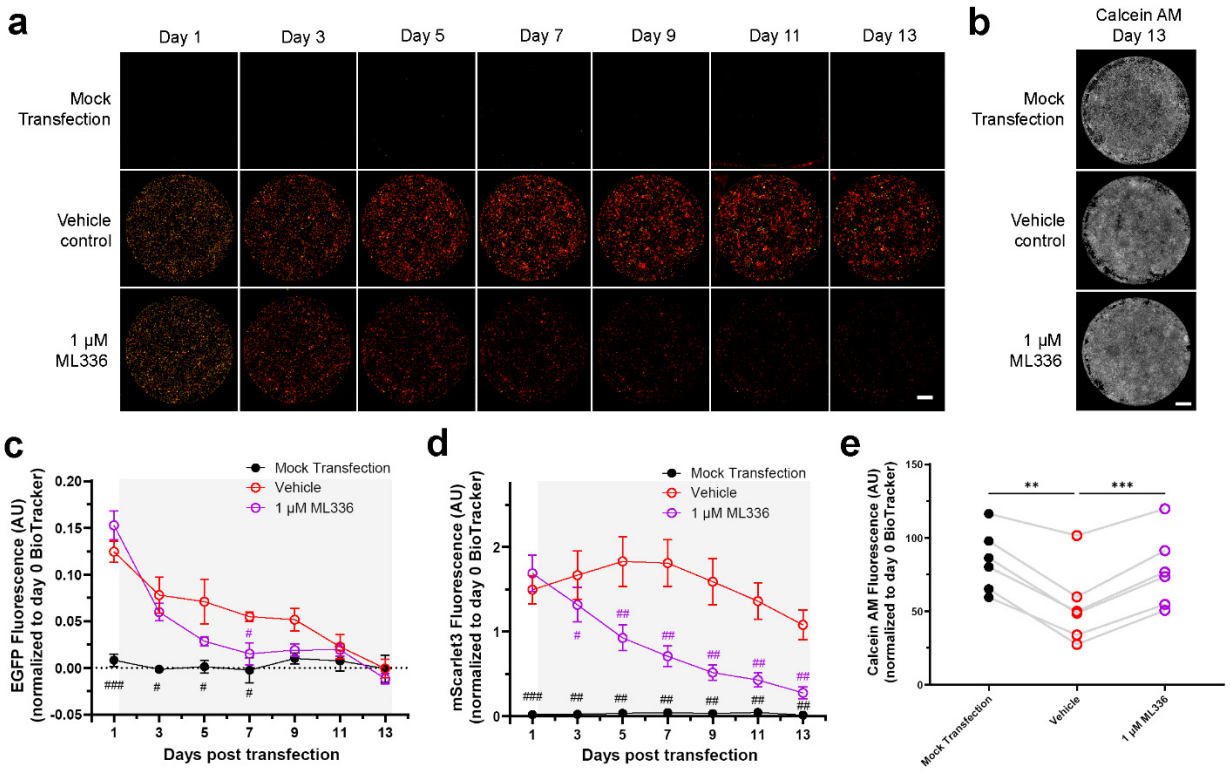

Fig. 8. ML336 reverses srIκBα-Smad7-SOCS1 saRNA transfection

a, Representative images of EGFP (green) and mScarlet3 (red) expression over 13 days in FLS transfected with srIκBα-smad7-SOCS1. Cultures were treated with vehicle or 1 μM ML336, starting 1 day post-transfection. Scale bar = 5 mm.
b, Representative images of calcein AM staining on day 13 post-transfection. Scale bar = 5 mm.
c, Quantification of EGFP fluorescence intensity in srIκBα-Smad7-SOCS1-transfected FLS (n = 6). Cultures were treated with vehicle or 1 μM ML336 (treatment period indicated by shading). EGFP fluorescence was significantly lower in ML336-treated cultures compared to vehicle-treated cultures on day 7. Statistical significance relative to vehicle-treated cells was determined by two-way RM ANOVA with Greenhouse–Geisser correction and Dunnett's multiple comparisons test. #P<0.05, ###P<0.01.
d, Quantification of mScarlet3 fluorescence intensity in srIκBα-Smad7-SOCS1-transfected FLS (n = 6). Cultures were treated with vehicle or 1 μM ML336 (treatment period indicated by shading). mScarlet3 fluorescence was significantly lower in ML336-treated cultures compared to vehicle-treated cultures beginning on day 3. Statistical significance relative to vehicle-treated cells was determined by two-way RM ANOVA with Greenhouse–Geisser correction and Dunnett's multiple comparisons test. #P<0.05, ##P<0.01, ###P<0.001.
e, Quantification of calcein AM staining on day 13 post-transfection, following 12 days of vehicle or ML336 treatment (n = 6). Cultures treated with ML336 showed no significant difference in calcein AM signal compared to mock transfection, while vehicle-treated cultures exhibited significantly lower calcein AM signals compared to both mock-transfected and ML336-treated cultures. Statistical significance was

520 determined by one-way RM ANOVA with Greenhouse–Geisser correction and Tukey's multiple
521 comparisons test. **P<0.01, ***P<0.001.
522 Data were normalized to BioTracker intensity on day 0 and are presented as mean ± SEM.

523

524 **DISCUSSION**

525 saRNA-induced translation shutdown is thought to be mediated by phosphorylation of eIF2α.[20,26,73] During
526 saRNA replication, dsRNA replicative intermediates activate PKR, leading to eIF2α phosphorylation and
527 translation inhibition.[7,26] Our study is consistent with this mechanism and additionally demonstrates that
528 saRNA induces a reduction in eIF4E phosphorylation, a phenomenon previously observed with alphavirus
529 replicons, although the underlying mechanism remains unclear.[74,75] Similar to eIF2α phosphorylation,[76] a
530 reduction in eIF4E phosphorylation decreases global cap-dependent translation initiation,[77] promoting
531 cap-independent translation.[78] These combined effects—phosphorylation of eIF2α and reduced
532 phosphorylation of eIF4E—may explain why IRES-driven, cap-independent transgenes often achieve
533 higher expression compared to those relying on cap-dependent expression when using native saRNA.[21,79]

534 To counteract saRNA-induced translation shutdown, we designed saRNA constructs that express
535 inhibitors targeting dsRNA-sensing pathways using IRES-mediated translation. During translation
536 shutdown, global mRNA translation decreases, freeing ribosomes that would otherwise be used for
537 translating capped mRNAs, thereby enhancing cap-independent translation.[80] By leveraging this
538 mechanism, IRES-mediated expression of dsRNA-sensing pathway inhibitors ensures their levels
539 increase as translation shutdown intensifies. This approach effectively inhibits dsRNA sensing and
540 alleviates translation shutdown. In contrast, encoding these inhibitors via cap-dependent translation is
541 expected to be less effective, as translation shutdown would lead to reduced inhibitor expression.

542 In this study, we used vaccinia virus E3 to prevent saRNA-induced translation shutdown, a role that E3
543 has previously been used to fulfill.[26,27] E3 achieves this by sequestering dsRNA intermediates from
544 sensors like PKR[81] and by directly inhibiting PKR activation.[82] These dual actions prevent eIF2α
545 phosphorylation, alleviating translation inhibition and enhancing transgene expression.[26,27] However, our
546 findings suggest that this mechanism is incomplete. While E3 prevents saRNA-induced eIF2α
547 phosphorylation, its ability to enhance transgene expression also depends on RNase L activity. By
548 alleviating translation inhibition, E3 facilitates unrestrained RdRp production, driving robust saRNA
549 replication and dsRNA synthesis. This dsRNA activates RNase L, which degrades mRNA[51] and inhibits
550 nuclear mRNA export.[52] The resulting depletion of cytoplasmic mRNA[53] reduces competition for
551 ribosomes, enabling enhanced translation of saRNA transcripts. These transcripts are shielded from
552 RNase L degradation due to their localization within plasma membrane-associated micro-compartments
553 called spherules.[3] Consistent with this model, inhibiting RNase L with L* in the E3-NSs-L* construct
554 reduced transgene expression, likely due to restored ribosomal competition from intact host mRNA.

555 While preventing eIF2α phosphorylation and activating RNase L drive high levels of saRNA transgene
556 expression, this combination also causes significant cytotoxicity with the E3 construct. This dual-edged
557 effect potentially makes the E3 construct suited for immunotherapy applications, such as vaccines and
558 cancer treatments, where robust transgene expression and immunogenic cell death can promote strong
559 immune responses.[83,84] In contrast, non-immunotherapy applications require strategies that prioritize cell
560 viability and minimize tissue damage over maximizing transgene expression.

561 Alphavirus vectors, including the VEEV replicon used in this study, are known to induce cytotoxicity in
562 mammalian cells.[6,10,12–16] This cytotoxicity arises from dsRNA intermediates, which activate sensors such
563 as PKR, RIG-I, MDA-5, and OAS,[5,7,26,85] despite partial shielding within spherules.[3,20] Studies in HeLa
564 cells using microinjected dsRNA show that PKR is essential for cytosolic dsRNA-induced apoptosis, while
565 RIG-I and MDA-5 are dispensable.[86] Numerous studies further underscore the central role of PKR in
566 mediating apoptosis in response to dsRNA,[87–89] and have shown that PKR can mediate dsRNA-induced
567 apoptosis even in the absence of eIF2α phosphorylation.[90] OAS also contributes to dsRNA-induced
568 apoptosis by producing 2'-5'-oligoadenylates upon binding dsRNA, which activate RNase L, leading to
569 cleavage of single-stranded RNA.[53] This disrupts cellular translation as cleavage of actively translated
570 mRNA causes ribosome stalling. Ribosomes encountering truncated 3' ends of mRNAs are unable to
571 dissociate, resulting in collisions,[91,92] triggering the ribotoxic stress response[93] which can lead to

572 apoptosis.[91,94] These findings from the literature identify PKR and OAS/RNase L as key contributors to
573 saRNA-associated cytotoxicity and highlight them as valuable targets for mitigation.

574 While E3 relieves saRNA-induced eIF2α phosphorylation,[26,27] the E3 construct also compromised RNA
575 integrity, suggesting activation of the OAS/RNase L pathway. Furthermore, PKR, an IFN-inducible gene,[95]
576 was upregulated by the E3 construct, potentially allowing partial evasion of E3-mediated inhibition. Thus,
577 vaccinia virus E3 alone did not fully address the cytotoxic actions of dsRNA replicative intermediates
578 produced during saRNA replication. To further suppress PKR and OAS/RNase L pathways, we used
579 Toscana virus NSs[40] and Theiler's virus L*,[41] respectively. While this strategy resulted in lower transgene
580 expression—likely due to the protective actions of RNase L inhibition on cellular mRNA integrity—it
581 effectively mitigated the intrinsic mechanisms of saRNA cytotoxicity. However, the inclusion of multiple
582 viral proteins introduces additional challenges. In vivo, saRNA constructs must contend not only with
583 intrinsic cytotoxic mechanisms but also with adaptive immune responses leading to extrinsic cytotoxicity.
584 The co-expression of several viral proteins, along with the VEEV RdRp, significantly increases the
585 likelihood of viral peptides being presented on major histocompatibility complex class I molecules to
586 cytotoxic T lymphocytes. This is expected to activate adaptive immune responses, which could culminate
587 in the elimination of saRNA-transfected cells. Addressing both intrinsic and immune cell-mediated
588 cytotoxicity will be critical to achieving the long-term viability of saRNA-transfected cells and unlocking the
589 platform's full therapeutic potential.

590 While we found that inhibiting dsRNA-sensing pathways was an effective means to reduce saRNA-
591 induced cytotoxicity, it was not effective at preventing saRNA-induced cytokine responses. This agrees
592 with prior reports showing that dsRNA activates NF-κB even in the absence of PKR and RNase L,[96]
593 suggesting additional mechanisms contribute to NF-κB activation. One such mechanism may involve
594 eIF4E, a key regulator of translation initiation, whose activity is governed by its phosphorylation status
595 and serves as a rate-limiting step in cap-dependent protein synthesis.[50] In this study, we found that
596 saRNA transfection induces a reduction in eIF4E phosphorylation. Reduced eIF4E phosphorylation has
597 been shown to decrease the levels of the short-lived IκBα protein,[97] an inhibitor of NF-κB that sequesters
598 it in the cytoplasm and prevents nuclear translocation. Decreased IκBα levels thus allow NF-κB to
599 translocate to the nucleus, initiating cytokine expression and inflammatory responses. To address this, we
600 expressed srIκBα using cap-independent translation to produce a stable cytoplasmic pool of IκBα, thereby
601 preventing NF-κB activity. While this strategy effectively reduced saRNA-induced cytokine responses, it
602 also resulted in a reduction in cell viability, highlighting a tradeoff between suppressing inflammation and
603 maintaining cell survival.

604 The NF-κB pathway is a key regulator of inflammatory cytokine production, making it an important target
605 for suppressing cytokine responses.[98] However, NF-κB also has pro-survival functions as it promotes the
606 transcription of anti-apoptotic genes—though its exact effects depend on tissue type and biological
607 context.[99] In FLS, overexpression of srIκBα reduces inflammatory cytokine production but increases
608 sensitivity to TNF-α-induced apoptosis,[100,101] consistent with our findings that saRNA encoding srIκBα
609 lowered both anti-viral cytokine responses and cell viability. This phenomenon is not unique to FLS;
610 inhibition of NF-κB signaling with srIκBα has also been shown to render liver hepatocytes more
611 susceptible to pro-apoptotic stimuli.[102] This raises a key safety consideration, as saRNA delivery systems
612 such as lipid nanoparticles tend to accumulate in the liver.[103] Therefore, when designing saRNA
613 constructs for sustained, non-immunostimulatory transgene expression in contexts where apoptosis is
614 undesirable, the use of srIκBα to suppress cytokine responses may require co-expression of anti-
615 apoptotic proteins to offset the loss of NF-κB-mediated survival signaling.

616 In this study, we show that co-expressing Smad7 and SOCS1 effectively counteracted srIκBα-induced
617 cell death in FLS. While we did not assess the individual contributions of each protein, both are known to
618 have anti-apoptotic properties in certain contexts. Smad7 can inhibit TGF-β-induced apoptosis,[104,105] while
619 SOCS1 can suppress apoptosis triggered by IFN-α, IFN-β,[106] IFN-γ,[107] and TNF-α.[108–110] These anti-
620 apoptotic effects likely enable Smad7 and SOCS1 to mitigate srIκBα-induced reductions in FLS cell
621 viability.

622 We also found that co-expression of Smad7 and SOCS1 significantly enhanced cap-dependent
623 transgene expression. Although we did not distinguish the contributions of each protein to this effect, it is
624 likely mediated by SOCS1. Previous studies have shown that ruxolitinib, a small-molecule inhibitor of

625 Janus kinase (JAK) 1 and JAK2,[111] increases saRNA transgene expression when added to saRNA
626 polyplexes.[18] SOCS1 is an endogenous inhibitor of JAK1 and JAK2,[112] therefore, SOCS1 offers a
627 genetically encoded alternative to the small-molecule approach of ruxolitinib for enhancing saRNA
628 expression.

629 Furthermore, this study presents a straightforward method for controlling saRNA activity. ML336, a VEEV
630 RdRp inhibitor, blocks the synthesis of positive-sense genomic, negative-sense template, and
631 subgenomic RNAs of VEEV without affecting host cellular RNA transcription.[113] It has an in vitro effective
632 concentration 50 (EC_{50}) of 0.02-0.04 μM, and a 50 mg/kg dose offers 100% protection in a lethal VEEV
633 mouse infection model, with no observed toxicity.[114] Thus, ML336 and other RdRp inhibitors could provide
634 a practical means to deactivate saRNA—either to terminate transgene expression once therapeutic
635 objectives are met or as a safety measure to reduce the risks associated with prolonged innate immune
636 suppression and other potential side effects, including adaptive immune responses to the VEEV replicon
637 or viral innate immune inhibitory proteins.

638 Preclinical and clinical data show that saRNA vaccines often trigger an intense innate immune response
639 that can hinder antigen expression.[8,18,26] Additionally, saRNA vaccines can induce significant
640 inflammation,[115,116] which is increasingly recognized as problematic, as common adverse events include
641 pain, headache, tenderness, arthralgia, fever, and chills.[117,118] The approaches described in this study,
642 which reduces the inherent immunostimulatory effects of saRNA replication, could potentially be applied
643 to future saRNA vaccine designs to improve antigen expression and reduce reactogenicity.

644 The approach in this study also underscores the versatility of the saRNA platform, which can efficiently
645 integrate multiple transgenes and genetic elements. Our largest construct included the VEEV RdRP, two
646 IRES sequences, five 2A peptides, and eight transgenes within a 16.5-kilobase saRNA. This ability to
647 encode numerous transgenes without apparent size constraints is a notable yet underutilized strength of
648 the saRNA platform.

649 Leveraging this capacity for multiple transgenes, we encoded diverse inhibitors of dsRNA-sensing and
650 inflammatory signaling pathways directly within saRNA achieving durable and reversible transgene
651 expression with minimal cytotoxicity and immunostimulation. This approach eliminates the need for
652 exogenous immune suppressants, a common requirement in other studies utilizing saRNA for non-
653 immunotherapy applications. For instance, therapeutic antibody production, cellular reprogramming, and
654 retinal cell transfection with saRNA have relied on interferon-α/β receptor-1 blocking antibodies or the
655 vaccinia virus B18R interferon decoy receptor to suppress innate immune responses and achieve
656 effective transgene expression.[9,21–23] Similarly, corticosteroids have been used to enhance antigen
657 expression by reducing saRNA-induced innate immune activation.[25] Here, we demonstrate that encoding
658 broad-spectrum innate immune suppression directly within the saRNA obviates the need for additional
659 immune-modulatory treatments, thereby reducing treatment complexity. Moreover, this strategy localizes
660 immune suppression to transfected cells, which should minimize the risks of off-target effects associated
661 with systemic immune suppression.

662 Expressing multiple transgenes may also be a useful strategy for developing novel therapeutics. The NF-
663 κB, TGF-β, and JAK/signal transducer and activator of transcription (STAT) pathways are central to the
664 progression of osteoarthritis.[119–121] The srIκBα-Smad7-SOCS1 saRNA construct provides a novel strategy
665 to simultaneously target these pathways: srIκBα inhibits NF-κB, Smad7 blocks TGF-β, and SOCS1
666 suppresses the JAK/STAT pathway. Each of these proteins has been independently studied as a
667 treatment for osteoarthritis,[122–124] and their combination within a single construct could represent a
668 synergistic strategy to enhance therapeutic efficacy. While arthritogenic alphaviruses such as
669 chikungunya virus and Ross river virus can drive inflammatory responses in FLS, including upregulation
670 of secreted proteolytic molecules such as matrix metalloproteases,[125,126] the lack of FAP-α upregulation in
671 transfected FLS provides some evidence that saRNA transfection does not trigger comparable
672 responses. Moreover, the reduction in basal FAP-α levels observed with the srIκBα and srIκBα-Smad7-
673 SOCS1 constructs raises the possibility that saRNA could serve as a tool for suppressing fibroblast
674 activation in inflammatory settings. This approach could hold therapeutic potential in arthritis treatment,[127]
675 warranting further investigation in disease models.

676 In addition to expressing therapeutic transgenes, saRNA holds potential for inducing therapeutic effects
677 by modulating translational control. While the strategy outlined in this report mitigated eIF2α

678 phosphorylation, it was not effective at preventing saRNA-induced reductions in eIF4E phosphorylation.
679 In vitro directed evolution of the RdRp replicon[6,28,128] may offer a potential solution to this challenge.
680 Furthermore, we found that srIκBα expression decreased eIF4E levels, consistent with previous
681 findings.[129] While reducing eIF4E activity through saRNA or srIκBα expression could lower transgene
682 expression, it may also have therapeutic value, as lower eIF4E activity is associated with decreased pain
683 sensitivity,[130] inhibition of tumorigenesis[131], improvement of neurodevelopmental social deficits[132], and
684 increased longevity.[133] We also observed that srIκBα expression reduced phosphorylation of eIF2α, while
685 the E3-NSs-L* construct reduced PKR levels. Given that eIF2α phosphorylation activates the integrated
686 stress response, a pathway often driven by PKR in age-related diseases like neurodegeneration,[134]
687 saRNA may represent a novel approach to modulate stress responses in these conditions.

688 Our findings introduce a novel, fully saRNA-based strategy to overcome a key limitation of saRNA:
689 continuous innate immune stimulation. By inhibiting multiple innate immune pathways through proteins
690 expressed via cap-independent translation, we achieve sustained transgene expression with low
691 cytotoxicity and minimal antiviral cytokine induction, all without the use of exogenous
692 immunosuppressants. Building on these in vitro results, the next step will be to evaluate this strategy in
693 vivo to assess its effectiveness in complex biological environments. If successful, this approach could
694 expand the therapeutic applications of saRNA to non-immunotherapy contexts, such as protein
695 replacement therapy, therapeutic antibody production, genome editing, cellular reprogramming, and
696 immune cell engineering, where prolonged innate immune stimulation is undesirable. Importantly, the
697 reversibility of this approach offers significant advantages, enabling precise control over transgene
698 expression and serving as a crucial safety mechanism for future clinical applications.

699

700 MATERIALS & METHODS

701 *Experimental Design*

702 This study aimed to develop and evaluate saRNA constructs that modulate innate immune responses,
703 specifically targeting dsRNA sensing and inflammatory signaling pathways, to reduce saRNA-induced
704 cytotoxicity, cytokine expression, and achieve sustained transgene expression. To this end, we
705 engineered saRNA constructs that co-express multiple viral innate immune inhibitors and cellular
706 inhibitors of inflammatory signaling. The constructs were designed to enable monitoring of cap-dependent
707 and cap-independent translation using distinct fluorescent proteins.

708 The experimental approach included cloning the saRNA constructs using molecular biology techniques,
709 followed by in vitro transcription and transfection into mouse primary FLS. Transfected cells were
710 analyzed using fluorescence-based microplate assays to assess cell number, cell viability,
711 phosphatidylserine exposure, and fluorescent protein expression. Further evaluations of translational
712 control, FLS activation markers, RNA integrity, and cytokine secretion were conducted using in-cell
713 western assays, capillary electrophoresis, and bead-based immunoassays. Finally, the reversibility of
714 saRNA transfection was explored using a small-molecule inhibitor targeting the VEEV RdRp.

715 *Plasmid cloning and construct design*

716 The commercially available TagGFP2 E3L Simplicon vector (SCR725, Merck) served as the saRNA
717 backbone in this study. After removing the TagGFP2-IRES-E3 sequence, various constructs were
718 generated by combining different elements using restriction digests (FastDigest, Thermo Scientific),
719 overlap extension PCR (Phusion, Thermo Scientific), and HiFi assembly (NEBuilder, New England
720 Biolabs).

721 Genetic elements were sourced as follows: mScarlet3 from pDx_mScarlet3 (a gift from Dorus Gadella
722 [Addgene plasmid #189754]),[135] IRES-EGFP from pIRES2-EGFP (Clontech), and IRES-E3 and IRES-
723 PuroR (puromycin resistance) from the original TagGFP2 E3L Simplicon vector.

724 Custom gene synthesis (GeneArt, Thermo Scientific) was used to produce IRES-moxBFP, IRES-E3-T2A-
725 NSs-P2A-L*-E2A-mEGFP, and IRES-srIκBα-P2A-Smad7-T2A-SOCS1 sequences. The IRES sequence

726 was derived from pIRES2-EGFP (Clontech). Other sequences were derived from public databases:
727 moxBFP (FPbase ID: SSTDU),[136] mEGFP (FPbase ID: QKFJN), E3 (UniProt: P21605-1), NSs (UniProt:
728 P21699), L* (UniProt: P0DJX4), Smad7 (UniProt: O35253-1), and SOCS1 (UniProt: O35716). srIκBα was
729 engineered from IκBα (UniProt: Q9Z1E3) by substituting serines 32 and 36 with alanines. All synthesized
730 sequences were codon-optimized for mouse expression (GenSmart, GenScript).

731 Plasmids were cloned in DH5α competent *Escherichia coli* (High Efficiency, New England Biolabs) and
732 purified by maxiprep (PureLink HiPure, Invitrogen). All plasmid sequences were verified using nanopore
733 whole plasmid sequencing (Plasmidsaurus).

734 ***RNA synthesis***

735 Plasmids were linearized using XbaI (FastDigest, Thermo Scientific) at 37°C for 3 hours. The linear
736 plasmids were purified by phenol-chloroform extraction followed by sodium acetate ethanol precipitation.
737 Uncapped RNA was synthesized *in vitro* using the T7 RiboMAX Large Scale RNA Production kit
738 (Promega) at 37°C for 2 hours. After purification by ammonium acetate precipitation, the RNA was
739 denatured at 65°C for 5 minutes. Cap-1 structures were then generated using the Vaccinia Capping
740 System in conjunction with mRNA cap 2'-O-methyltransferase (both from New England Biolabs) for 45
741 minutes at 37°C. Following another ammonium acetate purification, the RNA was treated with Antarctic
742 phosphatase (New England Biolabs) for 30 minutes at 37°C. After a final ammonium acetate purification
743 step, the RNA was resuspended in THE RNA Storage Solution (Invitrogen), aliquoted, and stored at -
744 80°C until use.

745 ***Animals***

746 All mice used in this study were 5- to 12-week-old wildtype C57BL/6J mice (Bicester, UK). Both male and
747 female mice were included, though sex differences in response to saRNA transfection were not analyzed.
748 Mice were housed in groups of up to five in a temperature-controlled room (21°C), with bedding, a red
749 shelter, and enrichment materials provided. They were maintained on a 12-hour light/dark cycle, with food
750 and water available ad libitum. Mice were euthanized by exposure to CO_2 gas in a rising concentration,
751 and death confirmed by dislocation of the atlanto-occipital joint by applying pressure to the side of the
752 neck using thumb and forefinger, procedures in line with the Animals (Scientific Procedures) Act 1986
753 Amendment Regulations 2012.

754 ***Mouse primary FLS culture***

755 We cultured FLS from mouse knee joints following established protocols,[137] with slight modifications. In
756 brief, knee joints were exposed by cutting through the overlying skin with dissecting scissors. The patellar
757 tendon was then grasped near the patella with Dumont tweezers, and spring scissors were used to sever
758 the patellar tendon along with surrounding tissues. Finally, the patella was excised by cutting the
759 quadriceps tendon, and excess muscle and tendons were carefully trimmed away.

760 Both patellae from each animal were collected into a microcentrifuge tube containing ice-cold sterile
761 phosphate buffered saline (PBS), then transferred to a 24-well tissue culture plate (Costar) with FLS
762 culture media. The media consisted of DMEM/F-12 (Invitrogen) supplemented with 25% fetal bovine
763 serum (Sigma), 1X GlutaMAX (Gibco), and 100 µg/ml Primocin (InvivoGen).

764 The patellae were maintained in a humidified incubator at 37°C with 5% CO2, with media changes every
765 1-2 days. FLS outgrowth was observed, and after approximately 10 days, when cells reached 70%
766 confluency, the patellae were transferred to new wells for further FLS collection. Cells attached to the
767 original wells were passaged using 0.1% trypsin-EDTA (Sigma) into a single well of a 6-well plate
768 (Costar). Cells were later expanded into T25 flasks (BioLite, Thermo Scientific or CELLSTAR, Greiner
769 Bio-One) and passaged upon reaching confluency. After the second passage, Versene solution (Gibco)
770 was used for cell dissociation.

771 FLS were used between passages 3 and 8. In most experiments, cells from the same animal were
772 divided and plated onto 6-well or 24-well plates, allowing for parallel manipulations with matched
773 conditions. Occasionally, when cell number was low, cells from different animals were pooled before
774 division. Once plated for experiments, media was changed every 2-3 days.

775 ***Immunocytochemistry and confocal microscopy***

776 Cells were plated on poly-D-lysine-coated glass-bottom 35 mm dishes (P35GC-1.5-14-C, MatTek) and
777 fixed with 4% paraformaldehyde for 10 minutes at room temperature without permeabilization. After
778 fixation, cells were washed twice with PBS, followed by blocking with 10% normal goat serum in PBS for
779 1 hour at room temperature.

780 Cells were then incubated overnight at 4°C in blocking buffer, either without primary antibody (no primary
781 control) or with cadherin-11 (extracellular) rabbit polyclonal antibody (1:200, DF3523, Affinity
782 Biosciences). After three washes with PBS, cells were incubated for 1 hour at room temperature in
783 blocking buffer with 1 µg/ml Hoechst 33342, BioTracker NIR680 (1:2000, Merck), and goat anti-rabbit
784 Alexa Fluor 488 secondary antibody (1:500, Invitrogen).

785 After four additional PBS washes, cells were imaged in PBS using a Leica Stellaris 5 confocal microscope
786 equipped with a 40X oil immersion objective. Tile-scanned images were stitched using Las X microscopy
787 software (Leica) to generate high-resolution panoramic images.

788 ***BioTracker staining***

789 BioTracker NIR680 was diluted 1:2000 in unsupplemented DMEM/F-12. T25 flasks containing FLS were
790 washed once with HBSS (with calcium and magnesium, Gibco), then incubated with the diluted dye for 30
791 minutes at 37°C. After incubation, the flasks were washed three times with FLS media, with each wash
792 lasting 10 minutes at 37°C. The FLS were then dissociated using Versene and plated onto 6- or 24-well
793 plates.

794 ***FLS transfection***

795 For transfection in 6-well plates, the medium was removed and replaced with 1 ml of Opti-MEM I (Gibco).
796 In a microcentrifuge tube, 500 ng of saRNA was diluted in 200 µl of Opti-MEM I. In a separate tube, 3 µl
797 of Lipofectamine MessengerMAX (Invitrogen) was diluted in 100 µl of Opti-MEM I. After gently mixing, the
798 complexes were incubated at room temperature for 5 minutes, then added dropwise to the cells. The cells
799 were incubated with the complexes for 2 hours at 37°C, after which the media was removed and replaced
800 with fresh FLS media. For transfection in 24-well plates, all volumes and amounts of saRNA were
801 reduced fivefold.

802 ***Microplate imaging***

803 Unless otherwise specified, black glass-bottom 6-well plates (P06-1.5H-N, Cellvis) were used for
804 microplate imaging. Prior to imaging, the FLS media was replaced with Live Cell Imaging Solution
805 (Invitrogen). Imaging was performed using the Odyssey M laser scanner (LI-COR), using LI-COR
806 acquisition software with a plate offset of +1.45 mm and 100 µm resolution.

807 EGFP, mScarlet3, and BioTracker NIR680 were imaged using the 488, 520, and 700 channels,
808 respectively. Spectral cross-excitation between EGFP and mScarlet3 in the 488 and 520 channels was
809 corrected through linear unmixing analysis, as described below. Fluorescence intensity was quantified in
810 ImageJ by measuring the integrated density within equal-area regions of interest for each well.
811 Fluorescence values (EGFP, mScarlet3, and BioTracker) were normalized by the day 0 BioTracker signal
812 measured before transfection to account for variations in starting cell number.

813 ***Linear unmixing analysis***

814 saRNA constructs encoding individual fluorescent proteins (moxBFP, EGFP, or mScarlet3) were
815 designed to assess cross-excitation among the fluorescent proteins used in this study. tSA201 cells
816 (96121229, ECACC) were seeded in black glass-bottom 6-well plates coated with poly-D-lysine (Sigma)
817 and transfected with the saRNA constructs. Cells were imaged the following day using an Odyssey M
818 laser scanner, with fluorescence captured through the 488 and 520 channels. Expression of moxBFP was
819 undetectable in both the 488 and 520 channels, and therefore it was excluded from further analysis.
820 Bleed-through of EGFP into the 520 channel and mScarlet3 into the 488 channel was quantified using
821 ImageJ, with cross-excitation determined to be 11.32% and 0.94%, respectively. The emission signals
822 were assumed to be linearly proportional to the sum of the intensities of each fluorophore, and the
823 unmixed EGFP and mScarlet3 signals were calculated using Python.

824 ***Annexin V assay***

825 FLS were stained with BioTracker NIR680 and plated on black glass-bottom 24-well plates (Sensoplate,
826 Greiner Bio-One). Cells were transfected with saRNA or treated with 0.5 μM staurosporine (Cayman
827 Chemical) as a positive control.

828 Annexin V-CF800 conjugate (Biotium) was diluted to 250 ng/ml in Live Cell Imaging Solution (Invitrogen).
829 On each day of the assay, wells were washed with Live Cell Imaging Solution and replaced with diluted
830 Annexin V-CF800 solution. Plates were incubated at 37°C for 15 minutes. Following incubation, plates
831 were washed 3 times with Live Cell Imaging Solution before imaging the 700 and 800 channels with an
832 Odyssey M imager set to +1.45 mm image offset and 100 μm resolution.

833 Image analysis was performed using ImageJ. To correct for unidirectional spectral bleed-through of
834 BioTracker NIR680 into the 800-channel, subtractive compensation was applied by dividing the 700-
835 channel image by a factor of 800 and then subtracting it from the 800-channel image. Due to the
836 presence of a small number of high-intensity speckles in the 800-channel image, area rather than
837 fluorescence intensity was quantified. The display range of the 800-channel image was set between 0.25
838 and 2.5 and the image was thresholded using the method of Li.[138] The area of thresholded pixels within
839 each well was then quantified and adjusted based on the BioTracker signal before transfection to account
840 for variations in cell number. Data was then normalized to the average of the mock transfection condition.

841 ***Calcein AM staining***

842 Calcein AM (Invitrogen) staining was performed according to the manufacturer's protocol. Briefly, cells
843 were washed with HBSS and incubated with 2 μM calcein AM (diluted in HBSS) at 37°C for 30 minutes.
844 Following three washes, cells were imaged in Live Cell Imaging Solution, and the 488-channel image was
845 captured using an Odyssey M imager.

846 Although calcein AM and EGFP share overlapping spectra, calcein AM fluorescence was typically much
847 higher than EGFP, making EGFP's contribution to the measured Calcein AM signal negligible in most
848 cases. However, when the E3 construct was used, EGFP expression was sufficient to interfere with the
849 signal. To address this, in experiments that included use of the E3 construct, a 488-channel image was
850 captured prior to calcein AM application and subtracted from the post-application image to accurately
851 measure calcein AM fluorescence.

852 Fluorescence intensity was quantified using ImageJ. In experiments where BioTracker was used,
853 fluorescence values were corrected by the pre-transfection BioTracker signal to account for differences in
854 starting cell number.

855 ***In-cell western assay***

856 Cells were plated on black, glass-bottom 24-well plates. Alongside mock and saRNA transfections, one
857 well was reserved for background subtraction, which received no treatment. Unless specified otherwise,
858 experiments were conducted 2 days post-transfection. Cells were fixed with 4% paraformaldehyde for 10

859 minutes at room temperature, followed by two washes with tris-buffered saline (TBS). Permeabilization
860 was then performed using 0.1% Triton X-100 in TBS for 10 minutes, followed by two additional TBS
861 washes. After permeabilization, cells were blocked with Intercept TBS Blocking Buffer (LI-COR) for 1 hour
862 at room temperature with gentle agitation.

863 Primary antibodies were diluted in Intercept Blocking Buffer and incubated with the cells overnight at 4°C.
864 The background subtraction well was incubated with blocking buffer alone, without primary antibodies.
865 The following primary antibodies were used: Phospho-eIF2α (Ser51) (D9G8) XP rabbit monoclonal
866 (1:200, #3398, Cell Signaling Technology), eIF2α (L57A5) mouse monoclonal (1:200, #2103, Cell
867 Signaling Technology), PKR rabbit polyclonal (1:500, #18244-1-AP, Proteintech), Phospho-eIF4E (S209)
868 rabbit monoclonal (1:200, #ab76256, Abcam), eIF4E mouse monoclonal (5D11) (1:200, #MA1-089,
869 Invitrogen), and fibroblast activation protein (73.3) mouse monoclonal (20 µg/ml, #BE0374, InVivoMAb).
870 Except for the fibroblast activation protein antibody, which was conjugated to DyLight 800 using the
871 manufacturer's DyLight Antibody Labeling Kit (#53062, Thermo Scientific), all primary antibodies were
872 unconjugated.

873 After washing the wells three times with TBS, cells were incubated for 1 hour at room temperature with
874 the appropriate secondary antibodies or normalization stain, with gentle agitation. The secondary
875 antibodies used were goat anti-mouse IRDye 800CW (1:800), donkey anti-rabbit IRDye 800CW (1:800),
876 donkey anti-mouse IRDye 680RD (1:800), and CellTag 700 (1:500), all from LI-COR. The background
877 subtraction well received secondary antibody but no CellTag. Following four additional washes with TBS,
878 the plate was inverted and gently tapped on absorbent paper to remove excess liquid. The plate was then
879 imaged using the Odyssey M imager with LI-COR Acquisition software using a plate offset of +1.45 and
880 100 µm resolution. Signal quantification was carried out using Empiria Studio software (LI-COR).

881 ***RNA integrity analysis***

882 FLS were plated in 6-well plates and transfected with either saRNA or subjected to mock transfection.
883 After 26-30 hours, cells were harvested by scraping in 350 µl RLT buffer (QIAGEN) supplemented with 10
884 µl/ml β-mercaptoethanol (Sigma). Cell lysates were homogenized using QIAshredder columns (QIAGEN),
885 and total RNA was extracted using the RNeasy Mini Kit (QIAGEN) according to the manufacturer's
886 instructions. RNA quantity and quality were initially assessed using a N60 nanophotometer (Implen).
887 Samples were aliquoted and stored at -80°C until further analysis. For detailed quality assessment,
888 samples were transported on dry ice and analyzed using the RNA Pico Kit on the 2100 Bioanalyzer
889 system (Agilent), performed by Cambridge Genomic Services. RNA Integrity Number (RIN) values were
890 determined for each sample, and the differences in RIN between saRNA-transfected and mock-
891 transfected conditions were calculated.

892 ***Bead-based immunoassay***

893 FLS were stained with BioTracker and seeded onto 6-well plates. After transfection, the saRNA-
894 lipofectamine complexes were replaced with 2 ml of fresh FLS media. Two days later, supernatants were
895 collected and stored at -80°C until analysis. On the day of analysis, the supernatant was thawed on ice,
896 and levels of 13 innate immune-related cytokines (IFN-γ, CXCL1, TNF-α, MCP-1, IL-12p70, CCL5, IL-1β,
897 CXCL10, GM-CSF, IL-10, IFN-β, IFN-α, and IL-6) were measured using the LEGENDplex Mouse Anti-
898 Virus Response Panel (740621, BioLegend) following the manufacturer's protocol. Samples were run in
899 duplicate. A custom 3D-printed PETG vacuum manifold (designed with Fusion 360) was used for vacuum
900 filtration, and beads were analyzed using a CytoPLEX LX flow cytometer (Beckman Coulter). Data
901 analysis was performed with the LEGENDplex Qognit Data Analysis Suite (BioLegend). To account for
902 differences in cell number between wells, cytokine levels were corrected based on the BioTracker signal
903 before transfection.

904 ***ML336 experiments***

905 ML336 (Cayman Chemical) was dissolved in DMSO (Sigma) at a stock concentration of 10 mM, and
906 aliquots were stored at -20°C. For treatments, ML336 was added to cell cultures at a final concentration
907 of 1 μM, while vehicle control cultures received 0.01% DMSO.

908 ***Statistical Analysis***

909 All statistical analyses were conducted using GraphPad Prism 9, with specific tests detailed in the
910 corresponding figure legends. All statistical tests were two-sided tests.

911

912 **DATA AVAILABILITY STATEMENT**

913 The code for the unmixing analysis is available at https://github.com/lariferg/spectral_unmixing.

914 The 3D printed vacuum manifold compatible with the LEGENDplex assay has been deposited in the NIH
915 3D print exchange (3DPX-021388).

916 All data needed to evaluate the conclusions in the paper are present in the paper, the Supplementary
917 Materials, and the Figshare repository http://doi.org/10.6084/m9.figshare.27091972.

918

919 **ACKNOWLEDGMENTS**

920 The authors gratefully acknowledge the Cambridge Advanced Imaging Centre, the flow cytometry facility
921 from the School of the Biological Sciences, and Cambridge Genomic Services for their support &
922 assistance in this work. The authors would like to thank Dr. Paul Miller for providing the pDx_mScarlet3
923 plasmid and Dr. Alex Cloake for providing the pIRES2-EGFP plasmid used in this study. T.K.L.
924 acknowledges support from a Horizon Europe Marie Skłodowska-Curie Actions European Postdoctoral
925 Fellowship (UKRI Guarantee) [EP/X023117/1]. A.R. and L.W.P. disclose support from AstraZeneca PhD
926 studentships [G115018 and G113502, respectively]. L.F. discloses support from funding provided by the
927 MRC Postdoctoral Training Scheme. E.St.J.S. acknowledges funding from the UKRI and Versus Arthritis
928 [MR/W002426/1] as part of the ADVANTAGE visceral pain consortium through the Advanced Pain
929 Discovery Platform (APDP) and the Wellcome Trust [225856/Z/22/Z].

930

931 **AUTHOR CONTRIBUTIONS**

932 Conceptualization, T.K.L. and E.St.J.S
933 Formal analysis: T.K.L., E.St.J.S.
934 Funding acquisition: E.St.J.S., T.K.L.
935 Investigation: T.K.L., A.R., L.W.P.
936 Methodology: T.K.L., T.A.
937 Resources: E.St.J.S., T.K.L.
938 Software: L.F.
939 Supervision: E.St.J.S., T.K.L.
940 Visualisation: T.K.L., E.St.J.S.
941 Writing—original draft: T.K.L.
942 Writing—reviewing & editing: E.St.J.S., L.F.

943

944 **DECLARATION OF INTERESTS**

945 Authors declare that they have no competing interests.

946

947 **KEYWORDS**

Self-amplifying RNA, alphavirus vectors, RNA replicons, fibroblast-like synoviocytes, double-stranded RNA sensors, nuclear factor kappa B, viral innate immune antagonists, RNA vaccines, RNA therapeutics

DECLARATION OF GENERATIVE AI AND AI-ASSISTED TECHNOLOGIES IN THE WRITING PROCESS

During the preparation of this work, the authors used OpenAI's ChatGPT to enhance clarity and flow of the writing. After using this tool, the authors reviewed and edited the content as needed and take full responsibility for the content of the publication.

REFERENCES

1. Frolov, I., Hoffman, T.A., Prágai, B.M., Dryga, S.A., Huang, H.V., Schlesinger, S., and Rice, C.M. (1996). Alphavirus-based expression vectors: strategies and applications. Proc Natl Acad Sci U S A *93*, 11371–11377.

2. Bloom, K., van den Berg, F., and Arbuthnot, P. (2021). Self-amplifying RNA vaccines for infectious diseases. Gene Ther *28*, 117–129. https://doi.org/10.1038/s41434-020-00204-y.

3. Pietilä, M.K., Hellström, K., and Ahola, T. (2017). Alphavirus polymerase and RNA replication. Virus Research *234*, 44–57. https://doi.org/10.1016/j.virusres.2017.01.007.

4. Maruggi, G., Zhang, C., Li, J., Ulmer, J.B., and Yu, D. (2019). mRNA as a Transformative Technology for Vaccine Development to Control Infectious Diseases. Mol Ther *27*, 757–772. https://doi.org/10.1016/j.ymthe.2019.01.020.

5. Akhrymuk, I., Frolov, I., and Frolova, E.I. (2016). Both RIG-I and MDA5 detect alphavirus replication in concentration-dependent mode. Virology *487*, 230–241. https://doi.org/10.1016/j.virol.2015.09.023.

6. Gong, Y., Yong, D., Liu, G., Xu, J., Ding, J., and Jia, W. (2024). A Novel Self-Amplifying mRNA with Decreased Cytotoxicity and Enhanced Protein Expression by Macrodomain Mutations. Advanced Science *n/a*, 2402936. https://doi.org/10.1002/advs.202402936.

7. Gorchakov, R., Frolova, E., Williams, B.R.G., Rice, C.M., and Frolov, I. (2004). PKR-Dependent and -Independent Mechanisms Are Involved in Translational Shutoff during Sindbis Virus Infection. Journal of Virology *78*, 8455–8467. https://doi.org/10.1128/jvi.78.16.8455-8467.2004.

8. Dominguez, F., Palchevska, O., Frolova, E.I., and Frolov, I. (2023). Alphavirus-based replicons demonstrate different interactions with host cells and can be optimized to increase protein expression. Journal of Virology *97*, e01225-23. https://doi.org/10.1128/jvi.01225-23.

9. Vanluchene, H., Gillon, O., Peynshaert, K., De Smedt, S.C., Sanders, N., Raemdonck, K., and Remaut, K. (2024). Less is more: Self-amplifying mRNA becomes self-killing upon dose escalation in immune-competent retinal cells. European Journal of Pharmaceutics and Biopharmaceutics *196*, 114204. https://doi.org/10.1016/j.ejpb.2024.114204.

984 10. Frolov, I., and Schlesinger, S. (1994). Comparison of the effects of Sindbis virus and Sindbis virus
985 replicons on host cell protein synthesis and cytopathogenicity in BHK cells. J Virol *68*, 1721–1727.
986 https://doi.org/10.1128/jvi.68.3.1721-1727.1994.

987 11. Terenzi, F., deVeer, M.J., Ying, H., Restifo, N.P., Williams, B.R., and Silverman, R.H. (1999). The
988 antiviral enzymes PKR and RNase L suppress gene expression from viral and non-viral based vectors.
989 Nucleic Acids Res *27*, 4369–4375. https://doi.org/10.1093/nar/27.22.4369.

990 12. Li, Y., Su, Z., Zhao, W., Zhang, X., Momin, N., Zhang, C., Wittrup, K.D., Dong, Y., Irvine, D.J., and
991 Weiss, R. (2020). Multifunctional oncolytic nanoparticles deliver self-replicating IL-12 RNA to
992 eliminate established tumors and prime systemic immunity. Nat Cancer *1*, 882–893.
993 https://doi.org/10.1038/s43018-020-0095-6.

994 13. Venticinque, L., and Meruelo, D. (2010). Sindbis viral vector induced apoptosis requires translational
995 inhibition and signaling through Mcl-1 and Bak. Mol Cancer *9*, 37. https://doi.org/10.1186/1476-
996 4598-9-37.

997 14. Mastrangelo, A.J., Hardwick, J.M., Bex, F., and Betenbaugh, M.J. (2000). Part I. Bcl-2 and Bcl-x(L)
998 limit apoptosis upon infection with alphavirus vectors. Biotechnol Bioeng *67*, 544–554.

999 15. Frolov, I., Agapov, E., Thomas A Hoffman, J., Prágai, B.M., Lippa, M., Schlesinger, S., and Rice, C.M.
1000 (1999). Selection of RNA Replicons Capable of Persistent Noncytopathic Replication in Mammalian
1001 Cells. Journal of Virology *73*, 3854. https://doi.org/10.1128/jvi.73.5.3854-3865.1999.

1002 16. Lundstrom, K., Abenavoli, A., Malgaroli, A., and Ehrengruber, M.U. (2003). Novel semliki forest virus
1003 vectors with reduced cytotoxicity and temperature sensitivity for long-term enhancement of
1004 transgene expression. Molecular Therapy *7*, 202–209. https://doi.org/10.1016/S1525-
1005 0016(02)00056-4.

1006 17. Pepini, T., Pulichino, A.-M., Carsillo, T., Carlson, A.L., Sari-Sarraf, F., Ramsauer, K., Debasitis, J.C.,
1007 Maruggi, G., Otten, G.R., Geall, A.J., et al. (2017). Induction of an IFN-Mediated Antiviral Response
1008 by a Self-Amplifying RNA Vaccine: Implications for Vaccine Design. The Journal of Immunology *198*,
1009 4012–4024. https://doi.org/10.4049/jimmunol.1601877.

1010 18. Blakney, A.K., McKay, P.F., Bouton, C.R., Hu, K., Samnuan, K., and Shattock, R.J. (2021). Innate
1011 Inhibiting Proteins Enhance Expression and Immunogenicity of Self-Amplifying RNA. Mol Ther *29*,
1012 1174–1185. https://doi.org/10.1016/j.ymthe.2020.11.011.

1013 19. Blakney, A.K., Ip, S., and Geall, A.J. (2021). An Update on Self-Amplifying mRNA Vaccine
1014 Development. Vaccines (Basel) *9*, 97. https://doi.org/10.3390/vaccines9020097.

1015 20. Minnaert, A.-K., Vanluchene, H., Verbeke, R., Lentacker, I., De Smedt, S.C., Raemdonck, K., Sanders,
1016 N.N., and Remaut, K. (2021). Strategies for controlling the innate immune activity of conventional
1017 and self-amplifying mRNA therapeutics: Getting the message across. Adv Drug Deliv Rev *176*,
1018 113900. https://doi.org/10.1016/j.addr.2021.113900.

1019 21. Erasmus, J.H., Archer, J., Fuerte-Stone, J., Khandhar, A.P., Voigt, E., Granger, B., Bombardi, R.G.,
1020 Govero, J., Tan, Q., Durnell, L.A., et al. (2020). Intramuscular Delivery of Replicon RNA Encoding

1021 ZIKV-117 Human Monoclonal Antibody Protects against Zika Virus Infection. Molecular Therapy
1022 Methods & Clinical Development *18*, 402–414. https://doi.org/10.1016/j.omtm.2020.06.011.

1023 22. Yoshioka, N., Gros, E., Li, H.-R., Kumar, S., Deacon, D.C., Maron, C., Muotri, A.R., Chi, N.C., Fu, X.-D.,
1024 Yu, B.D., et al. (2013). Efficient Generation of Human iPS Cells by a Synthetic Self-Replicative RNA.
1025 Cell Stem Cell *13*, 10.1016/j.stem.2013.06.001. https://doi.org/10.1016/j.stem.2013.06.001.

1026 23. Kim, Y.G., Baltabekova, A.Z., Zhiyenbay, E.E., Aksambayeva, A.S., Shagyrova, Z.S., Khannanov, R.,
1027 Ramanculov, E.M., and Shustov, A.V. (2017). Recombinant Vaccinia virus-coded interferon inhibitor
1028 B18R: Expression, refolding and a use in a mammalian expression system with a RNA-vector. PLOS
1029 ONE *12*, e0189308. https://doi.org/10.1371/journal.pone.0189308.

1030 24. McGee, J.E., Kirsch, J.R., Kenney, D., Cerbo, F., Chavez, E.C., Shih, T.-Y., Douam, F., Wong, W.W., and
1031 Grinstaff, M.W. (2024). Complete substitution with modified nucleotides in self-amplifying RNA
1032 suppresses the interferon response and increases potency. Nat Biotechnol, 1–7.
1033 https://doi.org/10.1038/s41587-024-02306-z.

1034 25. Zhong, Z., McCafferty, S., Opsomer, L., Wang, H., Huysmans, H., De Temmerman, J., Lienenklaus, S.,
1035 Portela Catani, J.P., Combes, F., and Sanders, N.N. (2021). Corticosteroids and cellulose purification
1036 improve, respectively, the in vivo translation and vaccination efficacy of sa-mRNAs. Molecular
1037 Therapy *29*, 1370–1381. https://doi.org/10.1016/j.ymthe.2021.01.023.

1038 26. Beissert, T., Koste, L., Perkovic, M., Walzer, K.C., Erbar, S., Selmi, A., Diken, M., Kreiter, S., Türeci, Ö.,
1039 and Sahin, U. (2017). Improvement of In Vivo Expression of Genes Delivered by Self-Amplifying RNA
1040 Using Vaccinia Virus Immune Evasion Proteins. Hum Gene Ther *28*, 1138–1146.
1041 https://doi.org/10.1089/hum.2017.121.

1042 27. Xue, Y., Zhang, Y., Zhong, Y., Du, S., Hou, X., Li, W., Li, H., Wang, S., Wang, C., Yan, J., et al. (2024).
1043 LNP-RNA-engineered adipose stem cells for accelerated diabetic wound healing. Nat Commun *15*,
1044 739. https://doi.org/10.1038/s41467-024-45094-5.

1045 28. Li, Y., Teague, B., Zhang, Y., Su, Z., Porter, E., Dobosh, B., Wagner, T., Irvine, D.J., and Weiss, R.
1046 (2019). In vitro evolution of enhanced RNA replicons for immunotherapy. Sci Rep *9*, 6932.
1047 https://doi.org/10.1038/s41598-019-43422-0.

1048 29. Merrick, W.C. (2004). Cap-dependent and cap-independent translation in eukaryotic systems. Gene
1049 *332*, 1–11. https://doi.org/10.1016/j.gene.2004.02.051.

1050 30. Yang, Y., and Wang, Z. (2019). IRES-mediated cap-independent translation, a path leading to hidden
1051 proteome. Journal of Molecular Cell Biology *11*, 911–919. https://doi.org/10.1093/jmcb/mjz091.

1052 31. Maglaviceanu, A., Wu, B., and Kapoor, M. (2021). Fibroblast-like synoviocytes: Role in synovial
1053 fibrosis associated with osteoarthritis. Wound Repair and Regeneration *29*, 642–649.
1054 https://doi.org/10.1111/wrr.12939.

1055 32. Mousavi, M.J., Karami, J., Aslani, S., Tahmasebi, M.N., Vaziri, A.S., Jamshidi, A., Farhadi, E., and
1056 Mahmoudi, M. (2021). Transformation of fibroblast-like synoviocytes in rheumatoid arthritis; from a
1057 friend to foe. Autoimmun Highlights *12*, 3. https://doi.org/10.1186/s13317-020-00145-x.

1058 33. Honig, M.G., and Hume, R.I. (1986). Fluorescent carbocyanine dyes allow living neurons of identified
1059 origin to be studied in long-term cultures. J Cell Biol *103*, 171–187.
1060 https://doi.org/10.1083/jcb.103.1.171.

1061 34. Bertrand, R., Solary, E., O'Connor, P., Kohn, K.W., and Pommier, Y. (1994). Induction of a Common
1062 Pathway of Apoptosis by Staurosporine. Experimental Cell Research *211*, 314–321.
1063 https://doi.org/10.1006/excr.1994.1093.

1064 35. Rehwinkel, J., and Gack, M.U. (2020). RIG-I-like receptors: their regulation and roles in RNA sensing.
1065 Nat Rev Immunol *20*, 537–551. https://doi.org/10.1038/s41577-020-0288-3.

1066 36. Junior, A.G.D., Sampaio, N.G., and Rehwinkel, J. (2019). A Balancing Act: MDA5 in Antiviral Immunity
1067 and Autoinflammation. Trends in Microbiology *27*, 75–85.
1068 https://doi.org/10.1016/j.tim.2018.08.007.

1069 37. Gal-Ben-Ari, S., Barrera, I., Ehrlich, M., and Rosenblum, K. (2019). PKR: A Kinase to Remember.
1070 Front. Mol. Neurosci. *11*. https://doi.org/10.3389/fnmol.2018.00480.

1071 38. Silverman, R.H. (2007). Viral Encounters with 2′,5′-Oligoadenylate Synthetase and RNase L during
1072 the Interferon Antiviral Response. Journal of Virology *81*, 12720–12729.
1073 https://doi.org/10.1128/jvi.01471-07.

1074 39. Szczerba, M., Subramanian, S., Trainor, K., McCaughan, M., Kibler, K.V., and Jacobs, B.L. (2022).
1075 Small Hero with Great Powers: Vaccinia Virus E3 Protein and Evasion of the Type I IFN Response.
1076 Biomedicines *10*, 235. https://doi.org/10.3390/biomedicines10020235.

1077 40. Kalveram, B., and Ikegami, T. (2013). Toscana Virus NSs Protein Promotes Degradation of Double-
1078 Stranded RNA-Dependent Protein Kinase. J Virol *87*, 3710–3718. https://doi.org/10.1128/JVI.02506-
1079 12.

1080 41. Drappier, M., Jha, B.K., Stone, S., Elliott, R., Zhang, R., Vertommen, D., Weiss, S.R., Silverman, R.H.,
1081 and Michiels, T. (2018). A novel mechanism of RNase L inhibition: Theiler's virus L* protein prevents
1082 2-5A from binding to RNase L. PLoS Pathog *14*, e1006989.
1083 https://doi.org/10.1371/journal.ppat.1006989.

1084 42. Liu, Z., Chen, O., Wall, J.B.J., Zheng, M., Zhou, Y., Wang, L., Ruth Vaseghi, H., Qian, L., and Liu, J.
1085 (2017). Systematic comparison of 2A peptides for cloning multi-genes in a polycistronic vector. Sci
1086 Rep *7*, 2193. https://doi.org/10.1038/s41598-017-02460-2.

1087 43. Costigan, A., Hollville, E., and Martin, S.J. (2023). Discriminating Between Apoptosis, Necrosis,
1088 Necroptosis, and Ferroptosis by Microscopy and Flow Cytometry. Current Protocols *3*, e951.
1089 https://doi.org/10.1002/cpz1.951.

1090 44. Liu, Q., Huang, J., Xia, J., Liang, Y., and Li, G. (2022). Tracking tools of extracellular vesicles for
1091 biomedical research. Front. Bioeng. Biotechnol. *10*. https://doi.org/10.3389/fbioe.2022.943712.

1092 45. Chiaradia, E., Tancini, B., Emiliani, C., Delo, F., Pellegrino, R.M., Tognoloni, A., Urbanelli, L., and
1093 Buratta, S. (2021). Extracellular Vesicles under Oxidative Stress Conditions: Biological Properties and
1094 Physiological Roles. Cells *10*, 1763. https://doi.org/10.3390/cells10071763.

1095 46. van Genderen, H., Kenis, H., Lux, P., Ungeth, L., Maassen, C., Deckers, N., Narula, J., Hofstra, L., and
1096 Reutelingsperger, C. (2006). In vitro measurement of cell death with the annexin A5 affinity assay.
1097 Nat Protoc *1*, 363–367. https://doi.org/10.1038/nprot.2006.55.

1098 47. Crowley, L.C., Marfell, B.J., Scott, A.P., and Waterhouse, N.J. (2016). Quantitation of Apoptosis and
1099 Necrosis by Annexin V Binding, Propidium Iodide Uptake, and Flow Cytometry. Cold Spring Harb
1100 Protoc *2016*. https://doi.org/10.1101/pdb.prot087288.

1101 48. Chan, L.L., Wilkinson, A.R., Paradis, B.D., and Lai, N. (2012). Rapid Image-based Cytometry for
1102 Comparison of Fluorescent Viability Staining Methods. J Fluoresc *22*, 1301–1311.
1103 https://doi.org/10.1007/s10895-012-1072-y.

1104 49. Baird, T.D., and Wek, R.C. (2012). Eukaryotic Initiation Factor 2 Phosphorylation and Translational
1105 Control in Metabolism. Advances in Nutrition *3*, 307. https://doi.org/10.3945/an.112.002113.

1106 50. Mars, J.-C., Culjkovic-Kraljacic, B., and Borden, K.L.B. (2024). eIF4E orchestrates mRNA processing,
1107 RNA export and translation to modify specific protein production. Nucleus *15*, 2360196.
1108 https://doi.org/10.1080/19491034.2024.2360196.

1109 51. Burke, J.M., Moon, S.L., Matheny, T., and Parker, R. (2019). RNase L Reprograms Translation by
1110 Widespread mRNA Turnover Escaped by Antiviral mRNAs. Molecular Cell *75*, 1203-1217.e5.
1111 https://doi.org/10.1016/j.molcel.2019.07.029.

1112 52. Burke, J.M., Gilchrist, A.R., Sawyer, S.L., and Parker, R. (2021). RNase L limits host and viral protein
1113 synthesis via inhibition of mRNA export. Science Advances *7*, eabh2479.
1114 https://doi.org/10.1126/sciadv.abh2479.

1115 53. Donovan, J., Rath, S., Kolet-Mandrikov, D., and Korennykh, A. (2017). Rapid RNase L-driven arrest of
1116 protein synthesis in the dsRNA response without degradation of translation machinery. RNA *23*,
1117 1660–1671. https://doi.org/10.1261/rna.062000.117.

1118 54. Whelan, J.N., Li, Y., Silverman, R.H., and Weiss, S.R. (2019). Zika Virus Production Is Resistant to
1119 RNase L Antiviral Activity. J Virol *93*, e00313-19. https://doi.org/10.1128/JVI.00313-19.

1120 55. Paul, D., and Bartenschlager, R. (2013). Architecture and biogenesis of plus-strand RNA virus
1121 replication factories. World J Virol *2*, 32–48. https://doi.org/10.5501/wjv.v2.i2.32.

1122 56. Schroeder, A., Mueller, O., Stocker, S., Salowsky, R., Leiber, M., Gassmann, M., Lightfoot, S., Menzel,
1123 W., Granzow, M., and Ragg, T. (2006). The RIN: an RNA integrity number for assigning integrity
1124 values to RNA measurements. BMC Molecular Biology *7*, 3. https://doi.org/10.1186/1471-2199-7-3.

1125 57. Santoro, M.G., Rossi, A., and Amici, C. (2003). NF-κB and virus infection: who controls whom. The
1126 EMBO Journal *22*, 2552–2560. https://doi.org/10.1093/emboj/cdg267.

1127 58. Mitchell, J.P., and Carmody, R.J. (2018). Chapter Two - NF-κB and the Transcriptional Control of
1128 Inflammation. In International Review of Cell and Molecular Biology Transcriptional Gene Regulation
1129 in Health and Disease., F. Loos, ed. (Academic Press), pp. 41–84.
1130 https://doi.org/10.1016/bs.ircmb.2017.07.007.

1131 59. Lee, Y.-R., Kweon, S.-H., Kwon, K.-B., Park, J.-W., Yoon, T.-R., and Park, B.-H. (2009). Inhibition of IL-
1132 1β-mediated inflammatory responses by the IκBα super-repressor in human fibroblast-like
1133 synoviocytes. Biochemical and Biophysical Research Communications *378*, 90–94.
1134 https://doi.org/10.1016/j.bbrc.2008.11.002.

1135 60. Brown, K., Gerstberger, S., Carlson, L., Franzoso, G., and Siebenlist, U. (1995). Control of IκB-α
1136 Proteolysis by Site-Specific, Signal-Induced Phosphorylation. Science *267*, 1485–1488.
1137 https://doi.org/10.1126/science.7878466.

1138 61. Yan, X., Liu, Z., and Chen, Y. (2009). Regulation of TGF-β signaling by Smad7. Acta Biochimica et
1139 Biophysica Sinica *41*, 263–272. https://doi.org/10.1093/abbs/gmp018.

1140 62. Sobah, M.L., Liongue, C., and Ward, A.C. (2021). SOCS Proteins in Immunity, Inflammatory Diseases,
1141 and Immune-Related Cancer. Front Med (Lausanne) *8*, 727987.
1142 https://doi.org/10.3389/fmed.2021.727987.

1143 63. Dimitriou, I.D., Clemenza, L., Scotter, A.J., Chen, G., Guerra, F.M., and Rottapel, R. (2008). Putting
1144 out the fire: coordinated suppression of the innate and adaptive immune systems by SOCS1 and
1145 SOCS3 proteins. Immunological Reviews *224*, 265–283. https://doi.org/10.1111/j.1600-
1146 065X.2008.00659.x.

1147 64. Blumer, T., Coto-Llerena, M., Duong, F.H.T., and Heim, M.H. (2017). SOCS1 is an inducible negative
1148 regulator of interferon λ (IFN-λ)-induced gene expression in vivo. J Biol Chem *292*, 17928–17938.
1149 https://doi.org/10.1074/jbc.M117.788877.

1150 65. Bauer, S., Jendro, M.C., Wadle, A., Kleber, S., Stenner, F., Dinser, R., Reich, A., Faccin, E., Gödde, S.,
1151 Dinges, H., et al. (2006). Fibroblast activation protein is expressed by rheumatoid myofibroblast-like
1152 synoviocytes. Arthritis Res Ther *8*, R171. https://doi.org/10.1186/ar2080.

1153 66. Zhang, H.E., Hamson, E.J., Koczorowska, M.M., Tholen, S., Chowdhury, S., Bailey, C.G., Lay, A.J.,
1154 Twigg, S.M., Lee, Q., Roediger, B., et al. (2019). Identification of Novel Natural Substrates of
1155 Fibroblast Activation Protein-alpha by Differential Degradomics and Proteomics. Mol Cell
1156 Proteomics *18*, 65–85. https://doi.org/10.1074/mcp.RA118.001046.

1157 67. Fan, A., Wu, G., Wang, J., Lu, L., Wang, J., Wei, H., Sun, Y., Xu, Y., Mo, C., Zhang, X., et al. (2023).
1158 Inhibition of fibroblast activation protein ameliorates cartilage matrix degradation and osteoarthritis
1159 progression. Bone Res *11*, 1–12. https://doi.org/10.1038/s41413-022-00243-8.

1160 68. Croft, A.P., Campos, J., Jansen, K., Turner, J.D., Marshall, J., Attar, M., Savary, L., Wehmeyer, C.,
1161 Naylor, A.J., Kemble, S., et al. (2019). Distinct fibroblast subsets drive inflammation and damage in
1162 arthritis. Nature *570*, 246–251. https://doi.org/10.1038/s41586-019-1263-7.

1163 69. Boyd, D.F., Allen, E.K., Randolph, A.G., Guo, X.J., Weng, Y., Sanders, C.J., Bajracharya, R., Lee, N.K.,
1164 Guy, C.S., Vogel, P., et al. (2020). Exuberant fibroblast activity compromises lung function via
1165 ADAMTS-4. Nature *587*, 466–471. https://doi.org/10.1038/s41586-020-2877-5.

1166 70. Krausgruber, T., Fortelny, N., Fife-Gernedl, V., Senekowitsch, M., Schuster, L.C., Lercher, A., Nemc,
1167 A., Schmidl, C., Rendeiro, A.F., Bergthaler, A., et al. (2020). Structural cells are key regulators of

1168 organ-specific immune response. Nature *583*, 296–302. https://doi.org/10.1038/s41586-020-2424-
1169 4.

1170 71. Nagata, L.P., Wong, J.P., Hu, W., and Wu, J.Q. (2013). Vaccines and Therapeutics for the Encephalitic
1171 Alphaviruses. Future Virology *8*, 661–674. https://doi.org/10.2217/fvl.13.42.

1172 72. Chung, D., Schroeder, C.E., Sotsky, J., Yao, T., Roy, S., Smith, R.A., Tower, N.A., Noah, J.W., McKellip,
1173 S., Sosa, M., et al. (2010). ML336: Development of Quinazolinone-Based Inhibitors Against
1174 Venezuelan Equine Encephalitis Virus (VEEV). In Probe Reports from the NIH Molecular Libraries
1175 Program (National Center for Biotechnology Information (US)).

1176 73. Frolova, E.I., Palchevska, O., Dominguez, F., and Frolov, I. Alphavirus-induced transcriptional and
1177 translational shutoffs play major roles in blocking the formation of stress granules. J Virol *97*,
1178 e00979-23. https://doi.org/10.1128/jvi.00979-23.

1179 74. Berglund, P., Finzi, D., Bennink, J.R., and Yewdell, J.W. (2007). Viral Alteration of Cellular
1180 Translational Machinery Increases Defective Ribosomal Products. Journal of Virology *81*, 7220–
1181 7229. https://doi.org/10.1128/jvi.00137-07.

1182 75. Fros, J.J., and Pijlman, G.P. (2016). Alphavirus Infection: Host Cell Shut-Off and Inhibition of Antiviral
1183 Responses. Viruses *8*, 166. https://doi.org/10.3390/v8060166.

1184 76. Fernandez, J., Yaman, I., Sarnow, P., Snider, M.D., and Hatzoglou, M. (2002). Regulation of Internal
1185 Ribosomal Entry Site-mediated Translation by Phosphorylation of the Translation Initiation Factor
1186 eIF2α*. Journal of Biological Chemistry *277*, 19198–19205.
1187 https://doi.org/10.1074/jbc.M201052200.

1188 77. Scheper, G.C., and Proud, C.G. (2002). Does phosphorylation of the cap-binding protein eIF4E play a
1189 role in translation initiation? European Journal of Biochemistry *269*, 5350–5359.
1190 https://doi.org/10.1046/j.1432-1033.2002.03291.x.

1191 78. Dyer, J.R., Michel, S., Lee, W., Castellucci, V.F., Wayne, N.L., and Sossin, W.S. (2003). An activity-
1192 dependent switch to cap-independent translation triggered by eIF4E dephosphorylation. Nat
1193 Neurosci *6*, 219–220. https://doi.org/10.1038/nn1018.

1194 79. Chang, C., Music, N., Cheung, M., Rossignol, E., Bedi, S., Patel, H., Safari, M., Lee, C., Otten, G.R.,
1195 Settembre, E.C., et al. (2022). Self-amplifying mRNA bicistronic influenza vaccines raise cross-
1196 reactive immune responses in mice and prevent infection in ferrets. Molecular Therapy Methods &
1197 Clinical Development *27*, 195–205. https://doi.org/10.1016/j.omtm.2022.09.013.

1198 80. Koch, A., Aguilera, L., Morisaki, T., Munsky, B., and Stasevich, T.J. (2020). Quantifying the dynamics
1199 of IRES and cap translation with single-molecule resolution in live cells. Nat Struct Mol Biol *27*,
1200 1095–1104. https://doi.org/10.1038/s41594-020-0504-7.

1201 81. Ho, C.K., and Shuman, S. (1996). Physical and Functional Characterization of the Double-Stranded
1202 RNA Binding Protein Encoded by the Vaccinia Virus E3 Gene. Virology *217*, 272–284.
1203 https://doi.org/10.1006/viro.1996.0114.

1204 82. Dueck, K.J., Hu, Y. (Sandy), Chen, P., Deschambault, Y., Lee, J., Varga, J., and Cao, J. (2015).
1205 Mutational Analysis of Vaccinia Virus E3 Protein: the Biological Functions Do Not Correlate with Its
1206 Biochemical Capacity To Bind Double-Stranded RNA. Journal of Virology *89*, 5382–5394.
1207 https://doi.org/10.1128/jvi.03288-14.

1208 83. Leitner, W.W., Hwang, L.N., Bergmann-Leitner, E.S., Finkelstein, S.E., Frank, S., and Restifo, N.P.
1209 (2004). Apoptosis is essential for the increased efficacy of alphaviral replicase-based DNA vaccines.
1210 Vaccine *22*, 1537–1544. https://doi.org/10.1016/j.vaccine.2003.10.013.

1211 84. Wu, Y.-Y., Sun, T.-K., Chen, M.-S., Munir, M., and Liu, H.-J. (2023). Oncolytic viruses-modulated
1212 immunogenic cell death, apoptosis and autophagy linking to virotherapy and cancer immune
1213 response. Front. Cell. Infect. Microbiol. *13*. https://doi.org/10.3389/fcimb.2023.1142172.

1214 85. Li, Y., Banerjee, S., Wang, Y., Goldstein, S.A., Dong, B., Gaughan, C., Silverman, R.H., and Weiss, S.R.
1215 (2016). Activation of RNase L is dependent on OAS3 expression during infection with diverse human
1216 viruses. Proc Natl Acad Sci U S A *113*, 2241–2246. https://doi.org/10.1073/pnas.1519657113.

1217 86. Zuo, W., Wakimoto, M., Kozaiwa, N., Shirasaka, Y., Oh, S.-W., Fujiwara, S., Miyachi, H., Kogure, A.,
1218 Kato, H., and Fujita, T. (2022). PKR and TLR3 trigger distinct signals that coordinate the induction of
1219 antiviral apoptosis. Cell Death Dis *13*, 1–15. https://doi.org/10.1038/s41419-022-05101-3.

1220 87. Xu, C., Gamil, A.A.A., Munang'andu, H.M., and Evensen, Ø. (2018). Apoptosis Induction by dsRNA-
1221 Dependent Protein Kinase R (PKR) in EPC Cells via Caspase 8 and 9 Pathways. Viruses *10*, 526.
1222 https://doi.org/10.3390/v10100526.

1223 88. Gil, J., and Esteban, M. (2000). The interferon-induced protein kinase (PKR), triggers apoptosis
1224 through FADD-mediated activation of caspase 8 in a manner independent of Fas and TNF-α
1225 receptors. Oncogene *19*, 3665–3674. https://doi.org/10.1038/sj.onc.1203710.

1226 89. Zhang, P., and Samuel, C.E. (2007). Protein Kinase PKR Plays a Stimulus- and Virus-Dependent Role
1227 in Apoptotic Death and Virus Multiplication in Human Cells. Journal of Virology *81*, 8192–8200.
1228 https://doi.org/10.1128/jvi.00426-07.

1229 90. Roretz, C. von, and Gallouzi, I.-E. (2010). Protein Kinase RNA/FADD/Caspase-8 Pathway Mediates
1230 the Proapoptotic Activity of the RNA-binding Protein Human Antigen R (HuR). The Journal of
1231 Biological Chemistry *285*, 16806. https://doi.org/10.1074/jbc.M109.087320.

1232 91. Xi, J., Snieckute, G., Martínez, J.F., Arendrup, F.S.W., Asthana, A., Gaughan, C., Lund, A.H., Bekker-
1233 Jensen, S., and Silverman, R.H. (2024). Initiation of a ZAKα-dependent ribotoxic stress response by
1234 the innate immunity endoribonuclease RNase L. Cell Reports *43*.
1235 https://doi.org/10.1016/j.celrep.2024.113998.

1236 92. Guydosh, N.R., Kimmig, P., Walter, P., and Green, R. (2017). Regulated Ire1-dependent mRNA decay
1237 requires no-go mRNA degradation to maintain endoplasmic reticulum homeostasis in S. pombe.
1238 eLife *6*, e29216. https://doi.org/10.7554/eLife.29216.

1239 93. Snieckute, G., Genzor, A.V., Vind, A.C., Ryder, L., Stoneley, M., Chamois, S., Dreos, R., Nordgaard, C.,
1240 Sass, F., Blasius, M., et al. (2022). Ribosome stalling is a signal for metabolic regulation by the

1241 ribotoxic stress response. Cell Metab *34*, 2036-2046.e8.
1242 https://doi.org/10.1016/j.cmet.2022.10.011.

1243 94. Li, G., Xiang, Y., Sabapathy, K., and Silverman, R.H. (2004). An Apoptotic Signaling Pathway in the
1244 Interferon Antiviral Response Mediated by RNase L and c-Jun NH2-terminal Kinase *. Journal of
1245 Biological Chemistry *279*, 1123–1131. https://doi.org/10.1074/jbc.M305893200.

1246 95. Samuel, C.E., Kuhen, K.L., George, C.X., Ortega, L.G., Rende-Fournier, R., and Tanaka, H. (1997). The
1247 PKR protein kinase--an interferon-inducible regulator of cell growth and differentiation. Int J
1248 Hematol *65*, 227–237. https://doi.org/10.1016/s0925-5710(96)00544-0.

1249 96. Iordanov, M.S., Wong, J., Bell, J.C., and Magun, B.E. (2001). Activation of NF-κB by Double-Stranded
1250 RNA (dsRNA) in the Absence of Protein Kinase R and RNase L Demonstrates the Existence of Two
1251 Separate dsRNA-Triggered Antiviral Programs. Molecular and Cellular Biology *21*, 61–72.
1252 https://doi.org/10.1128/MCB.21.1.61-72.2001.

1253 97. Herdy, B., Jaramillo, M., Svitkin, Y.V., Rosenfeld, A.B., Kobayashi, M., Walsh, D., Alain, T., Sean, P.,
1254 Robichaud, N., Topisirovic, I., et al. (2012). Translational control of the activation of transcription
1255 factor NF-κB and production of type I interferon by phosphorylation of the translation factor eIF4E.
1256 Nat Immunol *13*, 543–550. https://doi.org/10.1038/ni.2291.

1257 98. Liu, T., Zhang, L., Joo, D., and Sun, S.-C. (2017). NF-κB signaling in inflammation. Sig Transduct Target
1258 Ther *2*, 1–9. https://doi.org/10.1038/sigtrans.2017.23.

1259 99. Luo, J.-L., Kamata, H., and Karin, M. (2005). IKK/NF-κB signaling: balancing life and death – a new
1260 approach to cancer therapy. Journal of Clinical Investigation *115*, 2625–2632.
1261 https://doi.org/10.1172/JCI26322.

1262 100. Miagkov, A.V., Kovalenko, D.V., Brown, C.E., Didsbury, J.R., Cogswell, J.P., Stimpson, S.A.,
1263 Baldwin, A.S., and Makarov, S.S. (1998). NF-κB activation provides the potential link between
1264 inflammation and hyperplasia in the arthritic joint. Proceedings of the National Academy of Sciences
1265 *95*, 13859–13864. https://doi.org/10.1073/pnas.95.23.13859.

1266 101. Zhang, H.G., Huang, N., Liu, D., Bilbao, L., Zhang, X., Yang, P., Zhou, T., Curiel, D.T., and Mountz,
1267 J.D. (2000). Gene therapy that inhibits nuclear translocation of nuclear factor kappaB results in
1268 tumor necrosis factor alpha-induced apoptosis of human synovial fibroblasts. Arthritis Rheum *43*,
1269 1094–1105. https://doi.org/10.1002/1529-0131(200005)43:5<1094::AID-ANR20>3.0.CO;2-V.

1270 102. Xu, Y., Bialik, S., Jones, B.E., Iimuro, Y., Kitsis, R.N., Srinivasan, A., Brenner, D.A., and Czaja, M.J.
1271 (1998). NF-kappaB inactivation converts a hepatocyte cell line TNF-alpha response from
1272 proliferation to apoptosis. Am J Physiol *275*, C1058-1066.
1273 https://doi.org/10.1152/ajpcell.1998.275.4.C1058.

1274 103. Sago, C.D., Krupczak, B.R., Lokugamage, M.P., Gan, Z., and Dahlman, J.E. (2019). Cell Subtypes
1275 Within the Liver Microenvironment Differentially Interact with Lipid Nanoparticles. Cellular and
1276 Molecular Bioengineering *12*, 389. https://doi.org/10.1007/s12195-019-00573-4.

1277 104. Yamamura, Y., Hua, X., Bergelson, S., and Lodish, H.F. (2000). Critical Role of Smads and AP-1
1278 Complex in Transforming Growth Factor-β-dependent Apoptosis. Journal of Biological Chemistry
1279 *275*, 36295–36302. https://doi.org/10.1074/jbc.M006023200.

1280 105. Patil, S., Wildey, G.M., Brown, T.L., Choy, L., Derynck, R., and Howe, P.H. (2000). Smad7 is
1281 induced by CD40 and protects WEHI 231 B-lymphocytes from transforming growth factor-beta -
1282 induced growth inhibition and apoptosis. J Biol Chem *275*, 38363–38370.
1283 https://doi.org/10.1074/jbc.M004861200.

1284 106. Zitzmann, K., Brand, S., De Toni, E.N., Baehs, S., Göke, B., Meinecke, J., Spöttl, G., Meyer,
1285 H.H.H.D., and Auernhammer, C.J. (2007). SOCS1 Silencing Enhances Antitumor Activity of Type I IFNs
1286 by Regulating Apoptosis in Neuroendocrine Tumor Cells. Cancer Research *67*, 5025–5032.
1287 https://doi.org/10.1158/0008-5472.CAN-06-2575.

1288 107. Mann-Chandler, M.N., Kashyap, M., Wright, H.V., Norozian, F., Barnstein, B.O., Gingras, S.,
1289 Parganas, E., and Ryan, J.J. (2005). IFN-γ Induces Apoptosis in Developing Mast Cells1. The Journal of
1290 Immunology *175*, 3000–3005. https://doi.org/10.4049/jimmunol.175.5.3000.

1291 108. Kimura, A., Naka, T., Nagata, S., Kawase, I., and Kishimoto, T. (2004). SOCS-1 suppresses TNF-
1292 alpha-induced apoptosis through the regulation of Jak activation. Int Immunol *16*, 991–999.
1293 https://doi.org/10.1093/intimm/dxh102.

1294 109. Madonna, S., Scarponi, C., Pallotta, S., Cavani, A., and Albanesi, C. (2012). Anti-apoptotic effects
1295 of suppressor of cytokine signaling 3 and 1 in psoriasis. Cell Death Dis *3*, e334–e334.
1296 https://doi.org/10.1038/cddis.2012.69.

1297 110. Yan, L., Tang, Q., Shen, D., Peng, S., Zheng, Q., Guo, H., Jiang, M., and Deng, W. (2008). SOCS-1
1298 Inhibits TNF-α-Induced Cardiomyocyte Apoptosis via ERK1/2 Pathway Activation. Inflammation *31*,
1299 180–188. https://doi.org/10.1007/s10753-008-9063-5.

1300 111. Goker Bagca, B., and Biray Avci, C. (2020). The potential of JAK/STAT pathway inhibition by
1301 ruxolitinib in the treatment of COVID-19. Cytokine & Growth Factor Reviews *54*, 51–61.
1302 https://doi.org/10.1016/j.cytogfr.2020.06.013.

1303 112. Liau, N.P.D., Laktyushin, A., Lucet, I.S., Murphy, J.M., Yao, S., Whitlock, E., Callaghan, K., Nicola,
1304 N.A., Kershaw, N.J., and Babon, J.J. (2018). The molecular basis of JAK/STAT inhibition by SOCS1. Nat
1305 Commun *9*, 1558. https://doi.org/10.1038/s41467-018-04013-1.

1306 113. Skidmore, A.M., Adcock, R.S., Jonsson, C.B., Golden, J.E., and Chung, D.-H. (2020). Benzamidine
1307 ML336 inhibits plus and minus strand RNA synthesis of Venezuelan equine encephalitis virus
1308 without affecting host RNA production. Antiviral Research *174*, 104674.
1309 https://doi.org/10.1016/j.antiviral.2019.104674.

1310 114. Schroeder, C.E., Yao, T., Sotsky, J., Smith, R.A., Roy, S., Chu, Y.-K., Guo, H., Tower, N.A., Noah,
1311 J.W., McKellip, S., et al. (2014). Development of (E)-2-((1,4-Dimethylpiperazin-2-ylidene)amino)-5-
1312 nitro-N-phenylbenzamide, ML336: Novel 2-Amidinophenylbenzamides as Potent Inhibitors of
1313 Venezuelan Equine Encephalitis Virus. J. Med. Chem. *57*, 8608–8621.
1314 https://doi.org/10.1021/jm501203v.

1315 115. Tregoning, J.S., Stirling, D.C., Wang, Z., Flight, K.E., Brown, J.C., Blakney, A.K., McKay, P.F.,
1316 Cunliffe, R.F., Murugaiah, V., Fox, C.B., et al. (2023). Formulation, inflammation, and RNA sensing
1317 impact the immunogenicity of self-amplifying RNA vaccines. Molecular Therapy Nucleic Acids *31*,
1318 29–42. https://doi.org/10.1016/j.omtn.2022.11.024.

1319 116. Bathula, N.V., Friesen, J.J., Casmil, I.C., Wayne, C.J., Liao, S., Soriano, S.K.V., Ho, C.H., Strumpel,
1320 A., and Blakney, A.K. (2024). Delivery vehicle and route of administration influences self-amplifying
1321 RNA biodistribution, expression kinetics, and reactogenicity. Journal of Controlled Release *374*, 28–
1322 38. https://doi.org/10.1016/j.jconrel.2024.07.078.

1323 117. Oda, Y., Kumagai, Y., Kanai, M., Iwama, Y., Okura, I., Minamida, T., Yagi, Y., Kurosawa, T.,
1324 Greener, B., Zhang, Y., et al. (2024). Immunogenicity and safety of a booster dose of a self-
1325 amplifying RNA COVID-19 vaccine (ARCT-154) versus BNT162b2 mRNA COVID-19 vaccine: a double-
1326 blind, multicentre, randomised, controlled, phase 3, non-inferiority trial. The Lancet Infectious
1327 Diseases *24*, 351–360. https://doi.org/10.1016/S1473-3099(23)00650-3.

1328 118. Saraf, A., Gurjar, R., Kaviraj, S., Kulkarni, A., Kumar, D., Kulkarni, R., Virkar, R., Krishnan, J., Yadav,
1329 A., Baranwal, E., et al. (2024). An Omicron-specific, self-amplifying mRNA booster vaccine for COVID-
1330 19: a phase 2/3 randomized trial. Nat Med *30*, 1363–1372. https://doi.org/10.1038/s41591-024-
1331 02955-2.

1332 119. Roman-Blas, J.A., and Jimenez, S.A. (2006). NF-κB as a potential therapeutic target in
1333 osteoarthritis and rheumatoid arthritis. Osteoarthritis and Cartilage *14*, 839–848.
1334 https://doi.org/10.1016/j.joca.2006.04.008.

1335 120. Shen, J., Li, S., and Chen, D. (2014). TGF-β signaling and the development of osteoarthritis. Bone
1336 Res *2*, 1–7. https://doi.org/10.1038/boneres.2014.2.

1337 121. Zhou, Q., Ren, Q., Jiao, L., Huang, J., Yi, J., Chen, J., Lai, J., Ji, G., and Zheng, T. (2022). The
1338 potential roles of JAK/STAT signaling in the progression of osteoarthritis. Front. Endocrinol. *13*.
1339 https://doi.org/10.3389/fendo.2022.1069057.

1340 122. Blackwell, N.M., Sembi, P., Newson, J.S., Lawrence, T., Gilroy, D.W., and Kabouridis, P.S. (2004).
1341 Reduced infiltration and increased apoptosis of leukocytes at sites of inflammation by systemic
1342 administration of a membrane-permeable IκBα repressor. Arthritis & Rheumatism *50*, 2675–2684.
1343 https://doi.org/10.1002/art.20467.

1344 123. Chen, S.-Y., Shiau, A.-L., Wu, C.-L., and Wang, C.-R. (2016). Intraarticular overexpression of
1345 Smad7 ameliorates experimental arthritis. Sci Rep *6*, 35163. https://doi.org/10.1038/srep35163.

1346 124. Ha, Y.-J., Choi, Y.S., Kang, E.H., Shin, K., Kim, T.K., Song, Y.W., and Lee, Y.J. (2016). SOCS1
1347 suppresses IL-1β-induced C/EBPβ expression via transcriptional regulation in human chondrocytes.
1348 Exp Mol Med *48*, e241–e241. https://doi.org/10.1038/emm.2016.47.

1349 125. Freppel, W., Lim, E.X.Y., Rudd, P.A., and Herrero, L.J. (2024). Synoviocytes assist in modulating
1350 the effect of Ross River virus infection in micromass-cultured primary human chondrocytes. J Med
1351 Microbiol *73*, 001859. https://doi.org/10.1099/jmm.0.001859.

1352 126. Legros, V., Belarbi, E., Jeannin, P., Kümmerer, B., Hardy, D., Desprès, P., Gessain, A., Roques, P.,
1353 Ceccaldi, P.-E., and Choumet, V. (2024). A recombinant CHIKV-NLuc virus identifies chondrocytes as
1354 target of Chikungunya virus in a immunocompetent mouse model. Preprint at bioRxiv,
1355 https://doi.org/10.1101/2024.05.20.594924 https://doi.org/10.1101/2024.05.20.594924.

1356 127. Wäldele, S., Koers-Wunrau, C., Beckmann, D., Korb-Pap, A., Wehmeyer, C., Pap, T., and Dankbar,
1357 B. (2015). Deficiency of fibroblast activation protein alpha ameliorates cartilage destruction in
1358 inflammatory destructive arthritis. Arthritis Res Ther *17*, 12. https://doi.org/10.1186/s13075-015-
1359 0524-6.

1360 128. Petrakova, O., Volkova, E., Gorchakov, R., Paessler, S., Kinney, R.M., and Frolov, I. (2005).
1361 Noncytopathic Replication of Venezuelan Equine Encephalitis Virus and Eastern Equine Encephalitis
1362 Virus Replicons in Mammalian Cells. J Virol *79*, 7597–7608. https://doi.org/10.1128/JVI.79.12.7597-
1363 7608.2005.

1364 129. Hariri, F., Arguello, M., Volpon, L., Culjkovic-Kraljacic, B., Nielsen, T.H., Hiscott, J., Mann, K.K.,
1365 and Borden, K.L.B. (2013). The eukaryotic translation initiation factor eIF4E is a direct transcriptional
1366 target of NF-κB and is aberrantly regulated in acute myeloid leukemia. Leukemia *27*, 2047–2055.
1367 https://doi.org/10.1038/leu.2013.73.

1368 130. Uttam, S., Wong, C., Price, T.J., and Khoutorsky, A. (2018). eIF4E-Dependent Translational
1369 Control: A Central Mechanism for Regulation of Pain Plasticity. Front Genet *9*, 470.
1370 https://doi.org/10.3389/fgene.2018.00470.

1371 131. Siddiqui, N., and Sonenberg, N. (2015). Signalling to eIF4E in cancer. Biochemical Society
1372 Transactions *43*, 763–772. https://doi.org/10.1042/BST20150126.

1373 132. Gkogkas, C.G., Khoutorsky, A., Ran, I., Rampakakis, E., Nevarko, T., Weatherill, D.B., Vasuta, C.,
1374 Yee, S., Truitt, M., Dallaire, P., et al. (2013). Autism-related deficits via dysregulated eIF4E-
1375 dependent translational control. Nature *493*, 371–377. https://doi.org/10.1038/nature11628.

1376 133. Syntichaki, P., Troulinaki, K., and Tavernarakis, N. (2007). eIF4E function in somatic cells
1377 modulates ageing in Caenorhabditis elegans. Nature *445*, 922–926.
1378 https://doi.org/10.1038/nature05603.

1379 134. Costa-Mattioli, M., and Walter, P. (2020). The integrated stress response: From mechanism to
1380 disease. Science *368*, eaat5314. https://doi.org/10.1126/science.aat5314.

1381 135. Gadella, T.W.J., van Weeren, L., Stouthamer, J., Hink, M.A., Wolters, A.H.G., Giepmans, B.N.G.,
1382 Aumonier, S., Dupuy, J., and Royant, A. (2023). mScarlet3: a brilliant and fast-maturing red
1383 fluorescent protein. Nat Methods *20*, 541–545. https://doi.org/10.1038/s41592-023-01809-y.

1384 136. Costantini, L.M., Baloban, M., Markwardt, M.L., Rizzo, M.A., Guo, F., Verkhusha, V.V., and Snapp,
1385 E.L. (2015). A palette of fluorescent proteins optimized for diverse cellular environments. Nat
1386 Commun *6*, 7670. https://doi.org/10.1038/ncomms8670.

1387 137. Chakrabarti, S., Hore, Z., Pattison, L.A., Lalnunhlimi, S., Bhebhe, C.N., Callejo, G., Bulmer, D.C.,
1388 Taams, L.S., Denk, F., and Smith, E.S.J. (2020). Sensitization of knee-innervating sensory neurons by

tumor necrosis factor-α-activated fibroblast-like synoviocytes: an in vitro, coculture model of inflammatory pain. Pain *161*, 2129–2141. https://doi.org/10.1097/j.pain.0000000000001890.

138. Li, C.H., and Lee, C.K. (1993). Minimum cross entropy thresholding. Pattern Recognition *26*, 617–625. https://doi.org/10.1016/0031-3203(93)90115-D.

SUPPLEMENTAL INFORMATION

Document S1. Figures S1–S5

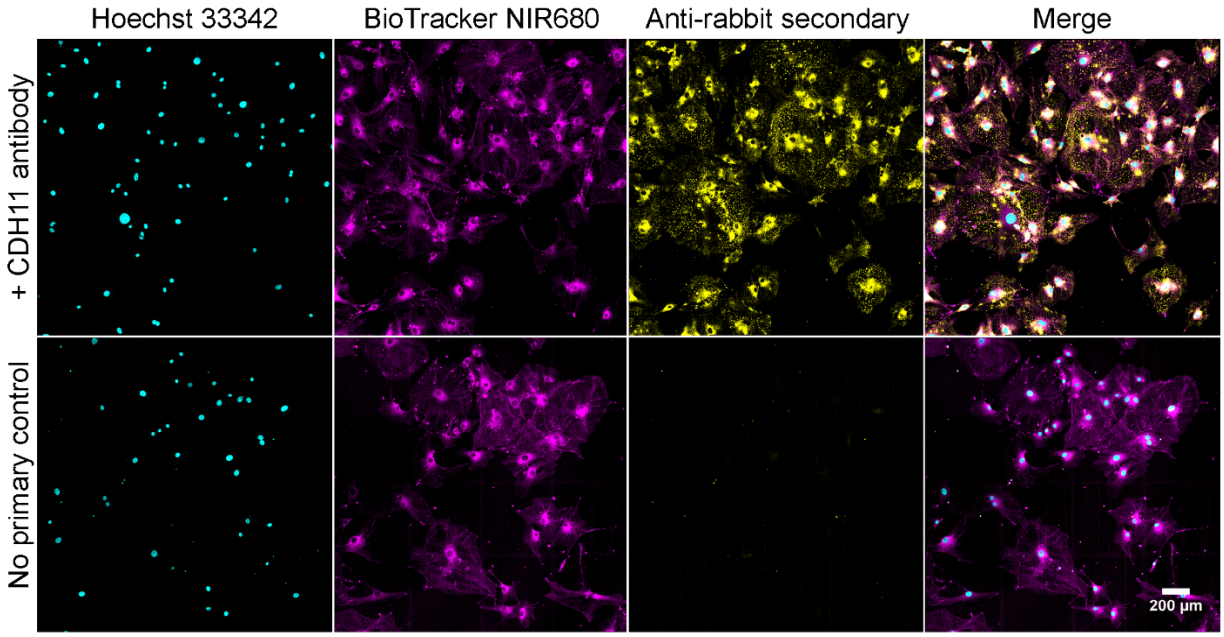

Fig. S1. Cadherin-11, a marker of fibroblast-like synoviocytes (FLS), stains cells isolated from mouse knee explants

Representative microscopy images of FLS isolated from mouse knee explants, stained with cadherin-11 (CDH11), an FLS marker. From left to right, columns show nuclear staining (Hoechst 33342, cyan), lipophilic membrane dye labeling (Biotracker NIR680, magenta), and Alexa 488 anti-rabbit secondary immunostaining (yellow), followed by a merged image. The top row shows cells treated with rabbit anti-CDH11 primary antibody, confirming CDH11 expression in isolated cells. The bottom row presents a no primary antibody control, showing no signal in the 488 channel. Scale bar = 200 µm.

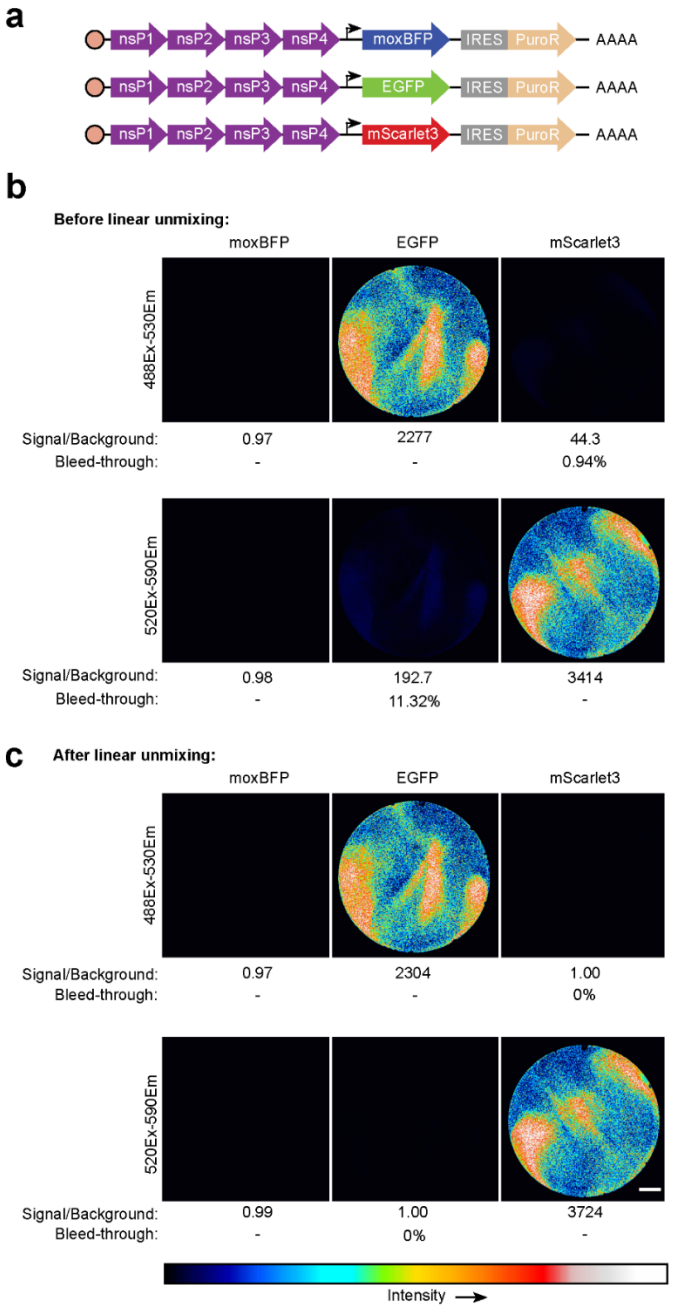

Fig. S2. Linear unmixing corrects spectral overlap of EGFP and mScarlet3 fluorescent signals imaged using the Odyssey M laser scanner

Schematic of the saRNA constructs used for linear unmixing, each expressing a different fluorescent protein: moxBFP, EGFP, and mScarlet3. These constructs were transfected into tSA201 cells. **b,** Representative imaging results showing fluorescence in the 488 and 520 channels, 1 day after transfection. moxBFP-transfected cells were not detected in either channel. EGFP was primarily detected in the 488 channel, with 11.32% bleedthrough into the 520 channel. mScarlet3 was primary detected in the 520 channel, with 0.94% bleedthrough into the 488 channel. Background signal was determined from mock transfected cells. **c,** Corrected images using linear unmixing to negate spectral bleedthrough from mScarlet3 and EGFP signals. Scale bars = 5 mm.

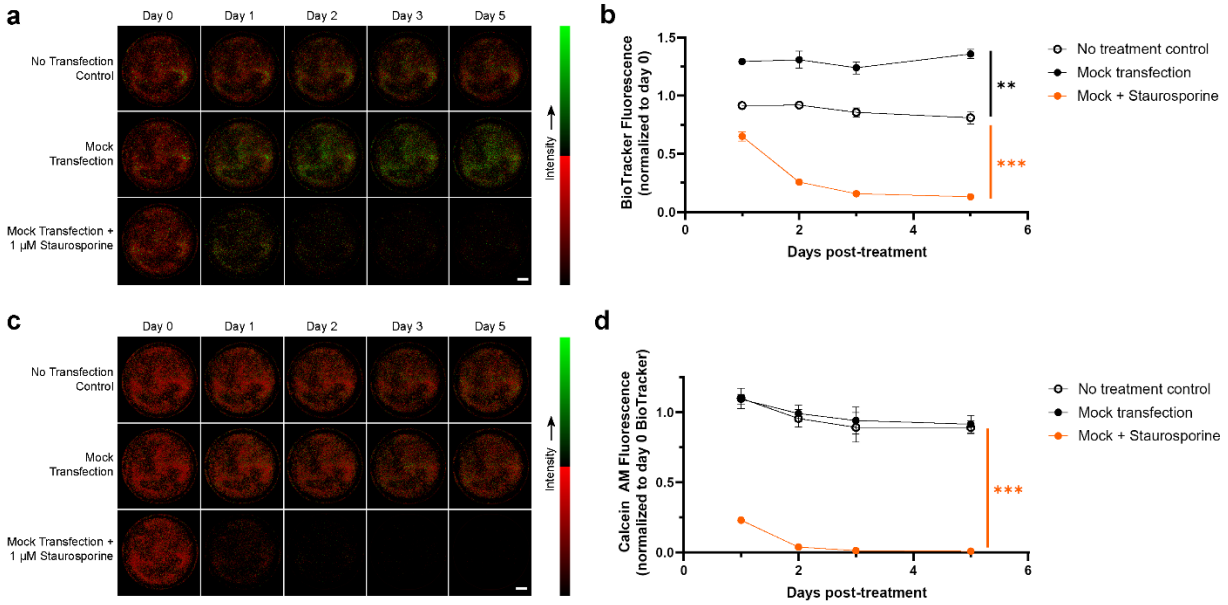

Fig. S3. BioTracker fluorescence indicates cell number following staurosporine-induced apoptosis, despite an increase after mock transfection

Validation of BioTracker fluorescence as a marker for cell number in the presence of apoptotic stimuli. **a,** Representative images of FLS stained with BioTracker under three conditions: no transfection control, mock transfection, and mock transfection with 1 μM staurosporine. BioTracker fluorescence intensity increases after mock transfection but decreases following staurosporine treatment, indicating cell loss. Scale bar = 5 mm. **b,** Quantification of BioTracker fluorescence over time for the three conditions (n = 3). Statistical significance was determined by two-way RM ANOVA with Dunnett's multiple comparisons test comparing groups to the no treatment control. **c,** Representative images of the same FLS stained with Calcein AM. Unlike BioTracker, Calcein AM fluorescence does not increase after mock transfection but decreases after staurosporine treatment, reflecting apoptotic cell death. Scale bar = 5 mm. **d,** Quantification of BioTracker fluorescence over time for the three conditions (n = 3). Fluorescence decreases following staurosporine treatment, consistent with findings in (a, b). Statistical significance was determined by two-way RM ANOVA with Dunnett's multiple comparisons test comparing groups to the no treatment control.

For all statistical reporting, $^{**}P < 0.01$ and $^{***}P < 0.001$. Data are presented as mean ± SEM.

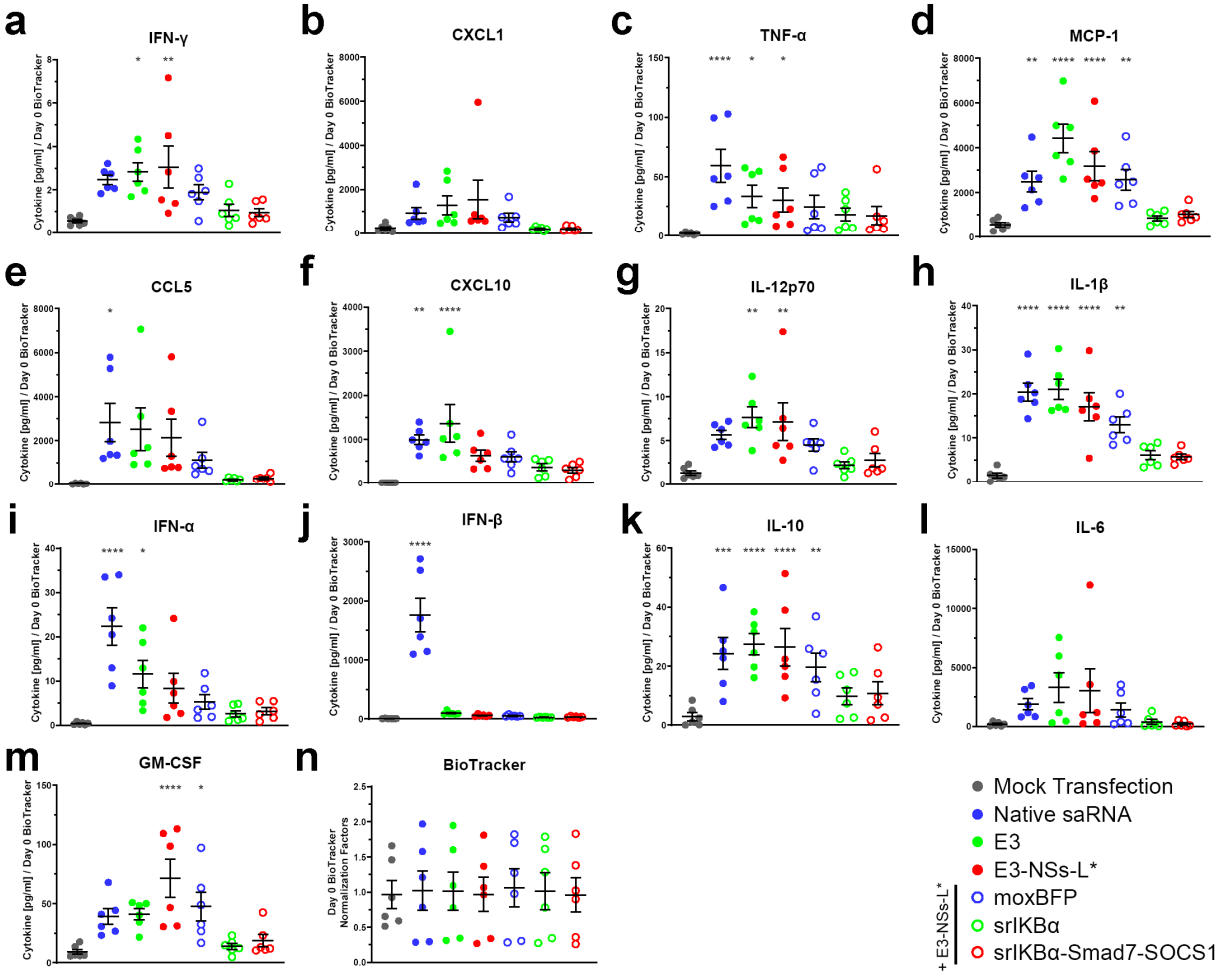

Fig. S4. Inhibition of dsRNA-sensing pathways and inflammatory signaling reduces saRNA-induced anti-viral cytokine secretion

Cytokines were collected from FLS 2 days post-transfection, quantified by bead-based immunoassay, and normalized by cell number using the BioTracker signal on day 0 (n = 6). Statistical significance for each cytokine was assessed using one-way RM ANOVA followed by Bonferroni's multiple comparisons test against the mock transfection control. A Bonferroni correction was applied to P values to account for multiple independent hypothesis testing. *P < 0.05, **P < 0.01, ***P < 0.001 and ****P < 0.0001. Data are presented as mean ± SEM.

a-m, Native saRNA induces anti-viral cytokine secretion. E3 reduces TNF-α (c), IFN-α (i), and IFN-β (j), secretion. E3-NSs-L* reduces CXCL10 secretion (f). srIκBα appears to reduce secretion of all cytokines tested. srIκBα-Smad7-SOCS1 does not reduce cytokine secretion more than srIκBα.

n, The BioTracker signal from day 0, used for normalizing differences in starting cell number, is shown.

Acronyms: IFN-γ, interferon-γ; CXCL1, C-X-C motif chemokine ligand 1; TNF-α, tumor necrosis factor-α; MCP-1, monocyte chemoattractant protein-1; IL-12p70, interleukin-12; CCL5, chemokine ligand 5; IL-1β, interleukin-1β; CXCL10, C-X-C motif chemokine ligand 10; GM-CSF, granulocyte-macrophage colony-stimulating factor; IL-10, interleukin-10; IFN-β, interferon-β; IFN-α, interferon-α; IL-6, interleukin-6.

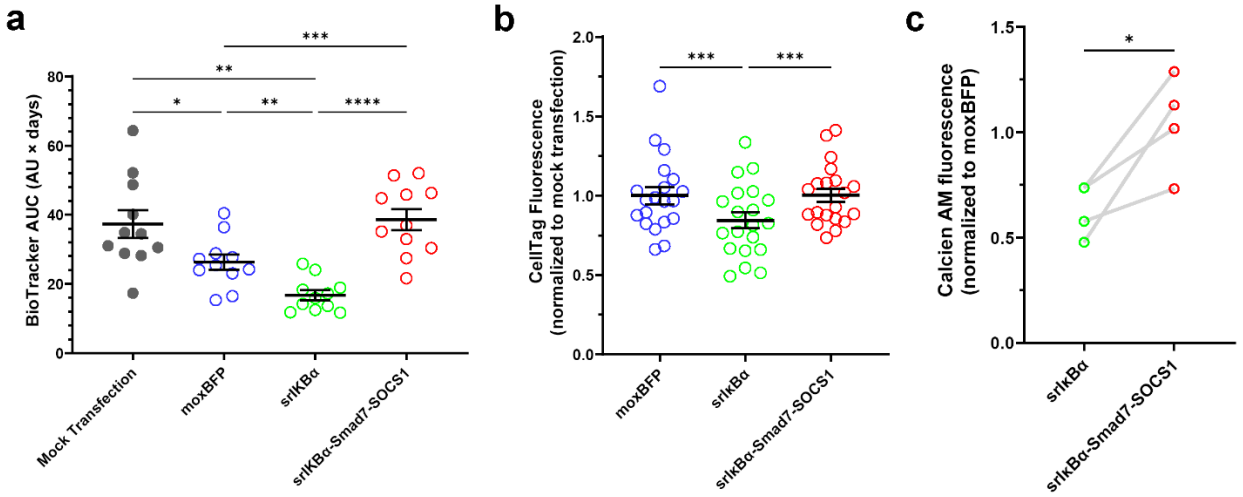

Fig. S5. srIκBα reduces cell number and viability, while srIκBα-Smad7-SOCS1 preserves both
a, AUC analysis of BioTracker fluorescence data shown in Fig. 5c, summarizing cumulative effects over the time course (n = 11). srIκBα induces reductions in integrated BioTracker signal, which is prevented by srIκBα-Smad7-SOCS1. Statistical analysis was performed using one-way RM ANOVA with Greenhouse–Geisser correction and Tukey's multiple comparisons test to compare all groups. Mock transfection data is also presented in Fig. 1g.
b, Quantification of mock transfection normalized CellTag signal (n = 20). The srIκBα construct reduces cell number, whereas this reduction is prevented by the srIκBα-Smad7-SOCS1 construct. Data were normalized to mock transfection. Statistical significance was determined by one-way RM ANOVA with Greenhouse–Geisser correction, and Tukey's multiple comparisons test. Data in this panel were pooled from in-cell western assays performed on day 2 post-transfection, incorporating data presented in Figs. 3 and 6 as well as additional data not shown elsewhere. ***$P < 0.001$.
c, Calcein AM staining performed 3 days post-transfection (n = 4). The srIκBα-Smad7-SOCS1 construct protects against reductions in cell viability induced by srIκBα. Data were normalized to the moxBFP construct. Statistical significance was determined by a paired t test. *$P<0.05$.
Data are presented as mean ± SEM. saRNA constructs used are shown in Fig. 4a.

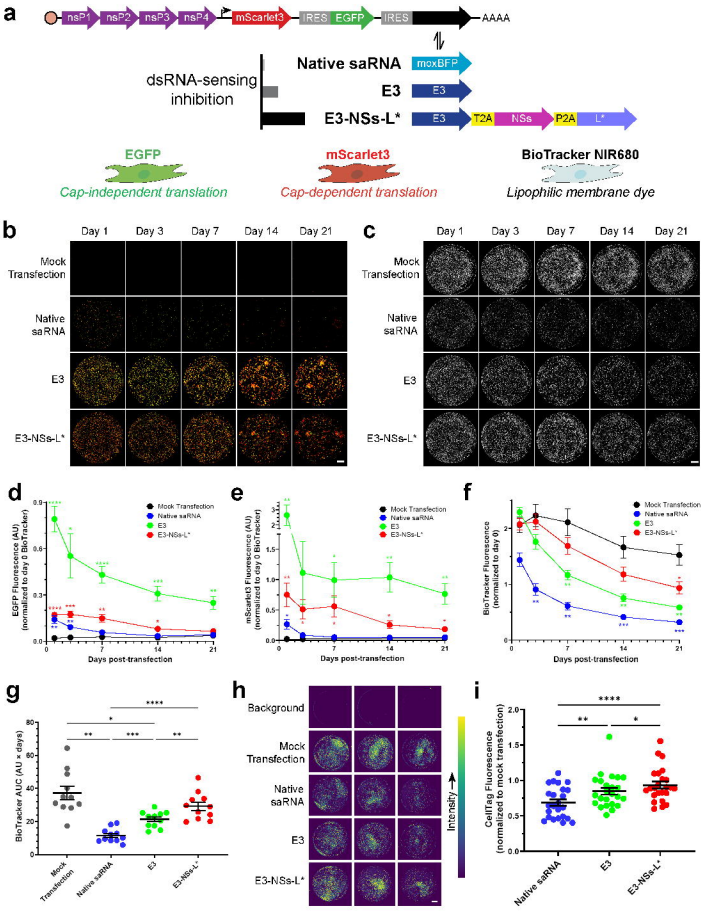
a
nsP1
nsP2
nsP3
nsP4
mScarlet3
IRES
EGFP
IRES
AAAA
dsRNA-sensing inhibition
Native saRNA
mcxBFP
E3
E3
E3-NSs-L*
E3
T2A
NSs
P2A
L*
EGFP
Cap-independent translation
mScarlet3
Cap-dependent translation
BioTracker NIR680
Lipophilic membrane dye
b
Day 1
Day 3
Day 7
Day 14
Day 21
Mock Transfection
Native saRNA
E3
E3-NSs-L*
c
Day 1
Day 3
Day 7
Day 14
Day 21
Mock Transfection
Native saRNA
E3
E3-NSs-L*
d
Mock Transfection
Native saRNA
E3
E3-NSs-L*
EGFP Fluorescence (AU)
(normalized to day 0 BioTracker)
Days post-transfection
e
Mock Transfection
Native saRNA
E3
E3-NSs-L*
mScarlet3 Fluorescence (AU)
(normalized to day 0 BioTracker)
Days post-transfection
f
Mock Transfection
Native saRNA
E3
E3-NSs-L*
BioTracker Fluorescence
(normalized to day 0)
Days post-transfection
g
BioTracker AUC (AU × days)
Mock Transfection
Native saRNA
E3
E3-NSs-L*
h
Background
Mock Transfection
Native saRNA
E3
E3-NSs-L*
Intensity
i
CellTag Fluorescence
(normalized to mock transfection)
Native saRNA
E3
E3-NSs-L*

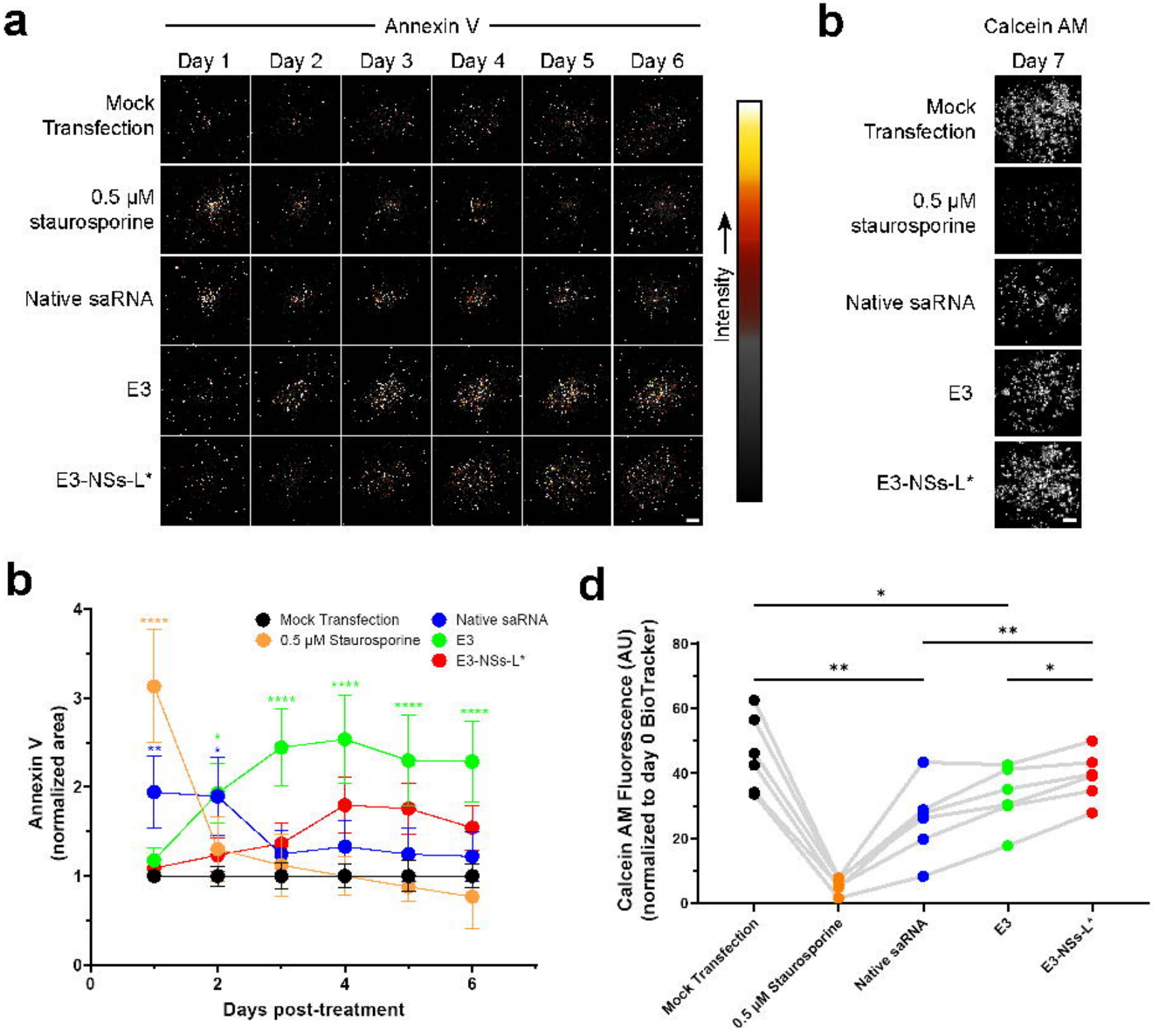
a
Annexin V
Day 1
Day 2
Day 3
Day 4
Day 5
Day 6
Mock Transfection
0.5 μM staurosporine
Native saRNA
E3
E3-NSs-L*
Intensity
b
Calcein AM
Day 7
Mock Transfection
0.5 μM staurosporine
Native saRNA
E3
E3-NSs-L*
b
Mock Transfection
0.5 μM Staurosporine
Native saRNA
E3
E3-NSs-L*
Annexin V (normalized area)
Days post-treatment
d
Calcein AM Fluorescence (AU) (normalized to day 0 BioTracker)
Mock Transfection
0.5 μM Staurosporine
Native saRNA
E3
E3-NSs-L*

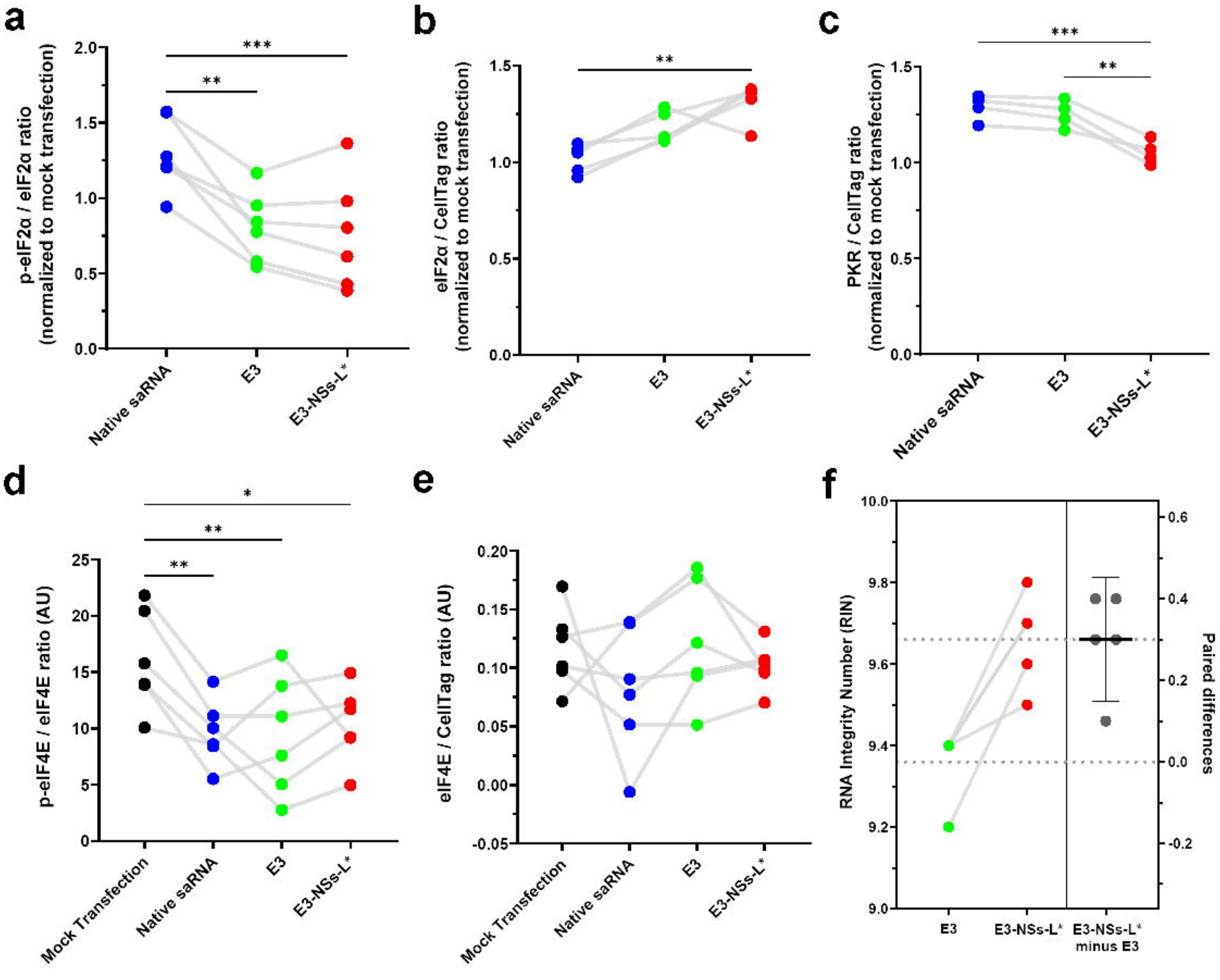
a
p-eIF2α / eIF2α ratio
(normalized to mock transfection)
2.0
1.5
1.0
0.5
0.0
***
**
Native saRNA
E3
E3-NSs-L*
b
eIF2α / CellTag ratio
(normalized to mock transfection)
1.5
1.0
0.5
0.0
**
Native saRNA
E3
E3-NSs-L*
c
PKR / CellTag ratio
(normalized to mock transfection)
1.5
1.0
0.5
0.0
***
**
Native saRNA
E3
E3-NSs-L*
d
p-eIF4E / eIF4E ratio (AU)
25
20
15
10
5
0
*
**
**
Mock Transfection
Native saRNA
E3
E3-NSs-L*
e
eIF4E / CellTag ratio (AU)
0.20
0.15
0.10
0.05
0.00
-0.05
Mock Transfection
Native saRNA
E3
E3-NSs-L*
f
RNA Integrity Number (RIN)
10.0
9.8
9.6
9.4
9.2
9.0
Paired differences
0.6
0.4
0.2
0.0
-0.2
E3
E3-NSs-L*
E3-NSs-L*
minus E3

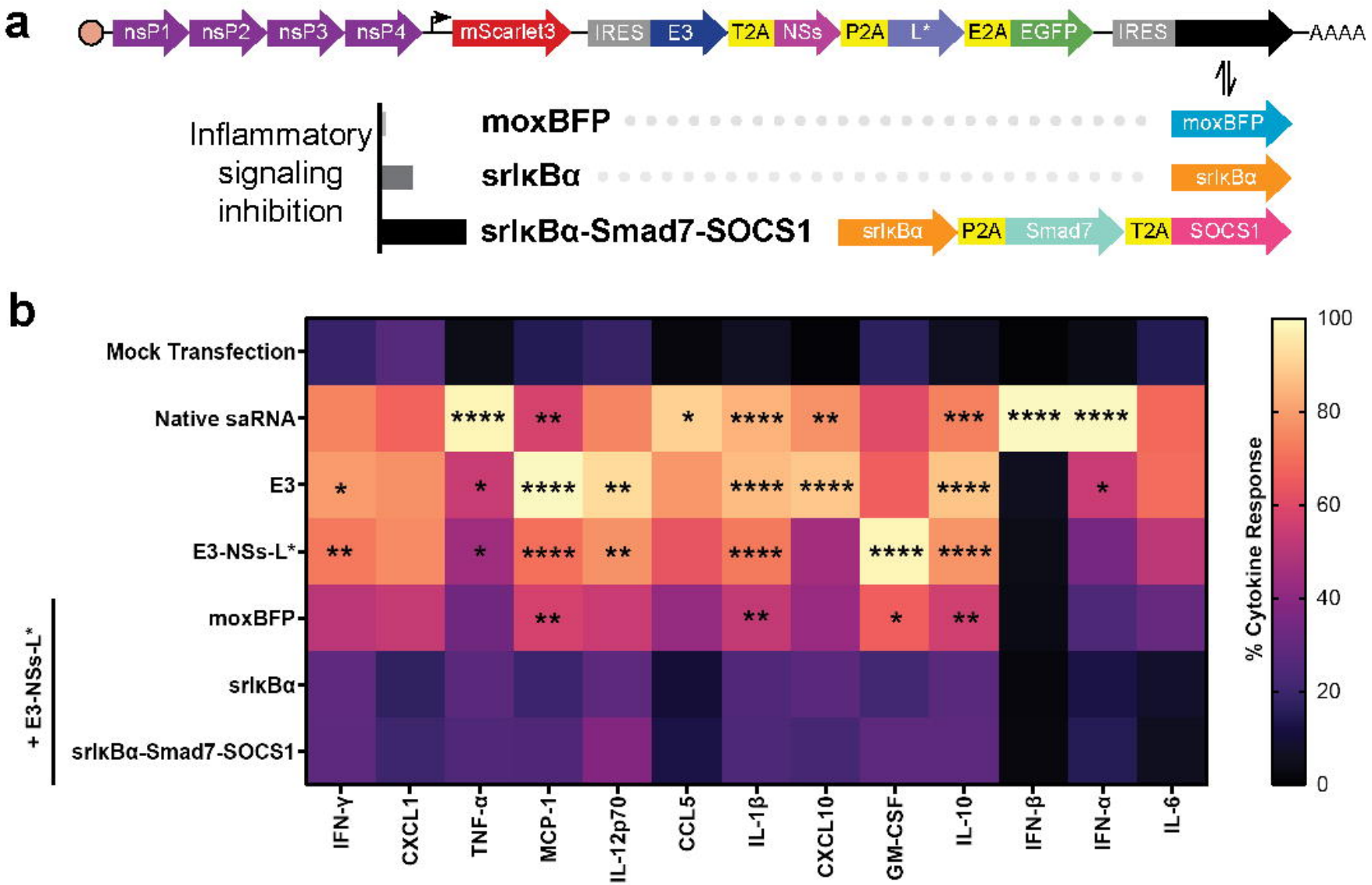
a
nsP1
nsP2
nsP3
nsP4
mScarlet3
IRES
E3
T2A
NSs
P2A
L*
E2A
EGFP
IRES
AAAA
Inflammatory signaling inhibition
moxBFP
srIκBα
srIκBα-Smad7-SOCS1
moxBFP
srIκBα
srIκBα
P2A
Smad7
T2A
SOCS1
b
Mock Transfection
Native saRNA
E3
E3-NSs-L*
moxBFP
srIκBα
srIκBα-Smad7-SOCS1
+ E3-NSs-L*
IFN-γ
CXCL1
TNF-α
MCP-1
IL-12p70
CCL5
IL-1β
CXCL10
GM-CSF
IL-10
IFN-β
IFN-α
IL-6
% Cytokine Response
100
80
60
40
20
0

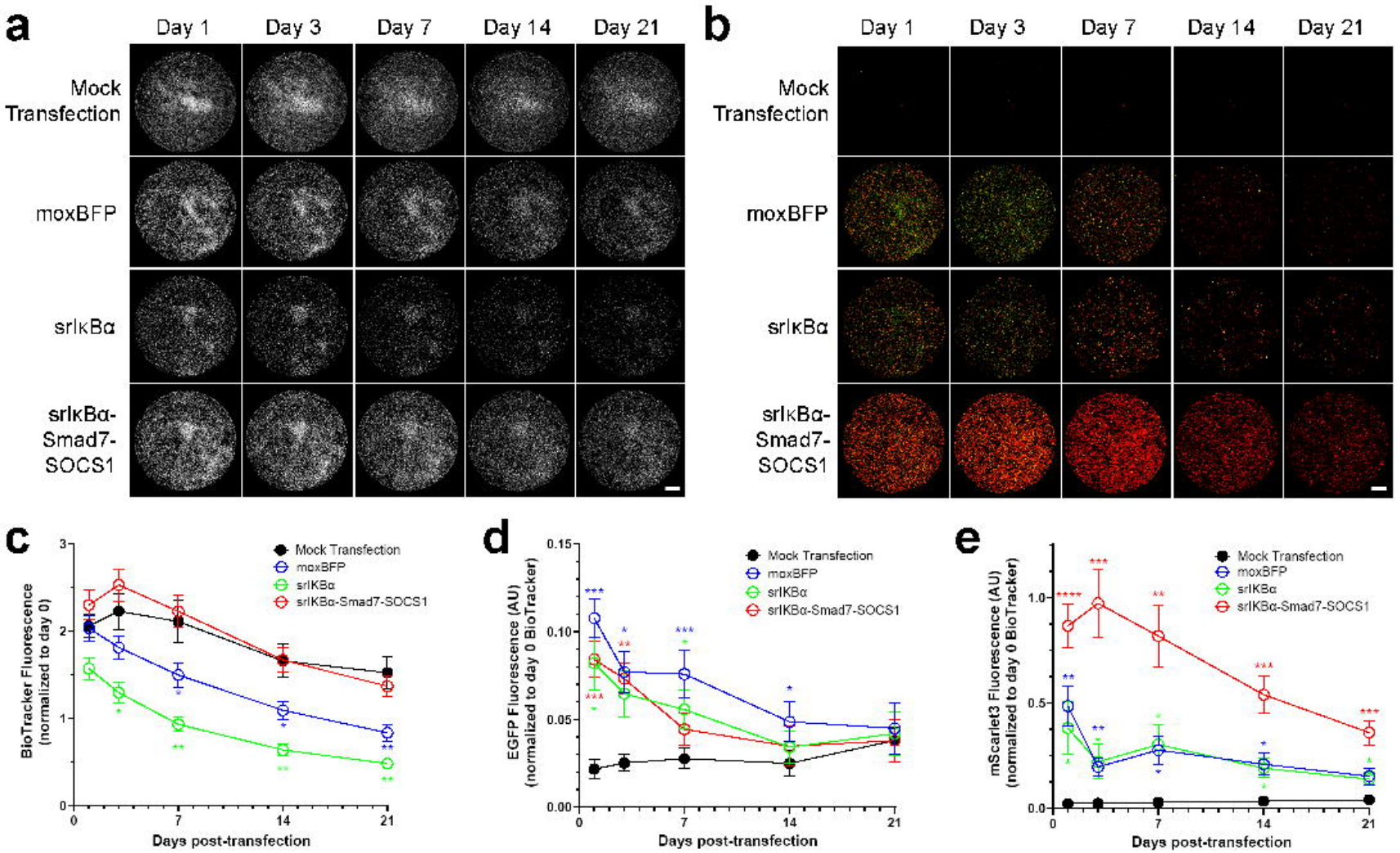
a
Day 1
Day 3
Day 7
Day 14
Day 21
Mock Transfection
moxBFP
srIκBα
srIκBα-Smad7-SOCS1
b
Day 1
Day 3
Day 7
Day 14
Day 21
Mock Transfection
moxBFP
srIκBα
srIκBα-Smad7-SOCS1
c
BioTracker Fluorescence (normalized to day 0)
Days post-transfection
Mock Transfection
moxBFP
srIKBα
srIKBα-Smad7-SOCS1
d
EGFP Fluorescence (AU) (normalized to day 0 BioTracker)
Days post-transfection
Mock Transfection
moxBFP
srIKBα
srIKBα-Smad7-SOCS1
e
mScarlet3 Fluorescence (AU) (normalized to day 0 BioTracker)
Days post-transfection
Mock Transfection
moxBFP
srIKBα
srIKBα-Smad7-SOCS1

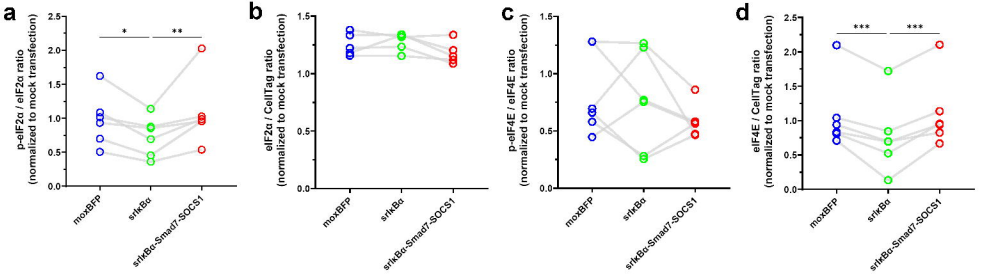
a
p-eIF2α / eIF2α ratio
(normalized to mock transfection)
2.5
2.0
1.5
1.0
0.5
0.0
*
**
moxBFP
srkBα
srkBα-Smad7-SOCS1
b
eIF2α / CellTag ratio
(normalized to mock transfection)
1.5
1.0
0.5
0.0
moxBFP
srkBα
srkBα-Smad7-SOCS1
c
p-eIF4E / eIF4E ratio
(normalized to mock transfection)
1.0
0.5
0.0
moxBFP
srkBα
srkBα-Smad7-SOCS1
d
eIF4E / CellTag ratio
(normalized to mock transfection)
2.5
2.0
1.5
1.0
0.5
0.0
***
***
moxBFP
srkBα
srkBα-Smad7-SOCS1

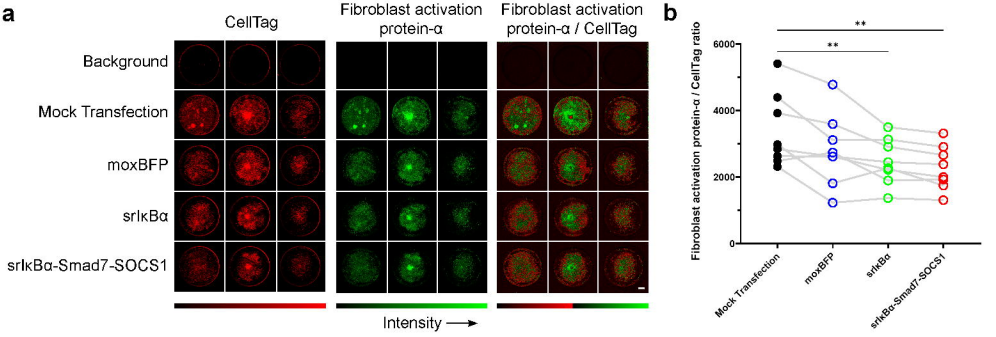
a
CellTag
Fibroblast activation protein-α
Fibroblast activation protein-α / CellTag
Background
Mock Transfection
moxBFP
srIκBα
srIκBα-Smad7-SOCS1
Intensity
b
Fibroblast activation protein-α / CellTag ratio
6000
4000
2000
0
**
**
Mock Transfection
moxBFP
srIκBα
srIκBα-Smad7-SOCS1

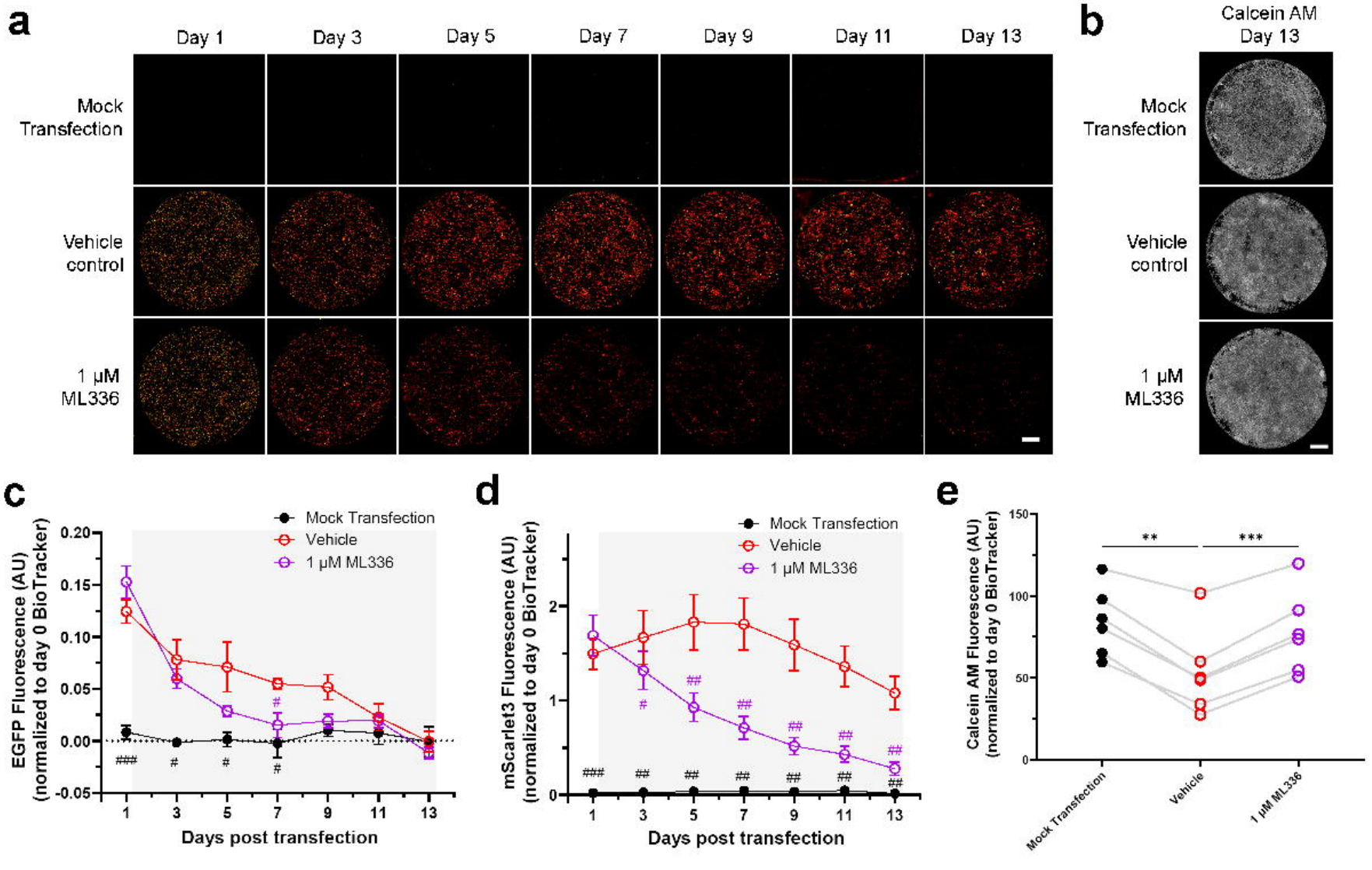
a
Day 1
Day 3
Day 5
Day 7
Day 9
Day 11
Day 13
Mock Transfection
Vehicle control
1 μM ML336
b
Calcein AM Day 13
Mock Transfection
Vehicle control
1 μM ML336
c
Mock Transfection
Vehicle
1 μM ML336
EGFP Fluorescence (AU) (normalized to day 0 BioTracker)
Days post transfection
d
Mock Transfection
Vehicle
1 μM ML336
mScarlet3 Fluorescence (AU) (normalized to day 0 BioTracker)
Days post transfection
e
Calcein AM Fluorescence (AU) (normalized to day 0 BioTracker)
Mock Transfection
Vehicle
1 μM ML336

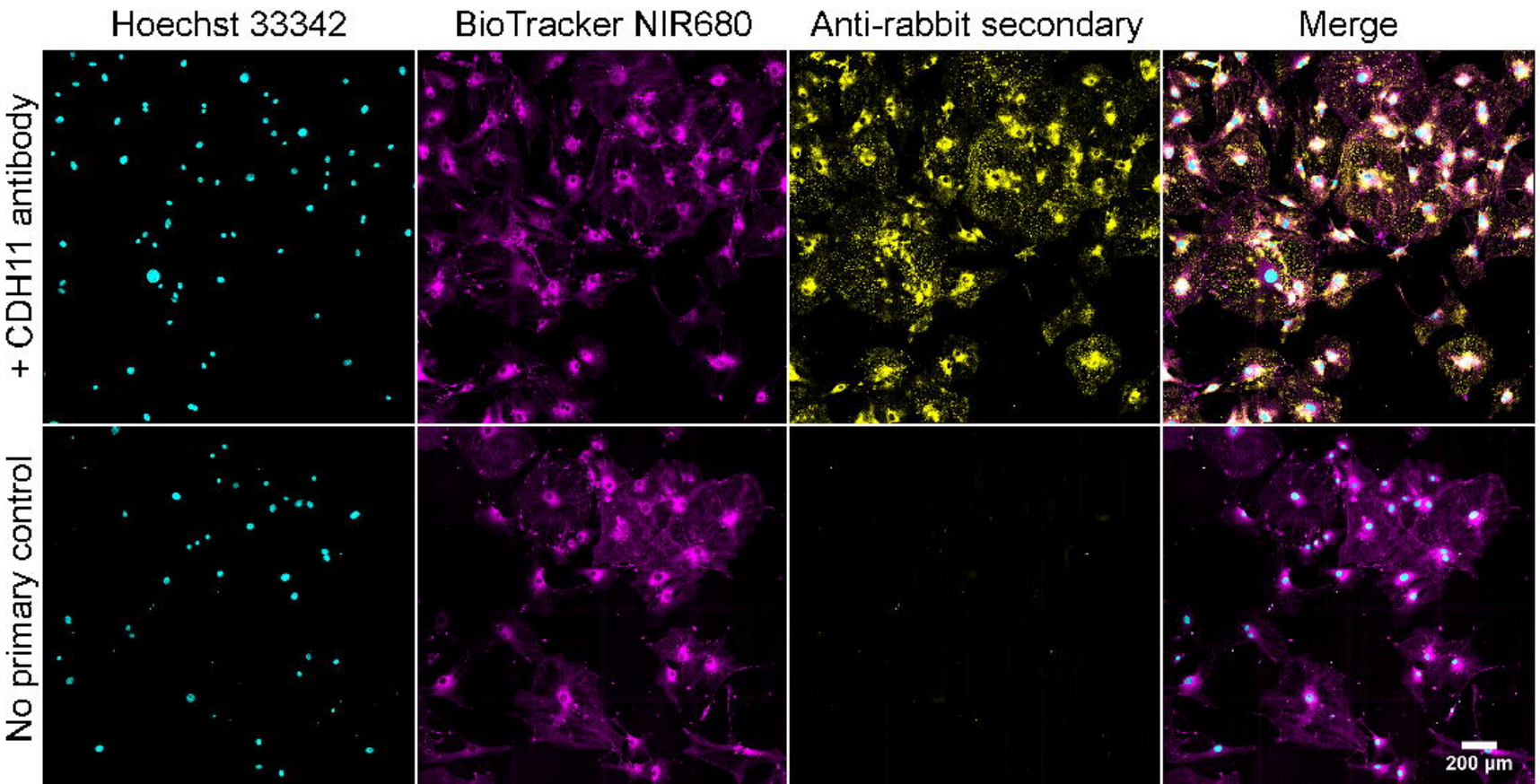
Hoechst 33342
BioTracker NIR680
Anti-rabbit secondary
Merge
+ CDH11 antibody
No primary control
200 µm

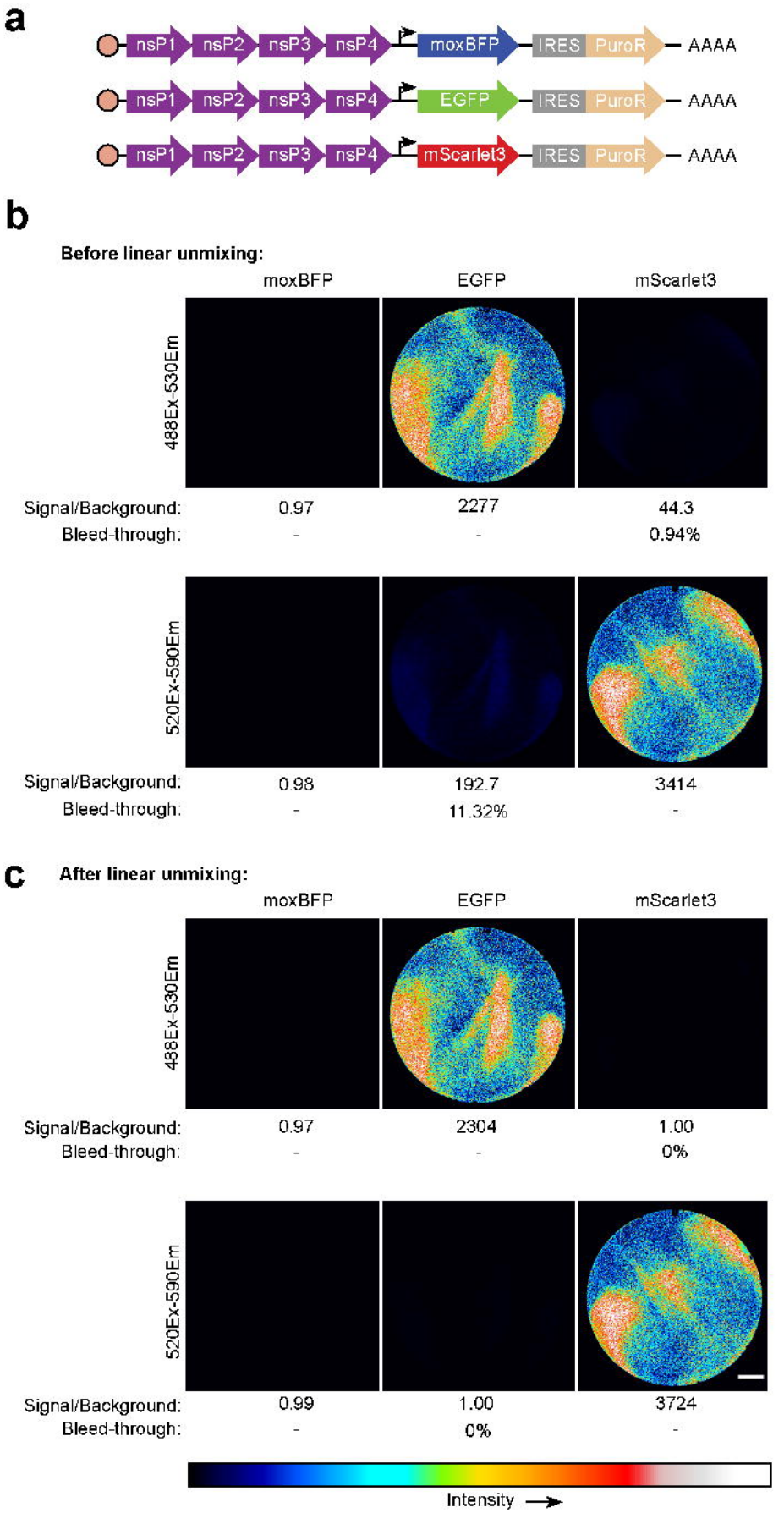
a
nsP1
nsP2
nsP3
nsP4
moxBFP
EGFP
mScarlet3
IRES
PuroR
AAAA
b
Before linear unmixing:
moxBFP
EGFP
mScarlet3
488Ex-530Em
Signal/Background:
0.97
2277
44.3
Bleed-through:
-
-
0.94%
520Ex-590Em
Signal/Background:
0.98
192.7
3414
Bleed-through:
-
11.32%
-
c
After linear unmixing:
moxBFP
EGFP
mScarlet3
488Ex-530Em
Signal/Background:
0.97
2304
1.00
Bleed-through:
-
-
0%
520Ex-590Em
Signal/Background:
0.99
1.00
3724
Bleed-through:
-
0%
-
Intensity

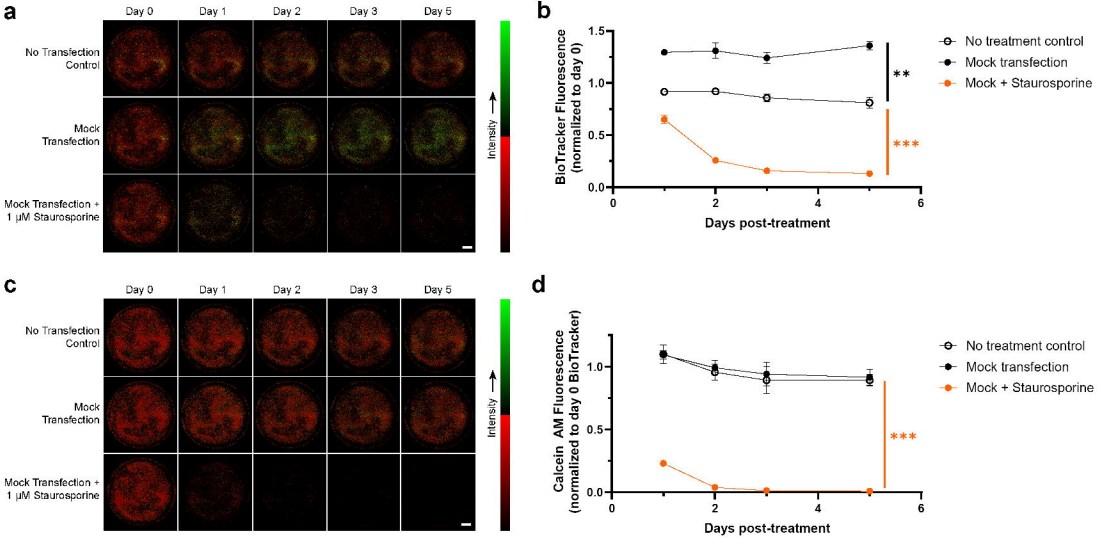
a
Day 0
Day 1
Day 2
Day 3
Day 5
No Transfection Control
Mock Transfection
Mock Transfection + 1 µM Staurosporine
Intensity
b
BioTracker Fluorescence (normalized to day 0)
1.5
1.0
0.5
0.0
0
2
4
6
Days post-treatment
**
***
No treatment control
Mock transfection
Mock + Staurosporine
c
Day 0
Day 1
Day 2
Day 3
Day 5
No Transfection Control
Mock Transfection
Mock Transfection + 1 µM Staurosporine
Intensity
d
Calcein AM Fluorescence (normalized to day 0 BioTracker)
1.0
0.5
0.0
0
2
4
6
Days post-treatment
***
No treatment control
Mock transfection
Mock + Staurosporine

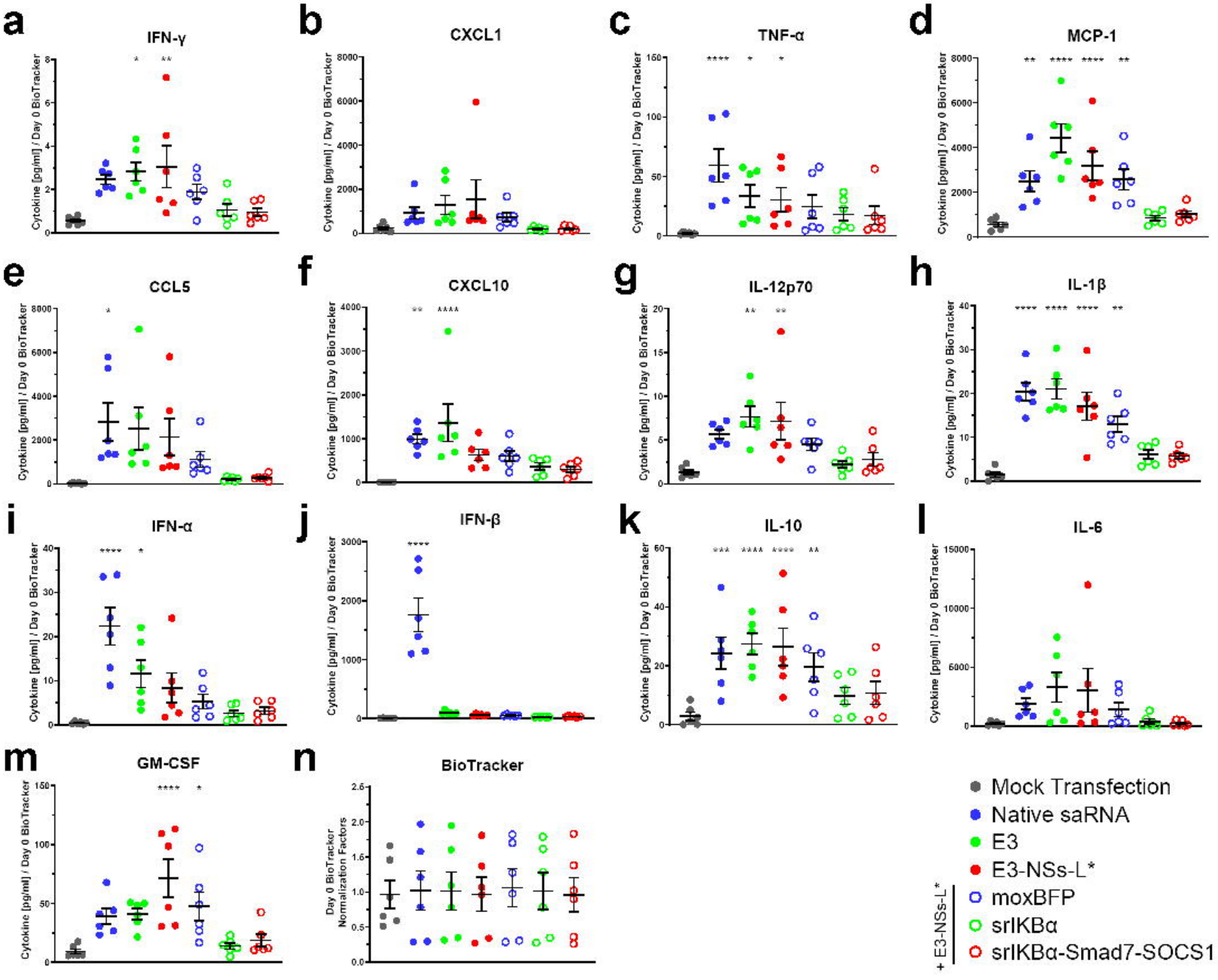
a
IFN-γ
b
CXCL1
c
TNF-α
d
MCP-1
e
CCL5
f
CXCL10
g
IL-12p70
h
IL-1β
i
IFN-α
j
IFN-β
k
IL-10
l
IL-6
m
GM-CSF
n
BioTracker
Cytokine [pg/ml] / Day 0 BioTracker
Day 0 BioTracker Normalization Factors
Mock Transfection
Native saRNA
E3
E3-NSs-L*
moxBFP
srIKBα
srIKBα-Smad7-SOCS1
+ E3-NSs-L*

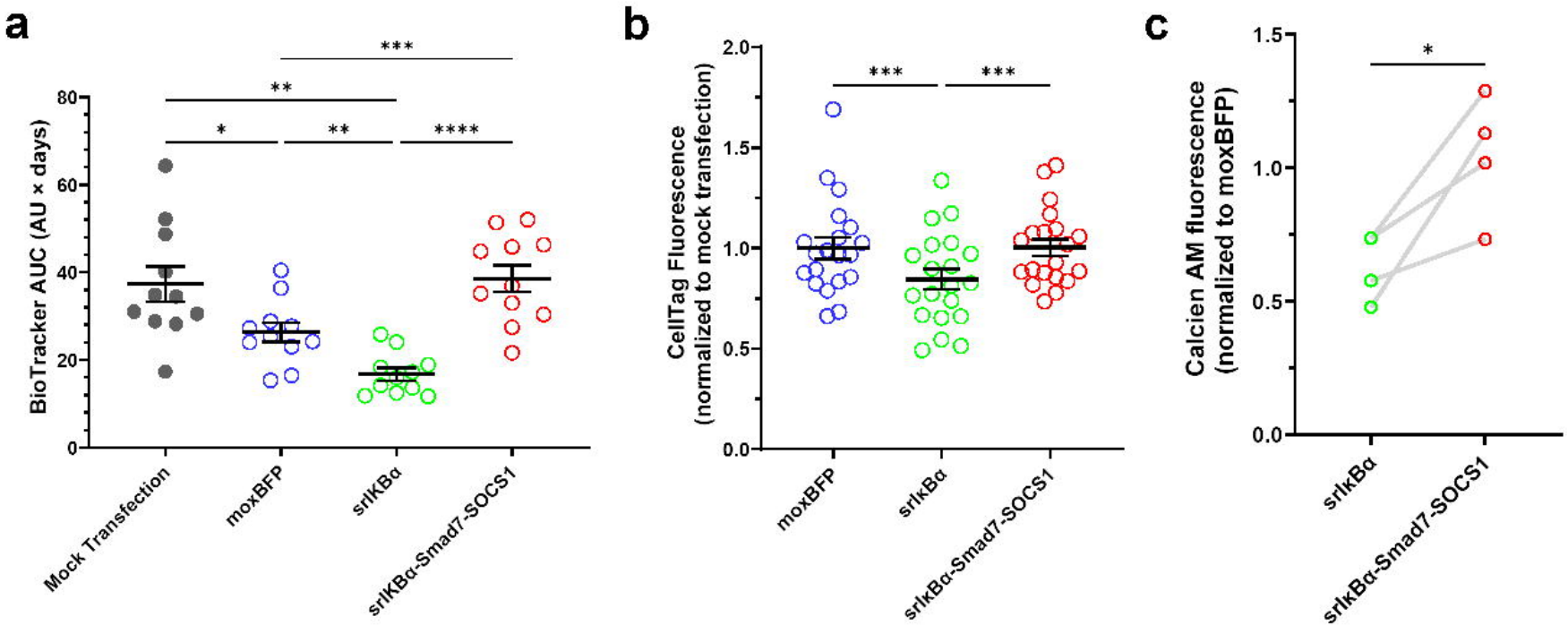
a
BioTracker AUC (AU × days)
0
20
40
60
80
***
**
*
**
****
Mock Transfection
moxBFP
srIKBα
srIKBα-Smad7-SOCS1
b
CellTag Fluorescence
(normalized to mock transfection)
0.0
0.5
1.0
1.5
2.0
***
***
moxBFP
srIκBα
srIκBα-Smad7-SOCS1
c
Calcien AM fluorescence
(normalized to moxBFP)
0.0
0.5
1.0
1.5
*
srIκBα
srIκBα-Smad7-SOCS1